

**POLITECNICO DI TORINO**

Collegio di Ingegneria Chimica e dei Materiali

**Master of Science Course  
in Materials Engineering**

Master of Science Thesis

**Performance of Enamel Coating:  
Corrosion Prevention in Reinforced  
Concrete and Metal Pipeline under  
Environmental and Vibrating Effects**



**Tutors**

Prof. Gian Paolo Cimellaro

Prof. Genda Chen

Prof. Richard K. Brow

**Candidate**

Erica Nesti

December 2019



# Table of Contents

<i>Sommario Italiano</i>	<b>i</b>
<i>Introduction</i>	<b>xiii</b>
<b>1 Background</b>	<b>1</b>
<b>1.1 Oil and Gas Pipeline</b>	<b>1</b>
1.1.1 Pipeline Classification	2
1.1.2 United State Pipeline Condition	6
1.1.3 Flammability limit	7
<b>1.2 Bridges</b>	<b>9</b>
1.2.1 Reinforced Concrete	10
1.2.2 Advantages of Reinforced Concrete	10
1.2.3 Disadvantages of Reinforced Concrete as a Structural Material	11
1.2.4 Properties of Reinforced Concrete	11
1.2.5 Manufacturing Techniques	13
1.2.6 United States Bridges Condition	14
<b>1.3 Corrosion</b>	<b>17</b>
<b>1.4 Pipeline Corrosion</b>	<b>18</b>
1.4.1 Pipeline Protection	19
<b>1.5 Corrosion in Reinforced Concrete Bridges</b>	<b>23</b>
1.5.1 Degradation Mechanism of Reinforced Concrete	23
1.5.2 Starting and Propagation of Corrosion in Reinforced Concrete	24
1.5.3 Protection of Reinforced Concrete	27
<b>2 Materials</b>	<b>29</b>
<b>3 Methods</b>	<b>31</b>
<b>3.1 Metal Pipe under Environmental and Vibrating Effects</b>	<b>31</b>
3.1.1 Soil-Pipe Interaction Model	31
3.1.2 Flow Induced Vibrations in the Pipe	32
3.1.3 MATLAB Analysis of Steel Vibrating Pipe	36
3.1.4 Fluid Dynamic Regime	38
3.1.5 Assessment of Pipe Fluid Flow Rate for Turbulence Regime	38
3.1.6 Flow Induced Vibration in Enamel Coated Pipe	41
3.1.7 MATLAB Analysis of Enamel Coated Pipe	42
<b>3.2 Corrosion Performance of Steel Rebar Enamel Coated</b>	<b>43</b>
3.2.1 Sample Preparation	44
3.2.2 Visual Observation	45
3.2.3 Electrochemical Test	45
3.2.4 Visual Observation	51
3.2.5 Microstructural Analysis	51
<b>4 Results</b>	<b>53</b>
<b>4.1 MATLAB Simulations for Steel Vibrating Pipe</b>	<b>53</b>
4.1.1 Pipe Diameter modify the Pipe Vibration	53
4.1.2 Ground Constant modify the Pipe Vibration	53
4.1.3 Fluid Rate modify the Pipe Vibration	53
4.1.4 Fluid Density modify the Pipe Vibrations	54

<b>4.2</b>	<b>MATLAB Simulations for Steel Vibrating Pipe Enamel Coated</b>	<b>59</b>
4.2.1	Pipe Diameter modify the Coated Pipe Vibrations	59
4.2.2	Coating Thickness modify the Coated Pipe Vibrations	59
4.2.3	Fluid Flow Rate modify the Enamel Coated Pipe Vibrations	59
4.2.4	Ground Constant modify the Enamel Coated Pipe Vibrations	59
<b>4.3</b>	<b>Performance of Enamel Coating</b>	<b>64</b>
4.3.1	Electrochemical Test	64
<b>4.4</b>	<b>Visual Observation</b>	<b>85</b>
4.4.1	Microstructural Analysis	86
<b>5</b>	<b><i>Discussion</i></b>	<b>89</b>
5.1	Influence of Coating in Vibrating Pipe	89
5.2	Enamel Coating	89
<b>6</b>	<b><i>Conclusion</i></b>	<b>91</b>
<b>7</b>	<b><i>Symbols List</i></b>	<b>93</b>
<b>8</b>	<b><i>References</i></b>	<b>95</b>
<b>9</b>	<b><i>Appendices</i></b>	<b>99</b>
9.1	MATLAB Code for Clamped Pipe carrying Fluid	99
9.2	MATLAB Code for Enamel Coated Pipe carrying Fluid	100
<b>10</b>	<b><i>Acknowledgements</i></b>	<b>103</b>

## Sommario Italiano

La corrosione è un processo spontaneo che affligge preferenzialmente i materiali metallici causandone la degradazione e la perdita delle performance desiderate. Questo fenomeno è facilmente promosso quando un componente metallico è a diretto contatto con l'ambiente naturale, in particolar modo, la presenza di acqua e di ossigeno sulla superficie, promuove la formazione di reazioni elettrochimiche che propagano il processo corrosivo. Come la termodinamica conferma, i materiali metallici reagiscono con l'ambiente per raggiungere il loro stato di minima energia, che è sotto forma di ossidi o carbonati. La corrosione è un fenomeno che colpisce principalmente il settore energetico, chimico, petrolchimico, meccanico e delle infrastrutture dei trasporti. Sebbene i danni, che la corrosione può causare, sono ben noti, frequentemente questa viene sottovalutata, fino a che non si verificano incidenti, che portano all'interruzione del ciclo produttivo oppure mettono a rischio la vita delle persone. Ad esempio, ciò è avvenuto nell'esplosione a San Bruno in California nel 2010 a causa del rilascio di gas da una condotta interrata o nel collasso del ponte Seongsu in Sud Corea nel 1994.

Il calcestruzzo armato è sicuramente uno dei materiali più utilizzati per la realizzazione di strutture, anche se in un primo momento era stato considerato un materiale intrinsecamente durevole con elevata resistenza agli agenti corrosivi, senza la necessità di particolari attenzioni, con il tempo si è compreso che questo materiale è sensibile a fenomeni di degradazione, quindi, deve essere opportunamente sottoposto ad operazioni di mantenimento e di controllo. Il cemento armato è soggetto a diverse forme di danneggiamento, fisiche, come i cicli gelo-disgelo, meccaniche, dovute a fenomeni di abrasione, erosione o esplosione, chimici, a causa dell'attacco di soluzioni acide, basiche o contenenti cloruri, oppure biologiche, dovute alla presenza di fouling. Molto spesso questi processi avvengono contemporaneamente quindi è difficile identificare una singola causa di fallimento. Il calcestruzzo armato presenta al suo interno una gabbia di tondini d'acciaio che hanno lo scopo di sostenere i carichi tensili che si generano nella struttura, così da supplire alla scarsa resistenza a trazione del calcestruzzo. La presenza di un materiale metallico all'interno del calcestruzzo genera un'addizionale sorgente di corrosione e possibile danneggiamento per il calcestruzzo armato. Si possono avere fenomeni di carbonatazione, che portano ad una progressiva diminuzione del pH nel calcestruzzo e alla progressiva scomparsa del layer di passività sulla superficie dei tondini. A causa della presenza di cloruri nell'ambiente esterno si può verificare la corrosione dell'armatura, oppure, si può avere il danneggiamento dello strato di passività a causa di correnti disperse generate dalla presenza di campi elettrici esterni. Una volta che il film di passività risulta danneggiato, il processo corrosivo prosegue fino a che l'integrità della struttura è compromessa.

Per ovviare o ritardare questi fenomeni negli anni sono state sviluppate diverse tecniche per proteggere le strutture in calcestruzzo armato. In particolar modo, si può agire modificando la superficie o la composizione chimica della formulazione del calcestruzzo stesso; si può proteggere i tondini d'acciaio con rivestimenti epossidici o zincati, o applicando protezione catodica oppure utilizzando un acciaio con una composizione chimica che abbia maggiore resistenza alla corrosione. In alcuni casi si può anche agire modificando l'ambiente esterno, per esempio controllando il tasso di umidità, la concentrazione di cloruri o di anidride carbonica, ma c'è da dire che questo tipo di strategia spesso trova difficile applicazione. Le infrastrutture in calcestruzzo armato non sono le uniche opere che risentono della corrosione, infatti, le condotte destinate al trasporto di fluidi, come acqua, gas naturale o greggio, sono un altro tipo di struttura che tende a deteriorarsi a causa di questo processo. Per quanto riguarda le condotte, la corrosione può essere indotta o da fattori interni, associati all'ambiente che si sviluppa all'

interno della tubatura oppure a fattori esterni, dovuti cioè all'ambiente esterno, ad esempio se la condotta è interrata o sommersa. Alcune delle principali cause che innescano il processo corrosivo possono essere, il tasso di umidità, il contatto con soluzioni contenenti cloruri, la reattività dei liquidi trasportati o la presenza di microrganismi. Per ridurre questi rischi, si possono utilizzare diverse strategie come la protezione catodica tramite correnti impresse che fornisce corrente alla struttura così da annullare la corrente di corrosione, oppure attraverso anodi sacrificali dove la struttura è collegata elettricamente con un materiale meno nobile rispetto alla tubatura stessa così da promuovere la corrosione di questo materiale e lasciare integra la struttura. Un'altra alternativa, è quella di utilizzare i rivestimenti, che possono essere depositati internamente o esternamente al condotto, a seconda se l'ambiente aggressivo sia associato all'ambiente interno o esterno. Attualmente, rivestire i condotti è sicuramente la pratica più utilizzata, perché la ricopertura fornisce vantaggi aggiuntivi: riduzione delle perdite di carico, diminuzione dei costi di trasporto e pompaggio o riduzione dei tempi di ispezione e controllo. Il materiale più utilizzato per realizzare questi rivestimenti è la resina epossidica, che fornisce un'ottima resistenza a corrosione ed è facilmente depositabile sulla superficie. Sfortunatamente, l'adesione superficiale con la tubatura è solo meccanica quindi con il tempo si osserva un distacco progressivo del rivestimento che promuove fenomeni di corrosione interstiziale. Inoltre, la presenza di particelle dure disperse nel fluido, come carbonati, silice, solfati o particelle di sporco, può verificare la graffiatura del rivestimento così da esporre il substrato all'ambiente aggressivo.

Per ridurre i rischi dovuti alla propagazione dei processi corrosivi, negli anni sono stati sviluppati vari sistemi di protezione delle strutture. È proprio all'interno di questo argomento, che si colloca questo lavoro di tesi, si sviluppa un modello dinamico per comprendere le performance di uno smalto ceramico di vetro borosilicato depositato all'interno di una condotta interrata per resistere alle vibrazioni indotte dal passaggio di liquidi o gas infiammabili. Inoltre, si valuta le prestazioni di resistenza a corrosione di questo stesso rivestimento, depositato sulle superfici di tondini d'acciaio utilizzati per la realizzazione di opere in calcestruzzo armato. In particolare, si studiano due diversi tipi di coating vetrosi ottenuti tramite due diversi processi tecnologici, uno partendo da slurry e uno partendo da polveri. I campioni di tondini sono stati testati in una soluzione 3.5% wt di NaCl e in una soluzione satura di  $\text{Ca}(\text{OH})_2$  con pH 14. La prima soluzione studia il processo degradativo di strutture in calcestruzzo armato in presenza di cloruri; ad esempio in condizioni reali questo si verifica nei ponti costruiti in ambienti marini. Al contrario, la seconda soluzione mostra il progredire dei processi corrosivi sui tondini all'interno del calcestruzzo stesso, dove si crea un ambiente con pH 14.

## **1. Materiali**

Sono stati testati due diversi tipi di rivestimenti vetrosi, con composizione simile, ma ottenuti con due diverse tecniche di deposizione. Il primo è il T-001 slurry, fornito da TOMATEC, il secondo è il GP2118 in polvere, fornito da PEMCO. In Tabella 2.2 sono riportate le composizioni chimiche esatte di questi materiali, per comprendere la natura chimica esatta di questi rivestimenti, in particolar modo, essi sono costituiti da un vetro borosilicato. Le principali proprietà di questo materiale sono l'ottima resistenza al calore e agli sbalzi termici, grazie al basso coefficiente di dilatazione termica, e l'elevata inerzia chimica. Il processo di produzione dei coating, in entrambi i casi, inizia con uno step di spazzolatura del substrato da rivestire, per rimuovere lo sporco e gli ossidi superficiali che si formano durante l'esposizione dei tondini d'acciaio con l'atmosfera. A seguire, il T-001 slurry coating è spruzzato sulla superficie da

rivestire, il componente è introdotto in forno e riscaldato a 150 °C per 10 min, così da promuovere l'evaporazione dell'acqua, dopodichè, si esegue una rampa termica fino a 815 °C mantenendo questa temperatura per 10 min, così da permettere la vetrificazione, in fine si estrae il componente dal forno e si raffredda in aria. Per quanto riguarda il processo produttivo del coating GP2118 in polvere, si ha una prima fase di spazzolatura del componente, seguito da uno step di spruzzatura elettrostatica per permettere l'adesione delle polveri sul substrato. A questo punto, il componente rivestito è sottoposto ad un ciclo termico a 843 °C per 10 minuti, così da promuovere la formazione del vetro e la realizzazione di un coating compatto, al termine il campione viene prelevato e raffreddato fino a temperatura ambiente in aria. I substrati presi in considerazione in questo lavoro di tesi sono dei tubi d'acciaio API 5L X65, realizzati da MRC Global, ottenuti per deformazione plastica a freddo e dei tondini d'acciaio con diametro 2.54 cm ottenuti tramite un processo di fusione e colata in stampo. Le specifiche composizioni di questi acciai sono presentate in Tabella 2.2 e 2.3.

Per chiarezza, il lavoro di tesi si presenta in due parti, nella prima, si presenta lo stato dell'arte e i metodi utilizzati per descrivere il modello dinamico del condotto rivestito internamente con il coating ceramico. Nella seconda parte, si ha un'introduzione generale sull'impiego nei calcestruzzi armati nei ponti, seguito dall'illustrazione dei metodi e dei risultati ottenuti riguardo le prestazioni dei tondini d'acciaio rivestiti.

## **2. Vibrazioni in Condotte Rivestite con Coating Ceramici di Vetro Borosilicato**

Le condotte, impiegate nel settore oil & gas, sono destinate al trasporto e alla distribuzione di petrolio, gas naturale e prodotti chimici e attraversano sia regioni urbane che extraurbane del territorio. A causa dei severi rischi connessi con i possibili sversamenti di questi prodotti, gli aspetti di sicurezza e di manutenzione di queste infrastrutture risultano essere scrupolosamente controllati, così da prevenire il verificarsi di infortuni, incidenti fatali o disastri ambientali. Per questo motivo, il dipartimento dei trasporti degli Stati Uniti ha fondato la divisione Pipeline and Hazardous Materials Safety Administration (PHMSA) per poter identificare e valutare i rischi delle condotte oil & gas, così da programmare le operazioni di mantenimento e di ristrutturazione prima che si verifichino sversamenti. Quest'organizzazione si impegna, inoltre, a pubblicare dei resoconti annuali sulle principali cause che hanno causato incidenti nelle condotte, in particolar modo, si osserva che i fenomeni corrosivi rappresentano circa il 20% delle cause di danno, come riportato in Figura 1.1 e 1.2. I gasdotti e gli oleodotti sono caratterizzati da un ciclo vita abbastanza prolungato, ciò fa sì che molti di questi condotti tutt'oggi in funzione sono stati costruiti con tecnologie e materiali ormai sorpassati e progressivamente si avvicinano al termine della loro vita di esercizio. Osservando Figura 1.8, si comprende che circa il 50% dei condotti negli US sono stati costruiti fra gli anni '50 e '60 e quindi tendono gradualmente a danneggiarsi e a presentare sversamenti sempre più frequenti. È un dato di fatto che progressivamente, nel tempo, le condotte danneggiate e ormai a fine vita dovranno essere completamente sostituite. È stata quindi studiata la possibilità di utilizzare un rivestimento interno di vetro borosilicato come valida alternativa ai tradizionali rivestimenti in resina epossidica, così da fornire un'ottima resistenza a corrosione del substrato metallico, ridurre le cadute di pressione durante il trasporto del fluido, aumentare l'efficienza del flusso riducendo l'energia richiesta per il trasporto e ottenere un'adesione chimica all'interfaccia fra il coating e il substrato, così da evitare l'innesco di processi di corrosione interstiziale.

Nell'ambito di questo progetto di ricerca della Missouri University of Science and Technology si colloca questo lavoro di tesi, in particolar modo, è stato realizzato un modello dinamico che valuta l'interazione suolo-tubo, in un condotto interrato rivestito internamente con un coating di vetro borosilicato, durante il passaggio di un fluido che induce vibrazioni nel condotto. Come prima cosa è stato individuato un modello di suolo che potesse rappresentare con buona approssimazione un suolo reale, si è dunque scelto il modello di suolo elastico alla Winkler, in cui il suolo è descritto come un letto di molle indipendenti con comportamento elastico. L'Equazione (3.1) rappresenta l'equazione costitutiva per questo modello.

Per analizzare le vibrazioni indotte da un fluido in una tubatura priva di rivestimento è stata utilizzata la teoria dell'elasticità lineare. Si considera quindi una tubatura con sezione omogenea di raggio  $R$  e lunga  $L$ , incastrata ad entrambe le estremità, in cui fluisce un fluido con velocità  $v$ . Si scrive l'equazione di bilancio delle forze nella struttura, come mostrato in Equazione (3.2). In cui  $F_{bend}$  rappresenta la reazione alla distorsione della struttura,  $F_{cent}$  è la forza centripeta dovuta alla curvatura della tubatura,  $\sigma_T$  è la reazione del suolo secondo il modello di Winkler,  $m$  è la massa totale della struttura, data dalla somma della tubatura e del volume di fluido diviso per l'unità di lunghezza e  $y$  è lo spostamento nella direzione trasversale all'asse del tubo che dipende dall'istante di tempo  $t$  considerato. Effettuando una serie di sostituzioni e approssimazioni, mostrate dall'Equazione (3.3) a (3.7), si ottiene la forma finale dell'equazione che descrive l'andamento delle vibrazioni della tubatura nel tempo, riportata in Equazione (3.8). L'equazione ottenuta è un'equazione differenziale alle derivate parziali e può essere risolta utilizzando le quattro condizioni al contorno, illustrate in Equazione (3.9), (3.10), (3.11) e (3.12), è una condizione iniziale, mostrata in Equazione (3.13). La soluzione di questo problema viene studiata con l'ausilio del programma MATLAB, come specificato, in Appendice 9.1 si riporta il codice utilizzato per risolvere l'equazione differenziale presentata precedentemente. Per poter comprendere completamente i risultati è necessario andare a confrontare le curve che si ottengono utilizzando MATLAB con la massima deflessione nella direzione  $y$  ammissibile nella struttura  $y_{max}$ . Soltanto se la massima deflessione osservabile nel tempo nella tubatura è inferiore alla deflessione massima stimata si può concludere che le vibrazioni non inducono deformazioni permanenti nel condotto. Per ricavare il valore di  $y_{max}$  si effettuano alcune assunzioni, la tubatura è considerata come una trave doppiamente incastrata soggetta ad un carico uniforme, come illustrato in Figura 3.4. La massima deflessione per una tradizionale trave risulta essere nota e mostrata per chiarezza in Equazione (3.14), sostituendo il momento di inerzia per una sezione tubolare all'interno dell'equazione precedente e sfruttando la formula di Navier, riportata in Equazione (3.16), infine, si ottiene che la massima deflessione  $y_{max}$  del condotto dipende dal diametro interno  $d$  ed esterno  $D$  del tubo, dalla sua lunghezza  $l$ , dal modulo elastico  $E$  e dal carico di snervamento  $\sigma_y$  del materiale, come mostrato in Equazione (3.20). La metodologia scelta per l'ottenimento dei risultati, si basa nel mantenere costante tutte le variabili in gioco nell'Equazione (3.8), eccetto una è lasciata libera di variare, con lo scopo di poter comprendere in modo chiaro come questo parametro influenza le vibrazioni del condotto. In particolar modo, si analizza l'andamento delle oscillazioni nella tubatura al variare del diametro, in Sezione 3.1.3.1, al variare della costante del suolo  $K_s$ , in Sezione 3.1.3.2, al variare della densità del fluido, in Sezione 3.1.3.3, e al variare della velocità del fluido all'interno del condotto. Per quanto riguarda l'analisi di quest'ultimo caso, è necessario introdurre il concetto di regime turbolento e laminare e tenere in considerazione un numero caratteristico che permette la descrizione di questi fenomeni, il numero di Reynolds  $Re$ . Stimando, infatti, il valore di questo numero per tre diversi casi di caduta di pressione  $\Delta P$  tra la sezione d'ingresso e d'uscita del condotto, si osserva dei valori di velocità del flusso troppo

elevati, di conseguenza il numero di Reynolds risulta essere nettamente maggiore di 2100 quindi si può concludere che il profilo fluidodinamico nel condotto risulta essere completamente turbolento. Dunque, non si può calcolare la velocità del flusso applicando la tradizionale formula di Poisselle per il regime laminare, ma è necessario analizzare l'equazione di bilancio energetico per il condotto in analisi, mostrata in Equazione (3.22), inoltre, supponendo valide le ipotesi illustrate in Equazione (3.23), (3.24) e (3.25), si ricava l'Equazione (3.26) dove la perdita di energia dovuta all'attrito  $R$  è uguale alla caduta di pressione  $\Delta P$  nella tubatura diviso per la densità del fluido. Ricordando che  $R$  può essere espresso tramite l'Equazione (3.27), allora  $R$  dipende direttamente dal coefficiente d'attrito di Darcy  $\xi$ , che può essere facilmente valutato utilizzando il diagramma di Moody, riportato in Figura 3.6. Si osserva che questo diagramma mostra che  $\xi = \xi\left(\frac{\epsilon}{D}, Re\right)$ , dove  $\epsilon$  rappresenta la rugosità superficiale e  $D$  è il diametro della tubatura, dunque, il rapporto  $\frac{\epsilon}{D}$  prende il nome di rugosità relativa. Analizzando il diagramma di Moody si comprende che quando il numero di Reynolds è sufficientemente grande, il coefficiente di Darcy  $\xi$  non dipende più da  $Re$ . Quindi sperimentalmente si determina il rapporto  $\frac{\epsilon}{D}$  per il sistema in esame, successivamente si osserva il diagramma di Moody per ricavare il coefficiente di Darcy  $\xi$ . Noto questo valore, si sfrutta l'Equazione (3.31) per calcolare la velocità del flusso nel condotto quando si ha una specifica perdita di pressione  $\Delta P$ . I valori di  $\Delta P$  e di velocità del flusso considerati sono mostrati in Tabella 3.4.

Una volta analizzato l'andamento delle vibrazioni in una condotta non rivestita si procede con l'introduzione del modello matematico che descrive il comportamento di un condotto rivestito internamente con lo smalto ceramico. L'Equazione (3.8), vista precedentemente, che permetteva di prevedere le vibrazioni di una tradizionale tubatura viene opportunamente modificata per tenere in considerazione la presenza del coating. L'equazione che si ottiene in questo caso è, anch'essa, un'equazione differenziale alle derivate parziali, permettendo la descrizione delle oscillazioni nel nuovo sistema come mostrata in Equazione (3.31). In particolare, in quest'equazione si osserva che le componenti che subiscono una modifica sono, il primo, che rappresenta la rigidità flessionale, dove si tiene conto sia del contributo della tubatura sia della presenza del coating, ed il secondo, che è associato allo spostamento che subisce la condotta nel tempo, si osserva che la massa totale tiene conto di tre diversi contributi, la massa del tubo, la massa del fluido e la massa del coating. La soluzione di quest'equazione viene studiata attraverso il software MATLAB, applicando il codice riportato in Appendice 9.2 ed utilizzando le stesse condizioni al contorno e iniziale presentate precedentemente in Equazione (3.9), (3.10), (3.11) e (3.12). Anche per l'analisi di questo sistema si utilizza la stessa strategia, vista precedentemente, cioè si assumono costanti tutte le variabili eccetto una, che viene lasciata libera di modificare il suo valore. In ordine, si studia l'andamento delle vibrazioni nel condotto rivestito al variare del diametro della tubatura, presentato in Sezione 3.1.7.1, al variare dello spessore del coating, mostrato in Sezione 3.1.7.2, al variare della costante del suolo, presentato in Sezione 3.1.7.4, ed al variare della velocità del flusso nella tubatura, illustrato in Sezione 3.1.7.3. Analizzando in specifico quest'ultimo caso, si osserva che il regime di moto del fluido è turbolento allora la velocità del fluido è ricavata utilizzando il diagramma di Moody, per le stesse cadute di pressione  $\Delta P$  viste precedentemente nella condotta non rivestita.

I risultati relativi a questi due modelli sono presentati in Sezione 4.1 e 4.2, dove in entrambi i casi si considera un periodo di analisi di 10 s. L'andamento complessivo del profilo di vibrazione può cambiare significativamente a seconda dei valori assunti dalle variabili, ma si nota che in nessun caso la deflessione massima osservata supera il valore limite  $y_{max}$ , che porta

in deformazione plastica la struttura. In merito alla tubatura non rivestita, si osserva che all'aumentare del diametro si ha una riduzione dell'ampiezza di oscillazione e una perdita del profilo sinusoidale, come mostrato in Figura 4.1. Invece, al variare della costante del suolo, sia per terreni ghiaiosi che sabbiosi si osserva che le vibrazioni assumono un profilo variabile che mantiene costante l'ampiezza di oscillazione anche se si ha uno spostamento periodico dell'asse neutro, come presentato in Figura 4.2 e 4.3. Per quanto riguarda la dipendenza delle vibrazioni dalla velocità del flusso, osservando Figura 4.4, si può concludere che il profilo delle oscillazioni del condotto rimane invariato all'aumentare della velocità del flusso. Infine la Figura 4.5 mostra l'andamento delle vibrazioni al variare della densità del fluido, in particolare, in questo caso si considerano tre diverse specie di liquidi acqua, petrolio e benzina. I grafici mostrano una forte dipendenza dalla densità, infatti, si osservano profili di vibrazione completamente differenti. A seguire vengono presentati i risultati delle simulazioni MATLAB ottenute per le condutture rivestite con il coating. In questo caso, si nota che aumentando in diametro della tubatura non si verifica una modifica del profilo di vibrazione, le oscillazioni, infatti, hanno un andamento sinusoidale, come mostrato in Figura 3.6. La principale differenza tra i grafici è l'ampiezza di vibrazione che tende a diminuire all'aumentare del diametro. Per quanto riguarda l'influenza dello spessore del rivestimento sulle vibrazioni, sono stati testati due diversi spessori, associati a due diverse tecniche di deposizione, lo spessore di 230  $\mu\text{m}$  ottenuto da T-001 slurry e lo spessore di 340  $\mu\text{m}$  ottenuto da GP2118 in polvere. In entrambi i casi, osservando le Figure 4.6 e 4.7, non si presenta una variazione significativa del profilo di vibrazione della tubatura allora lo spessore del coating non è un parametro che influenza la dinamica del tubo. Invece, come mostrato in Figura 4.8, la variazione della velocità del fluido modifica significativamente l'andamento delle oscillazioni, in particolare, si ha un andamento completamente irregolare delle curve già a partire da cadute di pressione di 14 bar. In ultima analisi, si considera la variazione della costante del suolo  $K_s$ , nel caso di suoli sabbiosi con valori di  $K_s$  contenuti si ha un andamento delle vibrazioni abbastanza regolare, ma al crescere del valore di  $K_s$  si osserva una maggiore irregolarità del profilo ma complessivamente il trend ha una certa periodicità. Al contrario, per i suoli ghiaiosi l'andamento delle vibrazioni è completamente irregolare ma la deformazione massima rimane sempre contenuta e inferiore al limite di snervamento, come mostrano le Figure 4.9 e 4.10.

### **3. Tondini d'acciaio rivestiti con Coating Ceramici di Vetro Borosilicato**

In questa sezione viene studiata l'efficacia e le performance del rivestimento di vetro borosilicato nel prevenire la corrosione. In particolare, si testano in contemporanea dei tondini d'acciaio tradizionale, privi di rivestimento, e dei tondini rivestiti con resina epossidica, che possono servire da confronto. I tondini d'acciaio scelti per quest'analisi presentano un diametro di 2.54 cm (1 inch), e vengono divisi in tre gruppi, uno destinato ad essere rivestito con il coating ceramico, con il processo precedentemente illustrato, un gruppo viene sottoposto ad un'operazione di spazzolatura per rimuovere gli ossidi superficiali, per poi essere rivestito con resina epossidica ed infine l'ultimo gruppo viene lasciato nel suo stato ossidato superficialmente. Successivamente, i tondini vengono tagliati in campioni di 5.08 cm (2 inches) di lunghezza. Per i campioni rivestiti con il coating ceramico è necessario marcare con resina epossidica la superficie dove si vuole eseguire il taglio, con lo scopo di evitare un eccessivo danneggiamento del rivestimento. A seguire, ogni sezione dei campioni viene connessa con un filo di rame utilizzando un foglio di rame adesivo, come mostrato in Figura 3.8. Dopodiché, utilizzando LOCTITE® Epoxy Marine, si riveste le sezioni di tutti i campioni e la superficie di

campioni precedentemente spazzolati, si lascia reticolare la resina epossidica per tre giorni prima di iniziare i test elettrochimici. I provini vengono divisi e un gruppo è immerso in una soluzione 3.5 %wt di NaCl, per valutare la esistenza a corrosione in presenza di cloruri, e l'altro in una soluzione satura di  $\text{Ca}(\text{OH})_2$  con pH 14, per simulare le condizioni ambientali all'interno del calcestruzzo armato. I campioni vengono monitorati per 70 giorni, settimanalmente nel primo mese di immersione e poi ogni due settimane fino al termine della prova. In specifico, si misurano l'Open Circuit Potential (OCP) cioè il potenziale misurato fra l'elettrodo di misura e l'elettrodo di riferimento quando non si applica un potenziale esterno, la Linear Polarization Resistance (LPR), che misura la resistenza del materiale ad essere polarizzato, generalmente questo valore viene calcolato con lo scopo di ricavare la corrente di corrosione ( $i_{\text{corr}}$ ), ed infine, si misura Electrochemical Impedance Spectroscopy (EIS), in cui si va a misurare il modulo dell'impedenza del sistema e l'angolo di fase fra il potenziale sinusoidale applicato e il segnale di corrente alternato misurato. Queste analisi vengono effettuate accoppiando Interface 1000E Potentiostat/Galvanostat con ECM8 Electrochemical Multiplexer, prodotti da Gamry Instruments. In specifico, per l'analisi OCP, si monitora l'andamento del potenziale per 1h, a seguire si effettua l'analisi EIS, in cui si applica un potenziale sinusoidale di 10 mV, in corrispondenza del valore di OCP misurato precedentemente, e con una frequenza tra 100 kHz e 5 mHz. Infine, si esegue l'analisi LPR, applicando un potenziale di  $\pm 15$  mV rispetto al valore di OCP misurato e con una velocità di scansione di 0.167 mV/s. Per chiarezza il set-up di queste prove viene riportato nelle Figure 3.12, 3.13, 3.14 e 3.15. Una volta raccolti i dati provenienti dalle analisi EIS, si è ipotizzato un modello di circuito elettrico equivalente (EEC) che fosse in grado di prevedere il comportamento del coating immerso in soluzione. Sono stati realizzati due circuiti equivalenti, mostrati in Figura 3.19, il primo valido nei primi 18 giorni di test, quando i fenomeni di trasporto di massa sono predominanti, le molecole di acqua e di ossigeno arrivano in prossimità della superficie del coating e promuovono le reazioni di corrosione nei punti dove il coating risulta danneggiato. Il secondo, invece, valido dal 18esimo fino al 70esimo giorno, è costituito dagli stessi elementi del primo circuito, ad eccezione dell'elemento di impedenza di Warburg, che tiene conto del contributo diffusivo sulla superficie del coating, a causa della presenza dell'accumulo dei prodotti di corrosione. Osservando Figura 3.19,  $R_s$  rappresenta la resistenza della soluzione,  $R_c$  la resistenza del coating,  $R_{ct}$  la resistenza al trasferimento della carica,  $\text{CPE}_c$  e  $\text{CPE}_{dl}$  sono degli elementi a fase costante, con un comportamento intermedio tra quello resistivo e quello capacitivo, e tengono conto del contributo capacitivo del coating  $\text{CPE}_c$  e della presenza del doppio strato elettrico all'interfaccia campione-soluzione  $\text{CPE}_{dl}$ .

Al termine dei test elettrochimici i campioni vengono propriamente preparati per effettuare l'analisi SEM, così da poter osservare con maggior dettaglio la morfologia e la microstruttura del rivestimento smaltato e di quello epossidico dopo 70 giorni a contatto con le soluzioni aggressive. L'apparecchiatura utilizzata in questo specifico caso è Helios NanoLab DualBeam. Innanzitutto, si monta la resina epossidica sui campioni che si vuole osservare, dopodiché si tagliano i campioni di tondini d'acciaio rivestiti così da ottenere delle sezioni di 5cmx5cmx0.5cm. Le superfici da osservare vengono lucidate e un sottile layer (5 -10 nm) di Pd/Au viene depositato sulla superficie, così da poter osservare le superfici dei materiali non conduttivi ed evitare all'accumulo di carica sulla superficie. In fine, i campioni vengono opportunamente posizionati sul porta campioni e immessi all'interno del Helios.

I risultati dei test di potenziale a circuito aperto (OCP) nelle Figure 4.11 e 4.12 mostrano in entrambe le soluzioni un andamento decrescente, anche se per la soluzione di  $\text{Ca}(\text{OH})_2$  essendo questo trend più marcato i valori iniziali di potenziale tendono a localizzarsi fra -0.3 V e -0.45 V. Al contrario nella soluzione di NaCl i valori di potenziale misurato nel primo periodo

tendono ad essere leggermente inferiori e si localizzano fra -0.5 V e -0.6 V. Tutte le curve tendono a decrescere nei primi 30 giorni ma a seguire tendono ad un valore costante. Per quanto riguarda il grafico dell'analisi OCP in NaCl, mostrato in Figura 4.11, si osserva che i campioni rivestiti con resina epossidica presentano il potenziale più elevato per i primi 40 giorni, ma a seguire il valore del potenziale tende a diminuire in modo significativo, così che i campioni rivestiti con lo smalto ceramico mostrano un potenziale a circuito aperto più alto di -0.62 V. Invece, i risultati OCP per i campioni immersi nella soluzione di Ca(OH)<sub>2</sub> mostrano un profilo più irregolare rispetto ai precedenti, in particolare, i provini rivestiti con lo smalto ceramico partendo da polveri presentano un potenziale più elevato per tutto il periodo di prova, ma sarà soltanto dopo il 30esimo giorno che i campioni rivestiti con la tecnica slurry mostreranno un valore di potenziale comparabile con quello dei provini con rivestimento ottenuto da polveri. Per quanto riguarda invece i campioni non rivestiti e quelli rivestiti con resina epossidica, si osserva che acquistano un potenziale nettamente inferiore e intorno a -0.7 V.

Le Figure 4.13 e 4.14 mostrano l'andamento della resistenza a polarizzazione dei campioni. Nella soluzione di NaCl si osserva che tutti i campioni rivestiti presentano valori di resistenza comparabili e con un trend complessivo decrescente di circa  $10^5 \Omega/\text{cm}^2$ . Al contrario per i campioni non rivestiti il valore di resistenza è significativamente inferiore di circa 4 ordini di grandezza, ciò fa sì che il passaggio di corrente possa avvenire con più facilità. Per quanto riguarda i campioni immersi nella soluzione di Ca(OH)<sub>2</sub>, si osserva anche in questo caso un andamento complessivo delle curve è decrescente, i valori di resistenza più elevati di circa  $10^6 \Omega/\text{cm}^2$  sono associati ai campioni rivestiti con materiale ceramico anche se i provini rivestiti con resina epossidica sono localizzati ad un solo ordine di grandezza di distanza. I provini invece non rivestiti mostrano un valore di resistenza a polarizzazione nettamente inferiore di circa  $10^2 \Omega/\text{cm}^2$ . I risultati di LPR sono sfruttati per ricavare la corrente di corrosione  $i_{\text{corr}}$  nei sistemi, come mostrato nelle Figure 4.15 e 4.16. Se si osserva l'andamento delle curve nella soluzione di NaCl presentano un trend crescente nei primi 40 giorni fino a che non raggiungono un valore costante. Le curve associate ai provini rivestiti con lo smalto di vetro borosilicato mostrano il valore di densità di corrente di corrosione più contenuto attorno a  $10^{-6} \text{ A}/\text{cm}^2$ , anche se la curva per i campioni rivestiti con resina epossidica tende ad essere prossima alla precedente. Al contrario, come ci si aspetta dalla curva della resistenza di polarizzazione, la curva dei campioni non rivestiti è nettamente spostata a valori di densità di corrente più alti. Analizzando Figura 4.14 dove vengono illustrati i risultati di densità di corrente di corrosione per i campioni immersi nella soluzione di Ca(OH)<sub>2</sub>, si osserva che l'andamento complessivo delle curve è molto simile a quello visto per i provini in soluzione di NaCl, anche se il gap tra la curva dei tondini rivestiti con resina epossidica è maggiormente distanziata rispetto a quella dei rivestimenti ceramici. In conclusione, possiamo dire che i materiali che presentano una resistenza a polarizzazione più alta e una densità di corrosione più bassa sono i materiali che presentano delle prestazioni contro la corrosione più elevate.

I risultati finali ottenuti per le analisi EIS sono mostrati nelle Figure 4.17 a 4.24, dove si osserva che i grafici A presentano l'andamento del modulo dell'impedenza in funzione della frequenza, invece, i grafici B mostrano il trend dell'angolo di fase al variare della frequenza. In specifico, le Figure da 4.17 a 4.20 presentano i risultati relativi ai campioni immersi nella soluzione di NaCl invece le Figure da 4.21 a 4.24 mostrano i risultati dei provini immersi nella soluzione di Ca(OH)<sub>2</sub>. Un coating che è intatto, privo di difetti superficiali che non lasciano esposto il substrato presentano un andamento delle curve del modulo di impedenza con un plateau a basse e medie frequenze, seguito da una progressiva diminuzione delle pendenze delle curve raggiunte le alte frequenze. I campioni che hanno questo trend in entrambi le soluzioni sono solamente i campioni rivestiti con resina epossidica, mostrati in Figura 4.19A e 4.23A. Inoltre,

si osserva che nella soluzione di NaCl con l'aumentare dei giorni la regione di plateau tende ad estendersi verso le frequenze più elevate, nel frattempo, si ha una diminuzione del valore di impedenza. Questo comportamento è da associarsi alla graduale penetrazione della soluzione attraverso il coating che porta ad una riduzione della resistenza del coating e ad un aumento del termine capacitivo. Osservando i diagrammi di Bode per i campioni rivestiti con lo smalto vetroso, mostrati in Figura 4.19A e 4.20A, le curve mostrano un trend completamente decrescente, senza la presenza del plateau iniziale, questo indica la presenza di difetti nel rivestimento, come aperture e pinholes. Confrontando, però questi grafici con le Figure 4.21A e 4.22A, risulta evidente che nei primi giorni d'immersione l'andamento è simile ma con il passare del tempo le curve tendono a ridurre la loro pendenza e a tendere sempre di più all'orizzontalità, ciò è dovuto alla parziale formazione nei punti di esposizione del substrato di un film di passività che riduce la velocità di corrosione. Per quanto riguarda i campioni rivestiti in soluzione di  $\text{Ca}(\text{OH})_2$  si osserva che a basse frequenze il valore di impedenza è sempre maggiore di  $10^5 \Omega \cdot \text{cm}^2$ , ciò significa che il processo corrosivo non prosegue e il coating fornisce una buona protezione alla superficie. Al contrario, nei provini immersi nella soluzione di NaCl, si osserva che l'impedenza è maggiore di  $10^5 \Omega \cdot \text{cm}^2$  soltanto nei primi giorni, ma dopodiché, scende a valori inferiori e la corrosione del substrato inizia, seppur con velocità contenute. Per avere un quadro completo della situazione sono stati testati anche i tondini privi di rivestimento in queste due soluzioni come termini di confronto, i diagrammi sono mostrati in Figura 4.22A e 4.24A. Nella soluzione di NaCl, complessivamente le curve hanno una pendenza negativa molto accentuata già a basse frequenze, con un valore di  $|Z|$  attorno a  $10 \Omega \cdot \text{cm}^2$ . Dunque, la superficie tende a corrodarsi liberamente senza la presenza di rivestimenti. Nella soluzione di  $\text{Ca}(\text{OH})_2$ , le curve a basse frequenze tendono ad avere una pendenza più contenuta rispetto al caso precedente, comunque, anche se si dovrebbe avere la formazione di una strato di passività, questo non risulta essere uniforme e continuo, quindi la corrosione prosegue anche in questo caso. I diagrammi di Bode mi permettono di avere informazioni sia sull'impedenza dei campioni, ma anche sull'andamento dell'angolo di fase fra il potenziale AC applicato e la corrente AC misurata. Le informazioni fornite da queste curve sono complementari a quelle dei diagrammi dell'impedenza, ma a volte permettono di avere una visione complementare e d'insieme migliore. Analizzando Figura 4.19B e 4.23B, si comprende che quando il coating risulta essere continuo e fornisce una buona protezione, l'angolo di fase è uguale a  $0^\circ$  a basse e medie frequenze, poi cresce rapidamente ad alte frequenze fino a raggiungere  $-90^\circ$ . Inoltre, con l'aumentare del tempo di immersione in entrambi i diagrammi, si ha uno spostamento delle curve verso il basso, associato proprio alla penetrazione della soluzione attraverso il coating. Confrontando i grafici precedenti con le Figure 4.17B, 4.18B, 4.21B e 4.22B relativi ai rivestimenti ceramici, si osserva che le curve anche se ad alte frequenze raggiungono  $-90^\circ$ , presentano però notevoli oscillazioni che sono una conferma della presenza di difetti sulla superficie dei rivestimenti. Questo andamento è presente sia nei provini immersi nella soluzione di NaCl che di  $\text{Ca}(\text{OH})_2$ . Per quanto riguarda i campioni non rivestiti, mostrati in Figura 4.20B e 4.24B, si osserva che quando la corrosione procede liberamente, cioè nella soluzione di NaCl, le curve mostrano dei valori di angoli di fase negativi a basse frequenze che progressivamente crescono fino a raggiungere valori positivi, invece per la soluzione di  $\text{Ca}(\text{OH})_2$ , si osserva che le curve presentano un angolo di fase vicino a  $0^\circ$  a basse e medie frequenze, però ad alte frequenze le curve non raggiungono  $-90^\circ$ , ma si arrestano a  $-60^\circ$ , chiaro segno che le superfici non sono completamente protette, come era stato ipotizzato nella curva dell'impedenza.

I risultati delle analisi EIS sono inoltre utilizzati per realizzare un modello di circuito equivalente (EEC) che permette di prevedere in modo teorico i valori di resistenza e di capacità di tutti gli elementi che compongono il sistema reale in cui i campioni sono immersi.

In particolare, per entrambe le soluzioni è monitorato l'andamento della resistenza e della capacità del coating, la resistenza al trasferimento di carica e la capacità del doppio strato elettrico all'interfaccia con la soluzione per 70 giorni, come mostrato nelle Figure da 4.25 a 4.32. Osservando la Figura 4.29 dove è mostrato l'andamento della resistenza del coating nella soluzione di NaCl, si osserva che le curve assumono un andamento decrescente nei primi 20 giorni poi assume un andamento costante a circa  $10^4 - 10^5 \Omega \cdot cm^2$ . In particolare, il rivestimento epossidico presenta il valore di resistenza più elevato, seguito dal rivestimento ceramico ottenuto da polveri e poi, per ultimo, seguito dal rivestimento ceramico prodotto tramite tecnica slurry. Per quanto riguarda la capacità del coating, il suo andamento è mostrato in Figura 4.30 e risulta completamente opposto a quello della resistenza, infatti, il coating epossidico presenta i valori più contenuti fra  $10^{-9}$  e  $10^{-10} 10^5 \Omega \cdot cm^2$  e a valori più elevati si trovano i coating ceramici. Il diagramma associato alla resistenza al trasferimento di carica, mostrato in Figura 4.31, presenta un andamento delle curve decrescente ma tra il 30esimo e il 40esimo giorno si osserva una variazione del trend delle curve. Infatti, se nei primi 30 giorni il rivestimento epossidico presenta i valori di resistenza più elevati, durante questo periodo la situazione si inverte, infatti, i rivestimenti diminuiscono sensibilmente la loro resistenza, così che i coating ceramici hanno una resistenza superiore dal 40esimo giorno fino al termine delle prove. La capacità del doppio strato elettrico presenta anch'esso un'inversione di tendenza tra il 30esimo e il 40esimo giorno, solo che in questo caso i valori di capacità più elevati sono associati ai provini con coating ceramico fino al 30esimo giorno e poi ai campioni con rivestimento epossidico dal 40esimo giorno fino al termine delle prove. In definitiva, i rivestimenti che presentano una migliore resistenza a corrosione sono a lungo termine i rivestimenti di smalto di vetro borosilicato poiché il loro valore di resistenza al trasferimento di carica e la capacità del doppio strato sono rispettivamente il più alto e il più basso. Al contrario, il rivestimento epossidico sebbene mostri ottime proprietà, superiori al coating ceramico, nei primi 30 giorni, a lungo termine questo tende a perdere la sua efficacia. A seguire si studia gli stessi grafici, visti precedentemente, per i campioni immersi in soluzione  $Ca(OH)_2$ . Figura 4.25 mostra il trend della resistenza del coating, si osserva un andamento leggermente decrescente nei primi 10 giorni che però raggiunge un valore costante in tutti e tre i rivestimenti. In specifico, il coating epossidico ha un valore di resistenza di un ordine di grandezza più elevato rispetto al rivestimento ceramico, posizionato a  $10^4 - 10^5 \Omega \cdot cm^2$ . Comparando questo grafico con Figura 4.26, dove si mostra le curve relative alla capacità del coating, si osserva, anche in questo caso, che il profilo delle curve è completamente opposto. Il rivestimento epossidico presenta la curva con valore più piccolo e i rivestimenti con smalto di vetro hanno le curve con valori più elevati di capacità. Il principale motivo per la quale si studia questa curva è per valutare l'efficacia del processo diffusivo della soluzione attraverso il rivestimento. Dopodiché, si analizza l'andamento delle curve della resistenza al trasferimento di carica, illustrata in Figura 4.27, l'andamento delle curve è complessivamente decrescente, ma i campioni rivestiti con resina epossidica presentano una resistenza significativamente più bassa di circa due ordini di grandezza rispetto ai campioni con coating ceramico. Nello stesso modo, anche il grafico associato alla capacità del doppio strato, presenta nei primi 20 giorni un valore di capacità minore per i campioni epossidici, ma con il passare dei giorni a causa dell'andamento crescente delle curve, i valori dei campioni epossidici superano quelli dei provini con rivestimento in vetro. Dunque, i rivestimenti con smalto in vetro borosilicato anche in soluzione di idrossido di calcio presentano una migliore resistenza alla corrosione, rispetto al rivestimento tradizionalmente utilizzato in resina epossidica.

I risultati ottenuti dall'analisi SEM (Figure 4.33 a 4.38) mostrano che i campioni con smalto ceramico hanno un'elevata porosità chiusa dovuta dalla formazione di anidride carbonica durante lo step ad alta temperatura in forno, che promuove la reazione tra il carbonio in lega e gli ossidi del rivestimento. Inoltre, osservando l'interfaccia si osserva la presenza di piccole

protrusioni metalliche che si articolano all'interno del rivestimento ceramico, in questo modo si ha un aumento della superficie di contatto tra i due materiali che porta ad un aumento della forza di adesione all'interfaccia. La tipica struttura irregolare con asperità che si osserva in questi campioni è dovuto ad un'alta compatibilità tra il substrato e il rivestimento, che porta alla formazione di legami chimici fra i due materiali. Osservando, invece, i campioni rivestiti con resina epossidica; sebbene il rivestimento sia compatto e privo di porosità, all'interfaccia si ha una completa perdita di adesione che porta alla formazione di uno strato intermedio di corrosione, come mostrano le Figure 4.37B e 4.38B. I due materiali che costituiscono il rivestimento e il substrato in questo caso non sono compatibili chimicamente quindi la forza che assicura l'adesione è unicamente di tipo meccanico e non è sufficiente a prevenire fenomeni di corrosione interstiziale.

#### 4. Conclusione

Per concludere, i risultati forniti dal modello matematico per prevedere il comportamento di un coating ceramico in presenza di un condotto in vibrazione, descrivono in modo veritiero ciò che avviene nei casi reali. In particolare, si osserva una dipendenza del profilo delle vibrazioni sia dal diametro del condotto, sia dallo spessore del coating che dalla costante del suolo. Al contrario, la velocità del fluido che attraversa la condotta non influisce sensibilmente nella dinamica delle vibrazioni. Inoltre, dando una visione di insieme a tutti i risultati ottenuti, si conclude che il profilo di vibrazione è fortemente affetto dai parametri di processo ma in nessun caso la deflessione massima della condotta supera il limite di snervamento del materiale, ciò significa che la struttura lavora in campo elastico per il periodo di tempo analizzato. Come sviluppo futuro, per comprendere in maggior dettaglio il comportamento del rivestimento nel modello dinamico sarebbe interessante creare un modello simulativo in ANSYS, così da poter studiare in maggior dettaglio come il regime di flusso influenza le vibrazioni.

I risultati relativi alle prestazioni del rivestimento con vetro borosilicato nell'ostacolare i processi corrosivi, mostrano un'ottima resistenza a corrosione di questo materiale, purtroppo a causa dell'irregolarità del substrato e delle reazioni promosse durante il ciclo termico che portano alla formazione di anidride carbonica, non è possibile la realizzazione di un rivestimento omogeneo e continuo privo di difetti. Questa problematica affligge sia il rivestimento ottenuto partendo da slurry che da polveri. Comparando i diagrammi di Bode per i campioni rivestiti con resina epossidica con quelli rivestiti con il coating ceramico, si osserva che la qualità del coating epossidico ha una qualità nettamente superiore dal punto di vista morfologico, ciò è anche confermato anche dalle immagini SEM. Sfortunatamente, però questo rivestimento a causa della scarsa adesione all'interfaccia è più sensibile al processo di degradazione, infatti, già dopo 30 giorni di immersione in soluzione di NaCl le curve EEC del circuito equivalente mostrano un sensibile riduzione della resistenza al trasferimento di carica, inoltre, osservando gli ingrandimenti all'interfaccia resina epossidica/metallo si ha la presenza di un sottile strato di ossidi di corrosione (Figure 4.37B e 4.38B). Le come confermato dalle curve che descrivono il circuito equivalente (EEC) nelle Figure 4.31 e 4.32.



## Introduction

Metals exist on the Earth's crust in the form of minerals such as oxides, carbonates, sulfides, and sulfates. Thanks to technical innovations, more and more metallurgical processes are developed to reduce the minerals in the desired metals or alloys. After that, these materials are properly shaped into beams, pipes, rebars or sheets, which are commonly used in civil and industrial sectors. Unfortunately, all metals and alloys exposed to natural environments are not at their thermodynamic lowest energy state [1]. For this reason, metals and alloys fatally react with the earth's atmosphere transforming back to oxidated or carbonates state. These phenomena are generally known as corrosion. The corrosion affects the energetic, chemical, petrochemical, mechanic, and transportation sectors. The direct cost of metallic corrosion is around \$276 billion per year, approximately 3.1% of the U.S. Gross Domestic Product (GDP) [3]. Regarding the civil infrastructure as bridges and pipelines, most of them were built in the 50s and they are getting at the end of their life-cycle as the US Department of Transportation mentioned [4, 22]. For these structures, the main failure reason is often related to the corrosion phenomena. Therefore, news monitoring technology is developed and is used to identify deficient bridges or pipeline leaks. To avoid corrosion phenomena, the use of protective coating is a consolidated technique that is widely diffused as mentioned in [40]. Unfortunately, polymer coatings have a life span of around 10 years, which is extremely lower compared to the hypothetical life-span of a pipeline or a bridge. Furthermore, the coating adhesion on the metal surface is only mechanical so as time goes on there is a loss of adherence at the interface and consequently promoting crevice corrosion [2]. For this reason, in the last years, the research is based on finding the possible replacement to epoxy coating using other materials that provide better interfacial adhesion and a longer life cycle [41].

Specifically, this thesis work deals with this topic and it is focused on the performance evaluation of enamel coating in two different structures, bridges and pipelines. In the pipeline, the enamel coating is deposited on the inner diameter in order to prevent the starting of the corrosion phenomena. Nevertheless, in this work, the pipeline corrosion aspect is not the focal point, but it focuses on predicting the enamel coating behavior when pipeline dynamic vibration occurs. On the other hand, in bridges structures, it is studied the corrosion resistance of enamel coated rebars compared to traditional epoxy coated ones. In particular, the specimens are tested in a 3.5%wt NaCl solution and in a saturated solution of  $\text{Ca}(\text{OH})_2$  with pH 14. These tests are done on two types of enamel coatings obtained with different production processes such as powder and slurry deposition.

This thesis is divided into five main sections. At the beginning an overview is presented of the actual situation of oil and gas pipelines and bridges, in particular, with an in-depth analysis of the principal corrosion mechanisms that affect these structures. This is followed by the material section, where the enamel coating chemical composition and the manufacturing technology are mentioned. After that, there is the method section in which the theoretical models and the experimental techniques that are used in this thesis work are described. Firstly, the vibrations pipeline model is illustrated and secondly, the rebars corrosion process and the characterization technique are described. The next section shows experiment and simulation results, specifically the MATLAB pipe simulation models, the coating behaviour and performance in NaCl and  $\text{Ca}(\text{OH})_2$  solutions. Finally, in the discussion section the results are described and analysed.



# 1 Background

This chapter presents a general background regarding the use of rebars in reinforced concrete and oil and gas pipelines. Furthermore, the second part of this section is focused on resuming the main corrosion concepts.

## 1.1 Oil and Gas Pipeline

Oil and gas pipeline transport and distribute crude oil, natural gas, chemicals, and petroleum products throughout the U.S. every day. Therefore, the low efficiency of supply means a severe economic impact. There are 299,000 miles of onshore gas transmission pipelines and 171,000 miles of onshore hazardous liquid pipelines with the purpose to connect wells and refineries to the end-users i.e. residential, commercial, industrial and institutional costumers [4]. The pipeline safety aspects during liquid and gas transport should be strictly controlled and respected to reduce the risks of disastrous accidents. The pervasive pipeline network extends through the whole US, in particular in urban and suburban areas, where there is a high demographic density. Releases of a product carried by these pipelines can impact surrounding populations, property, and the environment. Consequently, it may result in injuries and fatalities as well as environmental damage. For this reason, the Pipeline and Hazardous Materials Safety Administration (PHMSA) has been founded as one of ten operating administrations within the U.S. Department of Transportation. This department has the purpose to identify and evaluate safety risks, develop and enforce standards for design, construction, operations, and maintenance of pipelines carrying natural gas or hazardous liquids, educate operators and the public and conduct research on promising technologies. It also investigates the causes of pipeline incidents and it draws up reports about the different pipeline damages. Figures 1.1 and 1.2 are such an example [4].

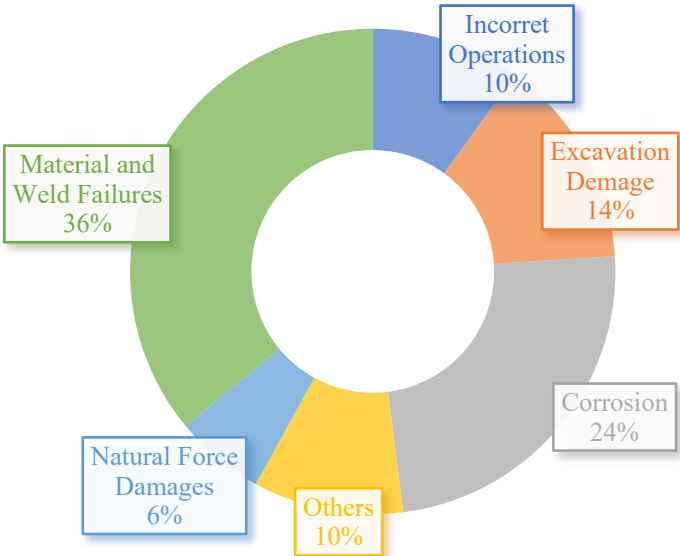
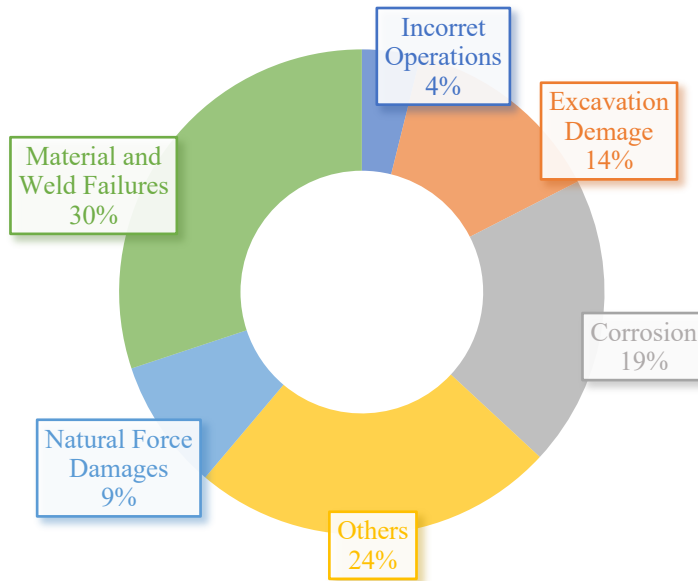


Figure 1.1 Causes of Significant Onshore Hazardous Liquid Pipeline Incidents [4].



**Figure 1.2** Causes of Gas Transmission Pipeline Significant Incidents [4].

As illustrated in the pie chart, corrosion is one of the principles causes of pipeline fracture and it costs billions of dollars to the economy. In other words, corrosion is a big issue.

### 1.1.1 Pipeline Classification

There are over 2.6 million miles of fuel pipelines in the United State that are divided into hazardous liquid and gas pipelines as in Figure 1.3.

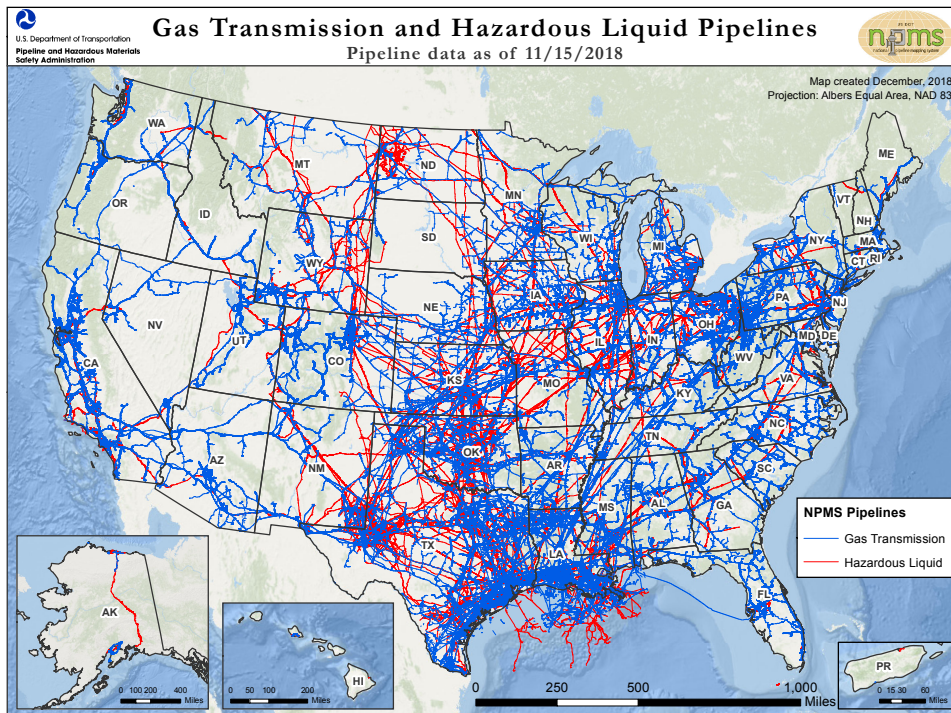


**Figure 1.3** Gas Transmission and Hazardous Liquid Pipelines. [5]

Hazardous liquid pipelines carry crude oil and refined fuels such as gasoline, diesel and jet fuel but they can also carry highly volatile liquids such as butane, ethane, and propane instead the principal constituent carried from gas pipelines is methane. Consequently, the totality of fuel pipelines in the US can be classified based on the carried substance and specific purpose. There are about 200,000 miles of onshore and offshore hazardous liquid pipelines; about 320,000 miles of onshore and offshore gas transmission and gathering pipelines and about 2,170,000 miles of natural gas distribution mains and service pipelines [6]. Therefore, the majority of pipelines miles are dedicated to service distribution. The fuel pipeline transportation system provides gas or refined fuels from the production locations to customers. As illustrated in Figure 1.4, the hazardous liquid and natural gas transportation system is formed by:

- Gathering pipelines transporting gas away from the point of production to another facility for further refinement or to transmission pipelines. Gathering systems typically require a small-diameter pipe that runs over relatively short distances. The branch lateral lines commonly are 0,0508 m to 0,2032 m (2 to 8 in). It should be designed to minimize pressure drop without having to use large-diameter pipe or require mechanical pressure-elevation equipment to move the fluid volume, pumps for liquid and compressors for gas.
- Transmission pipelines are the large lines, typically 0.15-1.20 m in diameter, that move gas long distances around the country, often at high pressures, typically 13-100 atm (200 – 1500 psi).
- Distribution pipelines are a system of mains and service lines that deliver natural gas to individual homes and businesses. They operate at relatively low pressure.
- Production Lines the pipes and equipment, normally near the wellhead, used to produce and prepare the gas for transport.

The pipeline’s path can be onshore or offshore; the first one involves the deposition of the pipeline on the surface ground or buried underground instead the offshore pipelines are extended under the sea level.

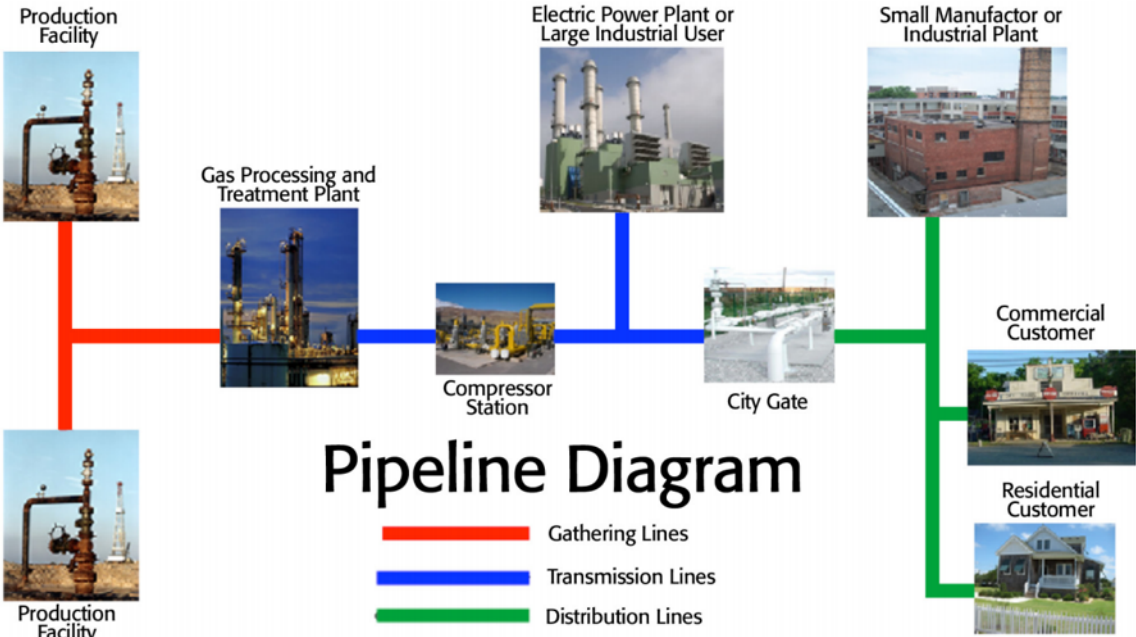


Figure 1.4 Pipeline transportation system from production to consumption [6].

### 1.1.1.1 Offshore Pipeline

The sub-sea pipeline is a pipeline that is laid on the seabed inside a trench. The majority of pipelines are located onshore because they have easier access for operators than submerged ones. The construction of an offshore pipeline considers a large number of factors related to engineering but in several cases also offshore ecology, geo-hazards and environmental. Pipeline construction involves the assembling of a large number of pipe segments to realize the full line and installing the line along the desired path. The specific step of deposition of the line on the seabed is a critical point because the material is subjected to intense mechanical stress. Therefore, several systems are developed to reduce the amount of stress that is concentrated inside the material before it starts work. The most commonly used installation processes are the S-lay system when the seabed is not extremely deep, during the installation the pipeline starts in a horizontal position on the vessel and gradually assumes a characteristic S-shape on the way to the seabed, as shown in Figure 1.5. J-lay system can install pipeline down to 3,350 m deep, the line leaves the J-lay vessel in a vertical position thanks to the presence of a tower, as represented in Figure 1.6. Reel-lay system, in this case, the pipeline is assembled onshore and it is spooled onto a large drum that it is mounted on a sea-going vessel. The vessel travels from the assembled zone to the installation site where the pipeline is unspooled and deposited on the seabed. The advantage of this system is a reduction in time installation. The reel-lay system can only handle lower diameter pipelines – up to about 0,4 m [7].

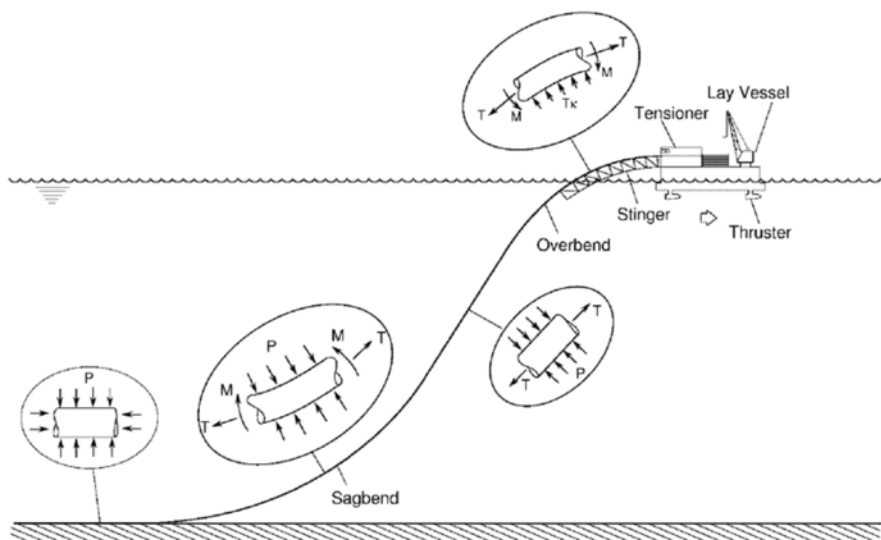


Figure 1.5 S-lay pipeline installation with pipeline loading [7].

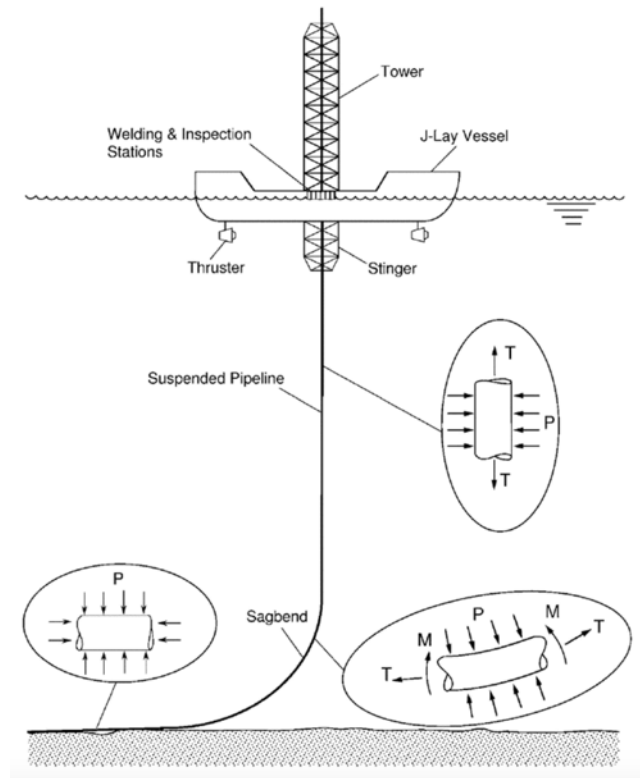
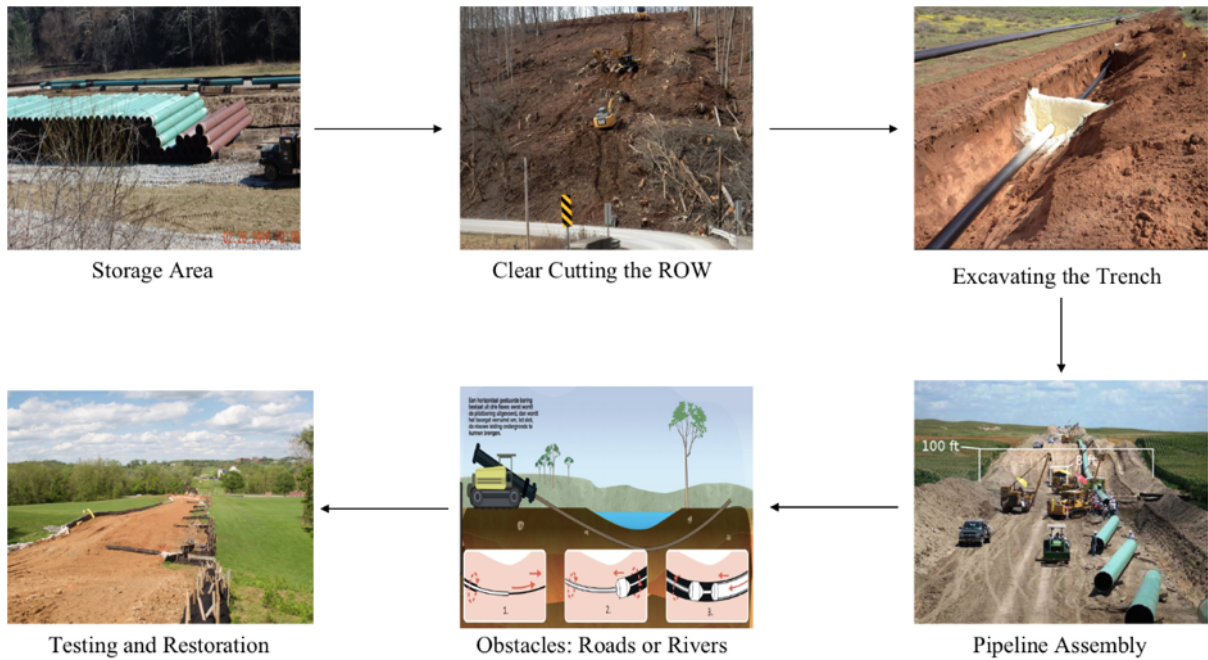


Figure 1.6 J-lay pipeline installation and associated loading [7].

### 1.1.1.2 Onshore Pipeline

Transporting hazardous liquid and gas pipelines have the purpose to connect the production site to the costumers. The pipeline has to be projected to maintain constant supply and reduce the cost of transportation. For this reason, generally, the pipeline networking can be built choosing the shortest route or the straighter one. Unfortunately, the first selected route frequently needs to be changed due to the presence of natural obstacles such as mountains, rivers, and swamps or permitting restrictions. Often the pipeline path is not completely buried but in some regions that could be emerged on the surface ground [8]. The construction of an onshore pipeline starts with the location of the staging area and storage yards. When the equipment is accessible, it follows the cleaning of the concerned areas so large trees are stockpiled or hauled off, while the branches and treetops are placed into piles and burned. After that, the trench is realized and sandbags are placed within the trench to restrict water flow and to support the pipe. At this point, pre-coated segments of pipe, usually 12 m in length, are transported from the storage area to the right-of-way (ROW) and they are laid above ground beside the trench or within the trench on the supporting sandbags. Then, the pipe segments are welded to obtain the final line and the weld joints are coated with epoxy resin to prevent corrosion. Finally, the weld joints are inspected with x-ray to ensure their quality and the connected lengths of pipe can be lowered into the trench. In the presence of roads, highways, streams, rivers or wetlands the pipeline is constructed underneath to avoid the obstacle using the horizontal directional drilling (HDD). In conclusion, the pipe is inspected, the trench is filled in and the pipeline integrity is tested using hydrostatic testing. All these steps are summarized in Figure 1.7.



**Figure 1.7** Representation of onshore pipeline construction. Figures taken from [9] with changes.

### 1.1.2 United State Pipeline Condition

Over 50% of the pipeline network in the United States are built in the 1950s and 1960s due to the huge demand for energy post-World War II. This is illustrated in Figure 1.8. Pipelines are characterized by long term cycle life, therefore, several working pipelines, in this day and age, are outdated, in terms of used materials and construction technology. Hazardous liquid and gas transmission pipelines are made in steel instead gas distribution pipelines are generally realized in cast iron. Furthermore, it should be noticed that in the current generation of gas distribution pipeline there is a tendency to replace cast iron with plastic. Steel is more susceptible to corrosion phenomena, but at the same time, it is more strength to excavation damage than plastics. Cast iron presents a high corrosion resistant but it is sensitive to graphitization phenomena. Moreover, some steel pipelines have not an outside coating because they were built before the legal obligation. Some of the first coatings that were used in those times, showed some problems in terms of corrosion and adhesion [4].

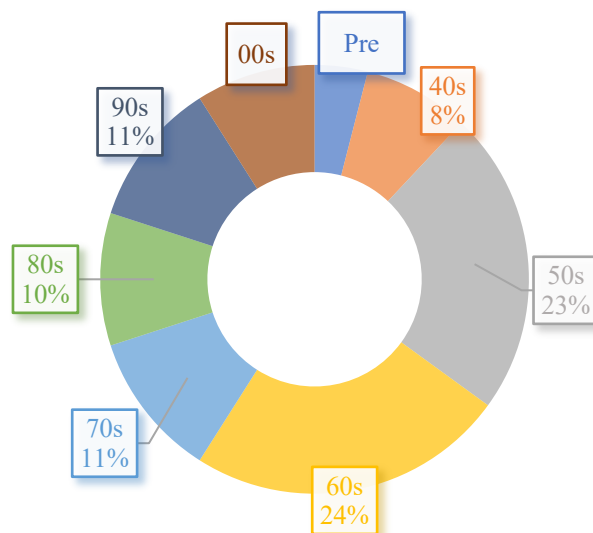


**Figure 1.8** Age Distribution of U.S. Pipeline Infrastructure [6].

### 1.1.3 Flammability limit

Before a fire or explosion can occur, three conditions must be met simultaneously. A fuel, i.e. combustible gas, and oxygen must be in certain proportions along with an ignition source, such as a spark or flame. The ratio of fuel and oxygen that is required varies with each combustible gas or vapor. The minimum concentration of a specific combustible necessary to support its combustion in air is defined as the Lower Explosive Limit (LEL). Below this level, the mixture is too “lean” to burn. The maximum concentration of a gas that will burn in the air is the Upper Explosive Limit (UEL). Above this level, the mixture is too “rich” to burn. The range between the LEL and UEL is known as the flammable range. Table 1.1 shows the LEL and UEL in the percentage of volume concentration for several gases and hazardous liquid measured at room temperature and atmospheric pressure [4]. The operation conditions need to be controlled to reduce the risks of sudden accidents, that could involve not only the destruction of the building but also the damages could cause the death of innocent people.

**Table 1.1** Flammability Characteristics of Combustible Gases expressed in %volume [10].

<i>Gas</i>	<i>LEL</i>	<i>UEL</i>	<i>Flash Point (°C)</i>	<i>Ignition Energy (mJ)</i>	<i>Autoignition Temperature (°C)</i>
<i>Acetone</i>	2.6	13	-17	1.15	485
<i>Acetylene</i>	2.5	100	Flammable gas	0.017	305
<i>Benzene</i>	1.2	7.8	-11	0.2	560
<i>Carbon Disulfide</i>	1	50	-30	0.009	90
<i>Carbon Monoxide</i>	12	75	-191		609
<i>Cyclohexane</i>	1.3	8	-18	0.22	45
<i>Diborane</i>	0.8	88	-90		38
<i>Diesel</i>	0.6	7.5	62		210
<i>Gasoline</i>	1.4	7.6	-40		246
<i>Hydrogen</i>	4	75	Flammable gas	0.0016	500
<i>Kerosene</i>	0.6	5	38		210
<i>Methane</i>	5	15	Flammable gas	0.21	580
<i>Propane</i>	2.1	10	Flammable gas	0.25	480
<i>Toluene</i>	1.2	7	4.4	0.24	480

### 1.1.3.1 Pipeline accidents

Although the pipelines state is controlled using modern technology to prevent dramatic accidents, accidents still occur. Some of the most deleterious incidents are reported below.

- *July 30, 2004, Ghislenghien, Belgium.* The accident involved two gas pipelines buried about 1.10 m deep. At 9:00 am the explosion occurred after a loud hissing and an intense ground vibration. An enormous gas cloud was formed, the ignition occurred and produced "fireballs" that subsequently transformed into a long flare whose height was estimated at 150-200 m. The workers closed the valves to isolate the first line but due to the vibrations, the operations were complicated, so the vibrations of the first line were propagated on the ground and it caused the second leak in the second line, that was around 7 m distance. The explosion created a crater 10 m in diameter and 4 m deep. The final victim tally was 24 dead and 132 injured. The amount of accident cost was around 100 million euros. The expert's investigations established that the damage was caused to "external aggression" due to some earthworks held in the site [11, 12]. Some pictures of the incident are shown in Figure 1.9.



Figure 1.9 Ghislenghien gas pipeline explosion [11, 12].

- *November 9, 2010, San Bruno, California.* At 6:11 pm a steel gas pipeline exploded in a residential neighborhood of San Francisco. The explosion and resulting fire leveled 35 houses and damaged many more and killed 8 people. The explosion excavated an asymmetric crater 51 m long, 7.9 m wide and 12 m deep, as shown in Figure 1.10. The flames remained active until 11:40 on the following day and eyewitnesses reported that the initial blast "had a wall of fire more than 300 m high"[13].



Figure 1.10 San Bruno explosion of gas pipeline. Figures taken from "San Bruno Explosion: Photos Of The Fire's Aftermath Paint A Bigger Picture", Huffingtonpost.com.

- *September 19, 2018, Merrimack Valley, Massachusetts.* An over-pressure inside the pipeline caused a series of explosions and fires in three close towns such as Lawrence, Andover, and North Andover. This pipe generally worked to pressure around 0.34 atm but this day the operators measured the pressure of 5 atm. Immediately, 30,000 people were forced to evacuate their homes. In the three towns were tally between 40 and 80 fires so a cloud of smoke covered all-region [15]. Some pictures of the disaster and the map of multiple explosions are shown in Figure 1.11.

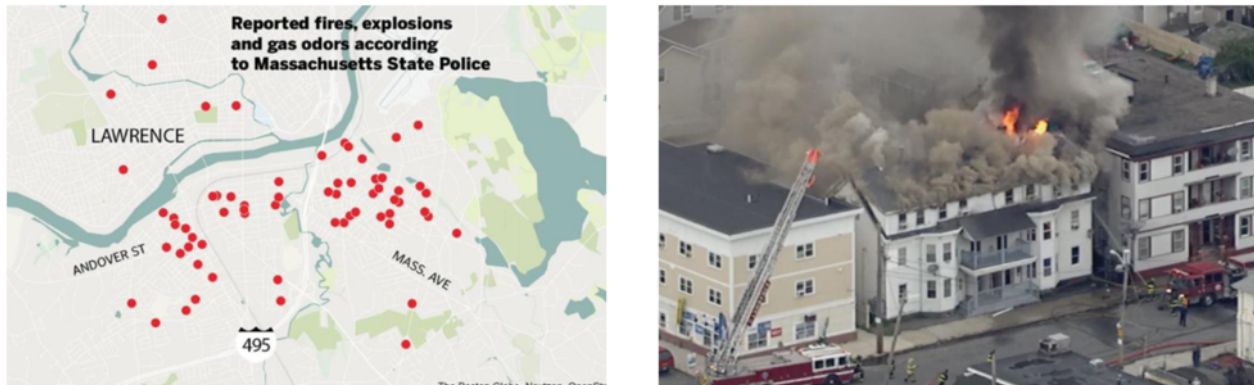


**Figure 1.11** Picture of a building in Merrimack Valley and multiple explosions map. Figures taken from “Dozens of explosions, fires after apparent gas issue in Merrimack Valley”, BostonCarmensUnion.com and “Map: Location of the fires, explosions, gas odors in Lawrence area”, BostonGlobe.com.

## 1.2 Bridges

Bridges are civil engineering works that allow to cross a natural barrier such as water or valley. In particular, the bridges, that running in this days in US, are built at the end of World War II in order to generate an extensive network of roadways facilities that allowed the people and good movement, promoted the growth of US economy, gave access to national and international markets and supported national defence ensuring rapid army deployment [16]. The bridge’s construction can be considered a material of study that has been to go on for centuries, starting from Roman period. Over the years, thanks to technological innovation news construction techniques are developed so in this day and age it is possible to rely on several types of bridges depending on the case. For instance, as shown in Figure 1.12, there may be different types of bridges: the beam bridge, the Truss bridge, the cantilever bridge, the arch bridge, the tied arch bridge, the suspension bridge, or the cable-stayed bridge. The most diffused materials for bridges building are structural steel and reinforced concrete but this thesis works is focused on study bridges with rebar as reinforcement in concrete.

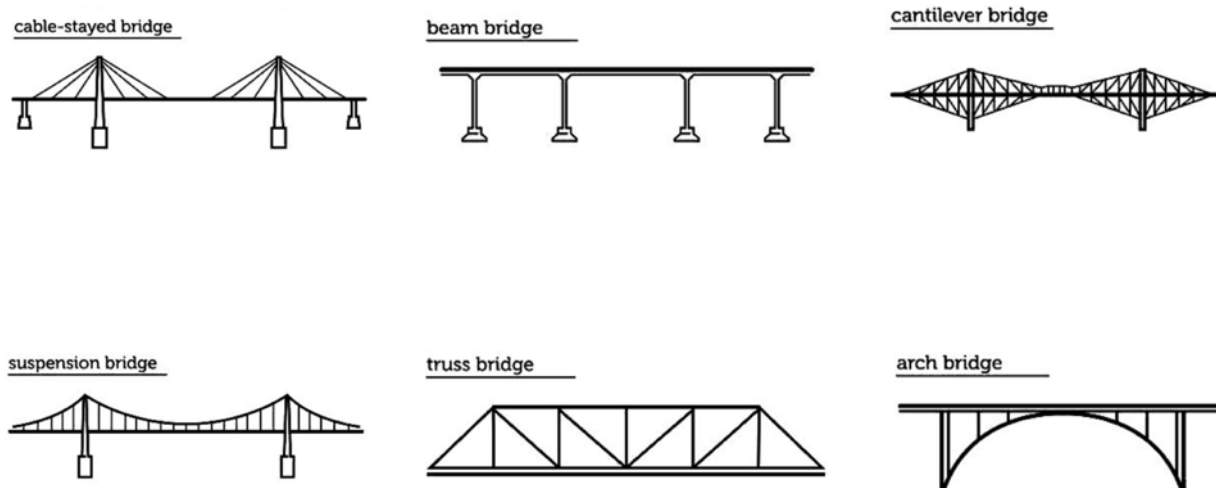


**Figure 1.12** Types of Bridges. Figures taken from “Different Types of Bridges”, Engineeringdiscoveries.com.

### 1.2.1 Reinforced Concrete

Reinforced concrete is one of the most diffused materials used in this day and age to realize residential, industrial and civil engineering works, i.e. bridges, tunnels, dams, highways, and railways. The reinforced concrete is a composite material consisted of two different elements:

*Concrete.* This is a composite material constituted mainly of water, aggregate, and cement. The aggregates typically have different dimensions; the coarse ones that can act as a filler and the fine ones that fill up the void between the paste and the coarse aggregates. Regarding the mixture between water and cement, this acts as a binder.

*Reinforcement.* The concrete can be reinforced with several types of material depending on working conditions such as steel rebars or fibers, glass fibers, and polymer fibers. In recent years, as a result of the environmental impact, sustainable materials are introduced as a reinforcement material in concrete, i.e. grasses, hemp, bamboo and wood [17]. Generally, steel rebars, with a maximum diameter of 3 cm, are the most commonly used, they are properly shaped and interlinked to form the “cage”.

### 1.2.2 Advantages of Reinforced Concrete

The synergy between steel and concrete gives to reinforced concrete a range of proprieties that make it the most used material in the civil sector. The great success can be understood by the following numerous advantages shown below.

- Reinforced concrete has great resistance to fire and water. It is considered the best structural material in water presence and in case of fire only the external surface is damaged while the inner steel is still intact.
- Reinforced concrete structure is very rigid so it is commonly used in the construction of the railway bridge [19].
- It does not require expensive maintenance operations.

- It has a long service life compared with other materials. It does not reduce their load-bearing capacity over the years thanks to the solidification reaction that goes on for a long time.
- It is usually the cheapest solution for footings, floor slabs, basement walls, piers, and similar applications.
- It is possible to make structures with different sizes and shape with total liberty forms.
- It does not require a high grade of skilled labor compared with other materials such as structural steel.
- High availability and economy of reinforced concrete elementary components.

### 1.2.3 Disadvantages of Reinforced Concrete as a Structural Material

However, as all materials also reinforced concrete has its drawbacks.

- Concrete has a very low tensile strength, requiring the use of tensile reinforcing.
- Form is required to hold a concrete structure until it is sufficiently hardened.
- The reinforced concrete structures are heavy due to the high specific gravity of the material.
- Poor thermal and sound insulation. The concrete has a weak attitude to stop thermal fluxes and acoustic waves.
- Reinforced concrete is a porous material so it suffers from the capillary rise. Consequentially, if the structure is based on groundwater or high moisture content ground, a waterproof concrete is required.
- The concrete properties can vary drastically changing the proportion and the ratio of the mixture.
- At the end of the life cycle, the reinforced concrete is difficult to dispose or recycle.
- Last but not least, concrete suffers from shrinkage and creep phenomena.

### 1.2.4 Properties of Reinforced Concrete

The concrete shows an excellent compressive strength but rather the tensile strength resistance is weak. Steel rebars, that have great resistance to tensile stresses, are introduced in the concrete mixture to solve the concrete critical point. This new composite material is called reinforced concrete. Thanks to the excellent adhesion between steel and concrete tensile stresses can be transferred from the concrete to the steel while the compressive stresses are supported by the concrete itself. This is illustrated in Figures 1.13 and 1.14, where no-reinforced and reinforced beam are compared while bending stress acted. In a non-reinforced beam a wide and deep crack starting from the tensile region can be observed instead in reinforced beam multiple cracks propagate only in the concrete matrix but with small size [19].



Figure 1.13 No-reinforced beam tests with small load [19].

The Coefficient of Thermal Expansion (CTE) is close enough between steel and concrete, which provides excellent compatibility between the materials when they are subjected to stresses or temperature changes. In Table 1.2 are reported the respective CTE values. The excellent interfacial bond between these two materials is the result of chemical adhesion.

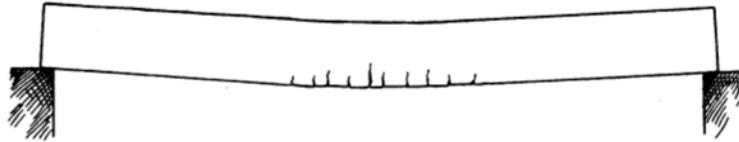
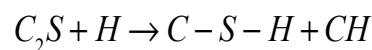
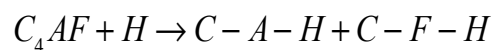
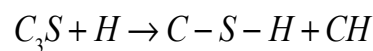
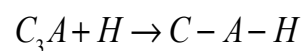


**Figure 1.14** Reinforced beam with bars [19].

**Table 1.2** Coefficient of Thermal Expansion of Steel and Concrete [20, 21].

<i>Material</i>	<i>CTE</i> $\left[\frac{1}{K}\right]$
<i>Steel</i>	$11 - 12.5 \cdot 10^{-6}$
<i>Concrete</i>	$12 - 13 \cdot 10^{-6}$

Furthermore, to enhance the interfacial adhesion the rebars can be twisted or corrugated to increase the friction and avoid possible slipping. The rebars connections also can change the stresses distribution in the material indeed many parameters and simulations are used to determine the best structure of the “cage”. This aspect should not be underestimated because the changing of rebar position can modify the material’s response and the structural integrity [19]. Reinforcing bars are subjected to corrosion, but the concrete surrounding them provides excellent protection. Moreover, a sufficiently workable concrete mixture is essential to surround the reinforcing bars and fill the form. To achieve this desired workability, more water is used compared to the stoichiometric volume, required from the hydration reactions. The cement hydration reactions are based on a series of complex reactions that are not yet completely understood. Using the cement chemistry notation, the main possible reactions are presented below.



Where the chemical compounds are:

- $C_2S$  is dicalcium silicate ( $2CaO \cdot SiO_2$ ).
- $C_3S$  is tricalcium silicate ( $3CaO \cdot SiO_2$ ).
- $C_3A$  is tricalcium aluminate ( $3CaO \cdot Al_2O_3$ ).
- $C_4AF$  is tetracalcium aluminate ferrite ( $4CaO \cdot Al_2O_3 \cdot Fe_2O_3$ ).

- $CH$  is calcium hydroxide ( $Ca(OH)_2$ ).
- $H$  is water ( $H_2O$ ).
- $C - S - H$  is hydrated silicate of calcium.
- $C - A - H$  is hydrated aluminate of calcium.
- $C - F - H$  is hydrated ferrite of calcium.

In short, the aluminate becomes hydrated aluminates of calcium instead the silicate becomes hydrated silicates of calcium, that have the texture of a rigid gel. The concrete binding capacity is due to the formation of a hydrated silicate of calcium indeed an excess of hydrated aluminate of calcium reduces the concrete workability and increase the curing time [22]. The extra mixing water does not react, remains inside the concrete and flows on the surface concrete where it evaporates. As a result, the concrete shrinks and cracks. The cracks can expose the reinforcement rebar to the atmosphere or chemical, such as chloride, and the corrosion process can be promoted. The water evaporation requires time thereby shrinkage continues for many years, even if generally the 90 % of shrinkage occurs in the first year. Furthermore, shrinkage depends also on the weather conditions, in windy regions the shrinkage will be greater instead in humid ones it is lower. The aggregates nature also influences the curing, using low-adsorptive aggregated, like granite or limestone, the water evaporation is promoted instead when adsorptive slates and sandstone are used the shrinkage may be reduced in the first moment but structure consolidation requires much time [18]. Under compressive loads, after an initial elastic deformation, concrete continues to deform plastically. This is phenomenon is well-known as creep and it depends strongly on the amount of stress. Other parameters influence creep inside concrete such as temperature and humidity. Creep is almost twice as large at 50 % humidity than at 100 % humidity [18].

### 1.2.5 Manufacturing Techniques

The reinforced concrete can be realized in the manufactory as prefabricated modules, that will be assembled in the building site, such as columns, slabs or panels, or realized directly on-site, in the construction place, the concrete is poured in the form, in which the reinforcement is previously disposed. This is illustrated in Figure 1.15 and 1.16. Usually the prefabricated modules have greater accuracy dimension than the on-site reinforced concrete but unlike during the assembly they can show junctions problems. Moreover, the prefabricated modules are commonly used when the weather condition does not influence the concrete curing [23].



**Figure 1.15** Prefabricated module. Figure taken from “TT Beam”, Viprocosa.com.



**Figure 1.16** On site pouring concrete. Figure taken from “Calcestruzzo Armato”, Teknoring.com.

### 1.2.6 United States Bridges Condition

In US there are approximately 614,387 bridges distributed in the territory. The majority are built between 50s and 60s so they are in service for more than fifty years. This is illustrated in Figure 1.17, where it is also observable that the majority of US bridge have more than twenty years life, thereby, as a result in the near future the amount of bridges that will come at the end of their life, it will increase dramatically. For this reason, the US Department of Transportation has already provided to check the status of US bridges in order to maintain, rehabilitate and replace the damaged ones [24]. An idea of the actual bridges situation in US is reported in Figure 1.18. In recent years, there is more government sensitivity regarding this problem, many investments are done to fixed bridges, even if the funds are insufficient then more money are required. In Table 1.3 are shown the top and the bottom US states that have deficient bridges. The US Department of Transportation is not confined to restore the existing bridges but also supports the research in news materials and technologies in order to develop materials with longer life, higher strengths and excellent corrosion resistance [23].

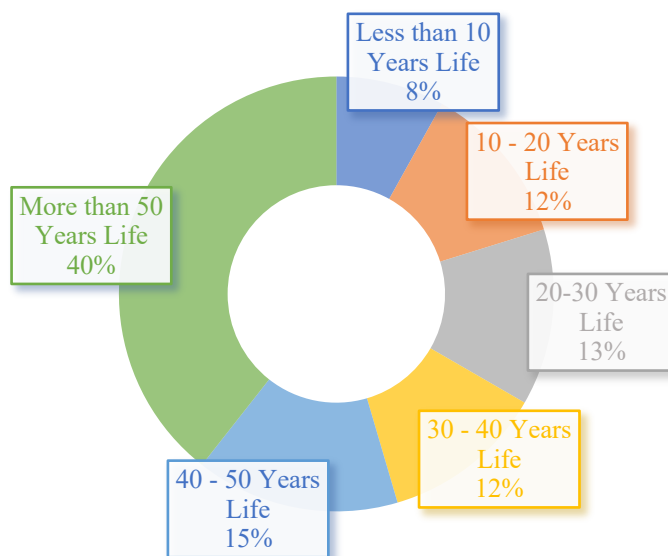


**Figure 1.17** America’s Bridges by Age [23].

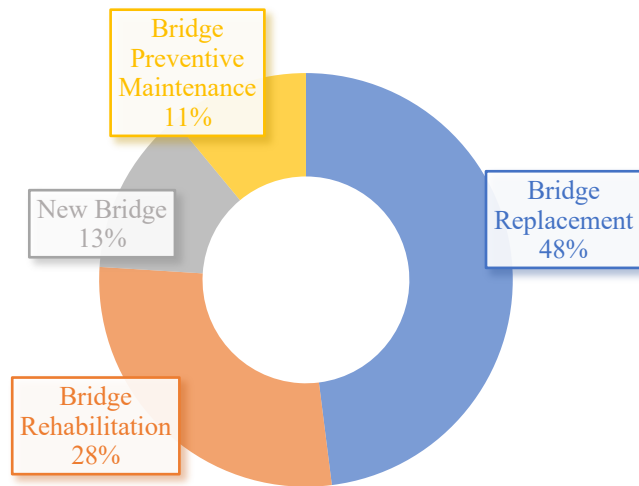
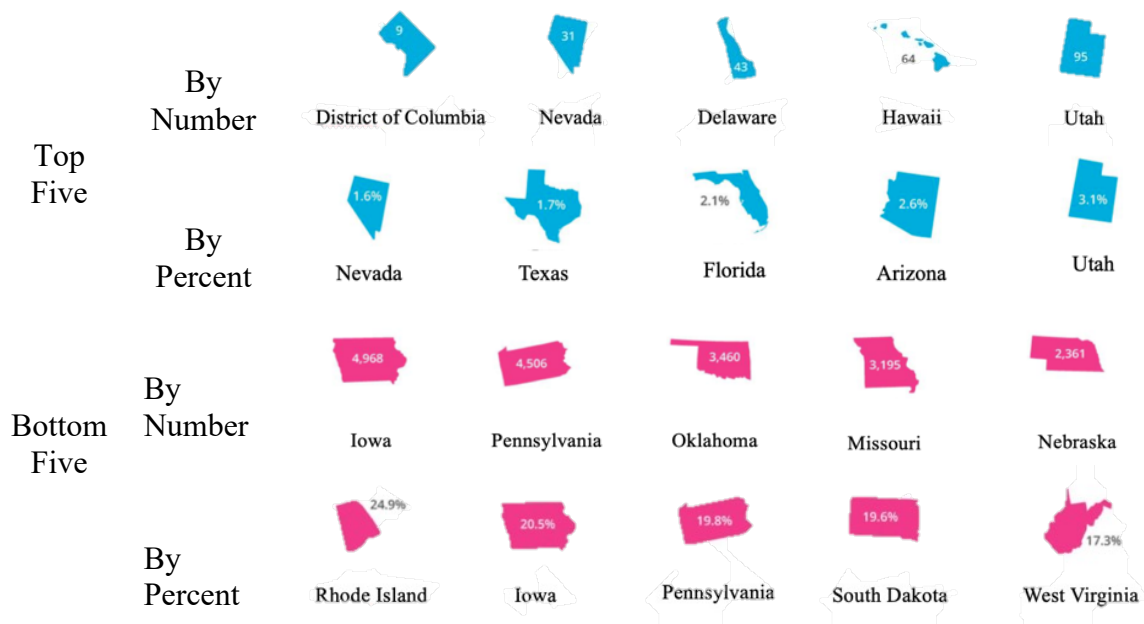


Figure 1.18 Condition of America's Bridges in 2015 [24].

Table 1.3 Structurally Deficient Bridges: Top and Bottom Five States by Number and Percent [23]



### 1.2.6.1 Bridges Accidents

Although, the bridges state is controlled using modern technology, as sensors, to prevent dramatic accidents, collapses still occurs. Some of the most deleterious incidents are reported below.

- *October 21, 1994, Seongsu Bridge, Seoul, South Korea.* At 7:40 the central section of the bridge, that was 48 m in length, collapsed during service, as shown in Figure 1.19. There were 32 people died and 17 injured. The main cause of the failure was due to improper welding of the steel trusses of the suspension structure beneath the concrete slab roadway [25].



**Figure 1.19** Collapse of Seongsu Bridge, Seoul, South Korea [25].

- *August 1, 2007, I-35W Mississippi River Bridge, US.* At 18:05 the eight-line of the I-35W highway bridge over the Mississippi River in Minneapolis, Minnesota had a catastrophic failure in the main span of the deck truss, that collapsed immediately, shown in Figure 1.20. The 111 vehicles that were on the bridge, collapsed with it as a result 13 died and 145 were injured [24].

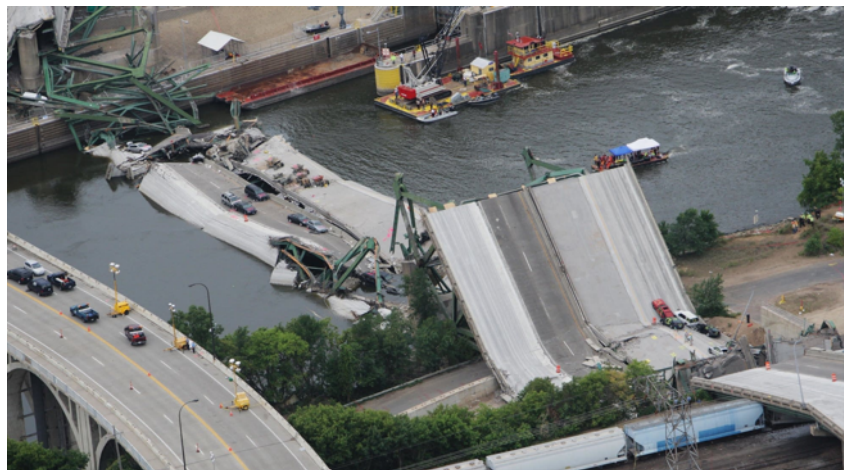


**Figure 1.20** Collapse of Mississippi River Bridge, USA [24].

- *August 28, 2018, Morandi Bridge, Italy.* At 11:36 the pillar 9 of the bridge collapsed killing 43 people, illustrated in Figure 1.21. The research, that is been done to determine the causes of breaking, have identified corrosion on the embedded steel even if the investigations are still ongoing.



**Figure 1.21** Collapse of Morandi Bridge, Genova, Italy. Figure taken from “Immense tragedy: 30 dead in Italy motorway bridge collapse”, Eglenews.com.

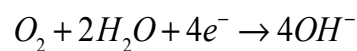
### 1.3 Corrosion

Corrosion is defined as the interaction between a material and the environment that degrades the material, changes his properties and compromises his functionality. Metal corrosion is a spontaneous process in which the Gibbs free energy is less than zero ( $\Delta G < 0$ ). Corrosion phenomena are due to electrochemical reactions and they allow the metals re-oxidation, for this reason usually is known as anti-metallurgy. These reactions involve the electric transfer of metal electrons across an electrolytic conducting solution. The total reaction can be divided into two partial reactions:

- The metal dissolution, known as oxidation or anodic reaction, an example is the iron oxidation.



- Oxygen reduction, known as a cathodic reaction.



These reactions occur on the metal surface with uniform distribution or as a localized attack. To promote corrosion must be satisfied some requirements, shown in Figure 1.22.

- Conducted metal for the anodic reaction.
- Electrolyte, such as a thin moisture film on the metal surface, to allow the electrons transfer.
- Oxygen for the cathodic reaction.

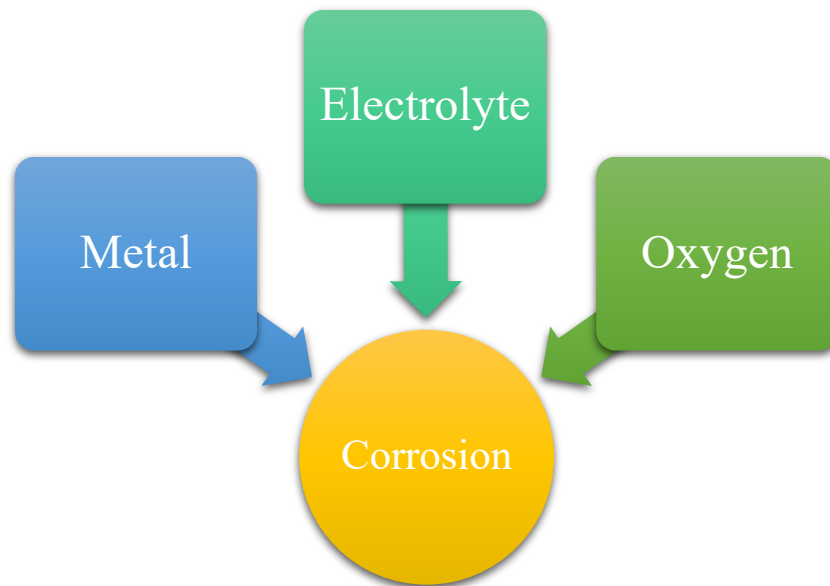


**Figure 1.22** Corrosion Requirements.

The corrosive mechanism of iron when a water drop is on his surface is reported in Figure 1.23. At the interface, the anodic and cathodic reactions occur, the metal is oxidized instead the oxygen is reduced and red rust appears on the metal surface. This mechanism is promoted also with other metals such as aluminum and zinc. Thanks to continuous studies nowadays it is possible to control and prevent corrosion to stop or delay the partial reactions.

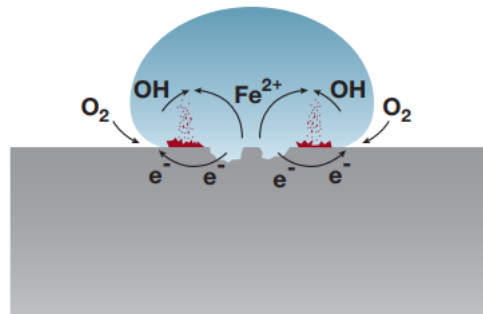


**Figure 1.23** Iron Corrosion under a water drop [26].

## 1.4 Pipeline Corrosion

One of the main factors that deteriorate pipeline is corrosion. In particular, when the metallic surface comes in contact with an electrolyte solution; the electrochemical process occurs and the steel pipeline deterioration starts. Corrosion could be due to external factors such as the natural interaction between the exterior pipe surface such as soil, air, and water surrounding; or for internal factors owing to environmental conditions inside the pipeline [28]. Different corrosion mechanisms can be generated by several metal-environment-stress coupling, in particular, the most relevant environmental factors are [2]:

- Soil chemistry (salts, acids, and alkalis), electrical resistance and moisture.
- Temperature range and peak levels.
- Humidity, condensation and splash exposure.
- Exposure to saltwater or natural water in case of partial, complete or fluctuating.
- Reactivity of the transported liquid or gas and the hazard associated with leaks.
- Proximity to cathodic or anodic protection, high-voltage lines, grounding or railway stations could induce the stray current.
- Exposure to UV radiation, sunlight, and chemicals.
- Acid rains, smog from industry and sewage.
- Presence of micro-organism.

It is not possible to define the most frequent type of corrosion in pipeline because too many parameters are involved. Generally, to avoid corrosion in the pipeline system several types of protection can be used, such as cathodic protection, coating or inhibitors.

### 1.4.1 Pipeline Protection

Over time several methods of corrosion protection are developed and applied on pipelines to mitigate the damages.

#### 1.4.1.1 Cathodic Protection (CP)

The cathodic protection is an electrochemical technique that allows to control and prevent from corrosion, buried and marine structures, heat exchanger's internal surfaces, chemical equipment and to reinforce concrete structures from chloride attack. There are two possible operating strategies:

- *Impressed Current.* The pipe metal's potential can be moved to negative values by impressing a voltage through an external power source. Impressed current is applied in the opposite direction to nullify the corrosion current and convert the corroding metal from anode to cathode. The negative terminal of the power source is connected to the structure to be protected. The other terminal is joined to an inert anode, often graphite, which is buried in the soil, therefore, the high-conductivity material provides good electrical contact between the anode and surrounding soil [2, 29]. An example of this device is shown in Figure 1.24.

Theoretically, the minimum needed current to cathodically protect a metallic system is calculated from the polarization curves of the anode and cathode reactions. It is a consolidated knowledge that the coupling of steel coating and cathodic protection reduces the current needed for cathodic protection. The presence of the coating decreases the oxygen diffusion rate so less current is required to polarize the metal cathodically. The simultaneous use of coating and impression current reduces the amount cost of electric energy required to protect the structure from corrosion.

- *Sacrificial Anode.* The sacrificial anode is a material block made with a less noble metal than the pipe metal, electrically connected that will corrode preferably compared to the pipeline. The anode area needs to be suitably controlled to avoid the rapid corrosion of

the anode. Generally, the anode design is carefully chosen to substitute the part annually.

Sacrificial anodes can be made in aluminium, zinc and magnesium alloy but they often provide inadequate protection in large structures, i.e. pipelines, so in this case, CP with power source shall be considered the best option [2].

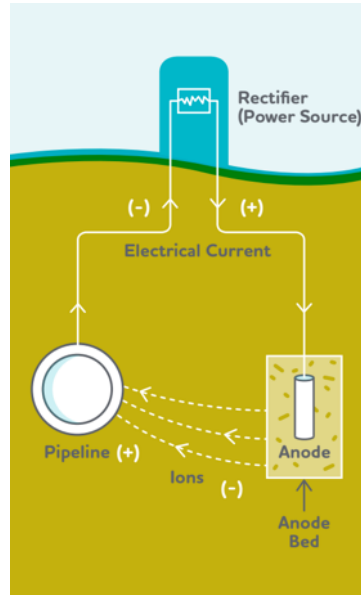


Figure 1.24 Representation of Impressed Current Cathodic Protection [30].

#### 1.4.1.2 Pipeline Coatings

One of the most effective strategies to reduce corrosion risks on pipeline involves cover the substrate with specific coatings to avoid the formation of redox reactions. Today pipe coating is standard practice and provides the following benefits:

- *Improved Gas Flow.* The coated pipeline presents a smoother surface that improves the flow capacity of the line than uncoated ones.
- *Faster Inspection and Commissioning.* Coated pipeline dries faster so inspection and commissioning are easier than uncoated ones.
- *Decreased Cost of Energy.* Pipelines that are coated internally allow to cut the cost of compression and pumping to save money and increase financial payback in 3-5 years.

The pipeline can be coated both externally and internally, therefore strict regulations have been implemented during the last 30 years. The application of internal coatings is not pervasive in the oil and gas pipeline because the operators prefer to treat oil and gas flows using dewatering treatments or adding corrosion inhibitors [2]. Where internal coatings can be used; epoxy and cement are the most diffused at this time as it is reported by PHMSA [28]. Firstly, the coating must be selected to be chemically compatible with the metal substrate. Secondly, to increase adhesion, the metal surface needs to be carefully prepared before coating deposition. To enhance the effectiveness and durability of the final coated component, the parts must be cleaned before the coating deposition. The principal steps in order involve:

1. Alkaline cleanings to kill biological contaminants.
2. Water rinsing.
3. Zinc phosphate application.
4. Second rinsing.
5. Chromate sealer application.

On the markets are sold a large choice of several types of coatings, it is extremely important to evaluate the specific condition in which coating will work to make the best choice. The factors that have been generally taken into consideration are:

- Mechanical properties of the coating.
- Susceptibility to damages, the presence of particles inside the pipe promotes abrasive phenomena during pipe handling for installation and repair.
- Soil chemistry.
- for in-situ joint coating.
- Pipeline operating conditions, such as flow velocity, pressure changes, temperature, and viscosity.
- Compatibility with cathodic protection.

Oil and gas pipelines coatings can be divided into two separate categories:

- *External Coatings.* Oil and gas pipelines run above ground, underground or immersed in fresh or saltwater, so coatings need to be engineered, to provide a proper resistance in these environmental conditions. Furthermore, external coatings must protect the pipe from wastewater, chemicals, local bacteria, and flora, which promote microbiological corrosion. Often pipeline paths across whole states with different climate conditions, that could affect change in pipeline protection levels from corrosion. Coal tar enamel coatings, fusion-bonded epoxy (FBE) coatings, polyolefin coatings, polyurethane coatings are the most diffused external coatings used at this time, even if multilayer coatings are been used recently because they provide more protection.
- *Internal Coatings.* These coatings are been developed to reduce the aggressive attacks of fluids on pipeline internal surfaces. The main purpose of corrosion is due to dissolved gases, such as oxygen, carbon dioxide, hydrogen sulfides, sulfur dioxide or chlorides. Often solid particles can be dispersed in the fluid thereby they could promote erosion effects on pipeline's walls, such as carbonates, sulfates, silica or dirt particles. For this reason, news research is begun in the last decade to study news materials that can show better corrosion resistance.

#### **1.4.1.3 Liquid Epoxy and Internal Fusion Bonded Epoxy (FBE)**

Both techniques have the purpose to cover the pipe's inner wall with a thin film of epoxy resin. Firstly, FBE is an epoxy-based powder coating based on a thermoset polymer that curing between 180 °C and 250 °C. The pipe is pre-treated and preheated to remove dirt and moisture after that epoxy powders are sprayed using an electrostatic gun on the internal surface, then the pipeline is heated again around curing temperature to melt the powder and stimulate chemical cross-linking reaction [30]. Secondly, liquid epoxy coating is a two-part system 100% solid applicable by cartridge, brush, roller or spraying on the pipeline internal surface, in this case, curing occurs above room temperature so a heating step is not required. The final FBE coating should have thickness from 60 to 100 µm instead of liquid epoxy coating is suitable a thickness between 625 and 1500 µm [31]. The pre-treatment step has a crucial role to obtain a strong long-term adhesion of the coatings on the pipeline surface. Both coatings show excellent

chemical resistance to chloride and oxygen, the reductive impact of corrosion fatigue and cavitation, highly compatible with cathodic protection and better dimensional stability due to minimal hysteresis. On the other hand, these coatings are easily damaged by mechanical impacts, they are also relatively expensive owing to the high cost of materials, heating and work requirement, in addition the maximum exposed temperature is above 140 °C, so the life expectancy is 10 - 12 years. One of the most important properties of FBE is associated with failure that is non-shielding to CP if disbondments occurs and water penetrates. Neither external corrosion nor SCC has been a problem under FBE coatings since CP can effectively protect the pipeline under any disbondments.

**1.4.1.4 Monitoring Techniques**

Comparing data obtained by the US Department of Transportation from 1998 to 2017, the number of pipeline incidents due to internal corrosion was approximately 12%, greater than incidents due to external corrosion estimated in the same period [28]. These results show that external corrosion damages are easier sometimes to identify with a visual inspection than internal failure. For this reason, in-line inspection monitoring techniques are extremely diffused in the last years to detect and monitor pipelines network from internal defects. The in-line inspection involves the use of "smart PIG" tool runs that travel along the inside of the pipeline using calipers or scanning technology similar to Magnetic Resonance Imaging (MRI) or ultrasound to measure a pipeline's wall thickness. In Figure 1.25 an example of PIG is reported. Anyway, the total liquids pipeline incidents are decreased from 1999 to 2015 after the usage of these tools, as confirmed in Figure 1.26 [32].

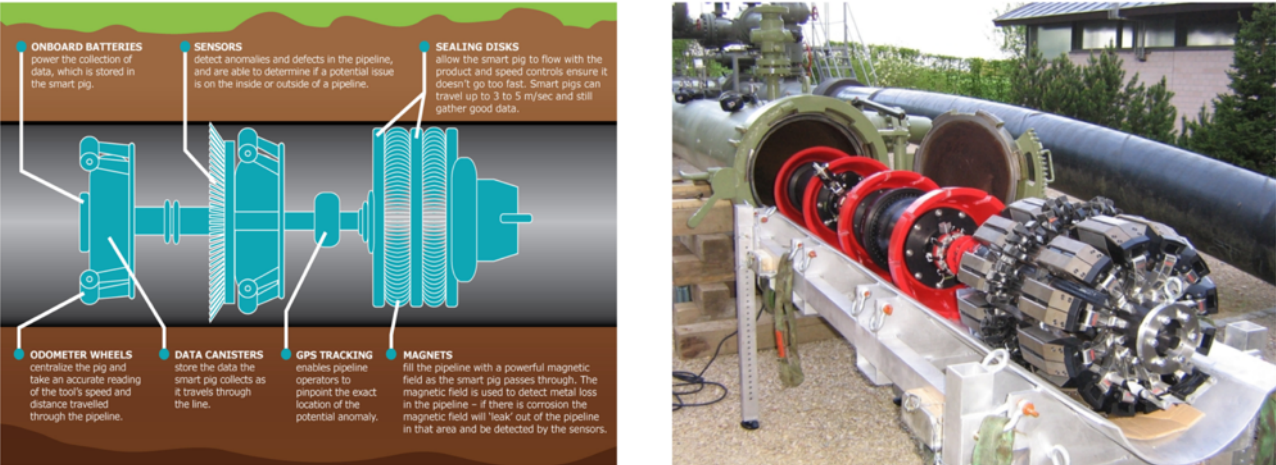


**Figure 1.25** “Smart PIG”. Figures taken from “Inside the smart pig – detecting potential pipeline problems before they happen”, Canadianpipelineassociation.com and “How to prevent leakage or environmental damage”, Iecetech.com.

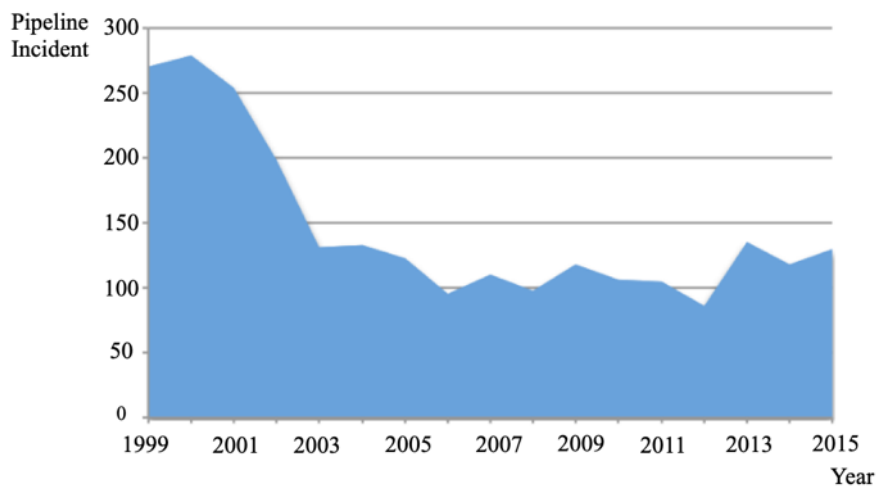


Figure 1.26 Total Liquids Pipeline Incidents from 1999 to 2015 [32].

## 1.5 Corrosion in Reinforced Concrete Bridges

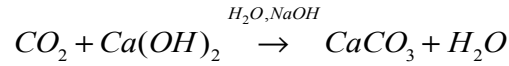
Until the 70s it was believed that reinforced concrete was an intrinsically durable material able to withstand a common aggressive environment building without any particular care. Nevertheless, starting from the first decade of the 1900s, the first damage in reinforced concrete was identified and studied, starting to the degradation of a large packing house outside New York and a harbor in Southampton, United Kingdom [33]. At that times it was not understood the destructive effect of chloride in reinforced concrete structures. Anyway, it will be only in response to the continuous damages of these structures that in 1957 the first reinforced concrete structure was monitoring. Seven-mile-long of a causeway in California, US, was studied to have an electrochemical corrosion map that showed the corroded areas – a routine technique used today by transport authorities around the world for condition monitoring [33]. In these days and age, there is more sensitivity regarding the damages of reinforced concrete works and their prevention. This is due to the increasing of failures, the high risks for people’s safety and the expensive cost of maintenance and restoration [34]. This thesis work is focused on evaluating the main corrosion processes and protective technique that affect bridges.

### 1.5.1 Degradation Mechanism of Reinforced Concrete

Concrete can be subjected to several different forms of degradation, physic, such as freeze-thaw cycles or fire; mechanical, as abrasion, erosion, explosion or shock; chemical as acid, sulfates, sulfides, seawater or alkaline aggregates; biological, as fouling and structural as overload, settling, cyclical stresses. This classification is only theoretical because practically these processes act synergically. When the concrete is reinforced with steel rebars other corrosion degradation processes can occur. Figure 1.27 shows in a schematic way, the connection between concrete degradation and rebars corrosion.



- *Carbonatation.* The alkalinity of concrete can be neutralized by carbon dioxide, coming from the external environment. There is a gradually pH decreasing, at  $\text{pH} < 9$  the passive layer is loss and the corrosion reaction can occur. The carbonatation reaction is schematically shown below.



The carbonatation does not induce damages in the concrete; it reduces, in fact, the porosity and improves the mechanical properties. On the contrary, there are important consequences on reinforcements, that are in contact with a concrete solution with  $\text{pH} < 9$  so corrosion can occur. The tendency of carbonation penetration is presented in Equation (1.1) and it depends directly on the time.

$$s = K \cdot t^{\frac{1}{n}} \quad (1.1)$$

Where  $s$  is the thickness of the carbonation layer,  $t$  is the time,  $n$  depends on the concrete porosity; it assumes value 2 for porous concrete and greater 2 for compact ones. The coefficient  $K$  is related to the carbonation rate, it depends on environmental factors, such as temperature, humidity, carbon dioxide content, but also the alkalinity and porosity of concrete [34].

- *Chloride.* When concrete is in contact with an environment rich of chloride, these ions can penetrate inside the concrete and reach the steel rebars, but as long as the chloride content does not exceed a threshold value (around 0,4 – 1 % of concrete weight content) the protective layer cannot break locally. The chloride can come from the natural environment or through additives that are added to the mixture, for example, calcium chloride ( $\text{CaCl}_2$ ) was commonly used in the past as an accelerant additive but forbidden currently. The required time to chloride attack depends directly on the chloride content on the external surface, the characteristics of the concrete matrix and the thickness of cover concrete. The content curves that describe the penetration of chloride in function of time can be get using Fick's second law for non-stationary diffusive processes, reported in Equation (1.2).

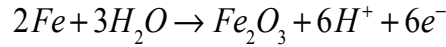
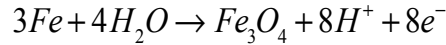
$$\frac{\partial C}{\partial t} = -D_{ce} \frac{\partial^2 C}{\partial x^2} \quad (1.2)$$

$C$  is the total chloride content at time  $t$  and distance  $x$  from the concrete surface,  $D_{ce}$  is the effective chloride diffusion content [34].

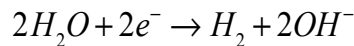
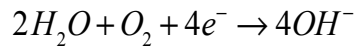
- *Dispersed Current.* Structures, that are crossed by an electric field, are subjected to interference between the field and the steel reinforcement. As a result, the passive film on the steel surface can be penetrated in the areas where the current touch the reinforcement.

The possible anodic reactions in steel embedded concrete are based on concrete pH and the presence of aggressive ions. On the other hand, cathodic reactions depend on the availability of  $\text{O}_2$  and the pH near the steel surface. These reactions are shown below [35].

### Anodic Reactions



### Cathodic Reactions



Furthermore, to be clear, a schematic image of the corrosion mechanism in rebar is shown in Figure 1.29. The corrosion processes commonly lead to the appearance of rust spots on the concrete external surface or spalling phenomena. The corrosion products occupy a greater volume than the steel itself and this induces internal expansion and stresses. The volume of corrosion products depends on the level of hydration of oxides, this is directly related to steel composition, in fact, they can have a volume double or six times higher than iron. The main types of iron hydrates with their specific volume are reported in Figure 1.30.

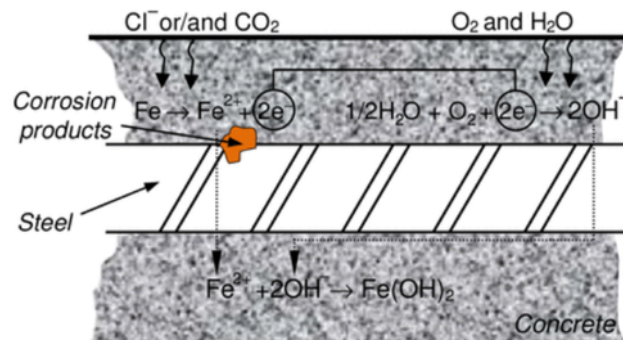


Figure 1.29 Illustration of Corrosion in Reinforced Concrete [35].

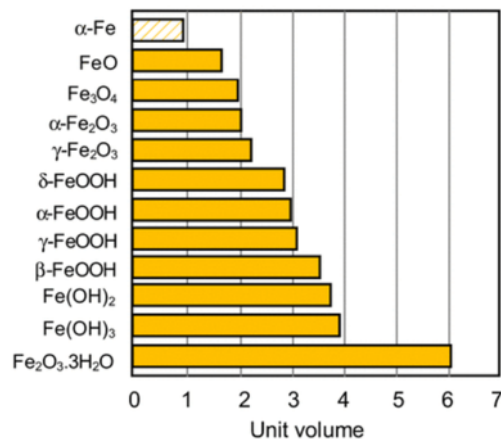


Figure 1.30 Volume of Iron Corrosion Products [35].

### 1.5.3 Protection of Reinforced Concrete

The reinforced concrete structure located close to an aggressive environment rich in chloride, like bridges, suffer intensely of corrosion problem, for this reason, it is impossible to ensure a lifetime that exceeding 50-75 years. Unfortunately, this theoretical period is too short for important bridges, just think that the Tower Bridge in London, UK, is in service over 100 years ago. To increase the durability of these structures often are used specific preventive measures, called additional protection, that act changing the characteristic of concrete, reinforcement, external environment or the structure itself. Sometimes the preventive measures are applied only in some critical points, i.e. joints, anchorages or supports. The different types of additional protection are illustrated schematically in Figure 1.31.

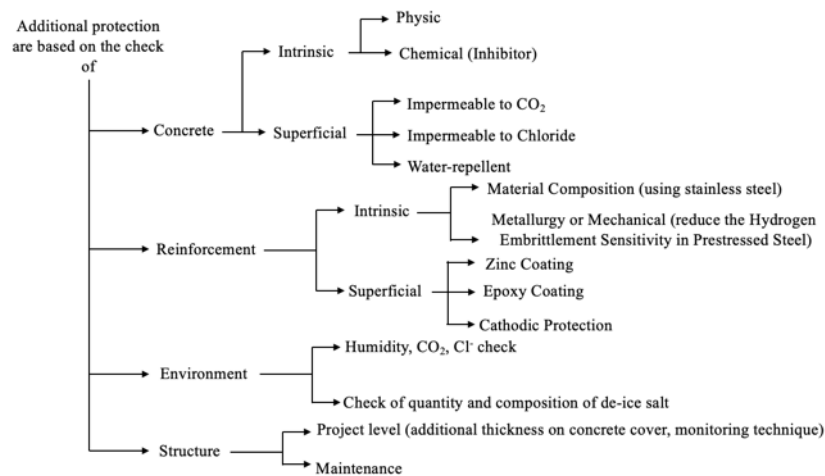


Figure 1.31 Methods of Additional Protection [35].

These technologies are required only in a chloride environment, as bridges located close to seawater, they need to be protected. The principal methods in which these systems work, are shown in Figure 1.32. In some cases when the chloride content is too severe may be advantageous substitute the common low carbon steel rebars with zinc or epoxy coated reinforcement or stainless steel reinforcement, even if the cost of these protections are generally double for coated reinforcement instead for stainless steel reinforcement the cost can be 6 – 9 time greater. On the market are also available several types of inhibitors, indicative value that can help in choosing are reported in Figure 1.33.

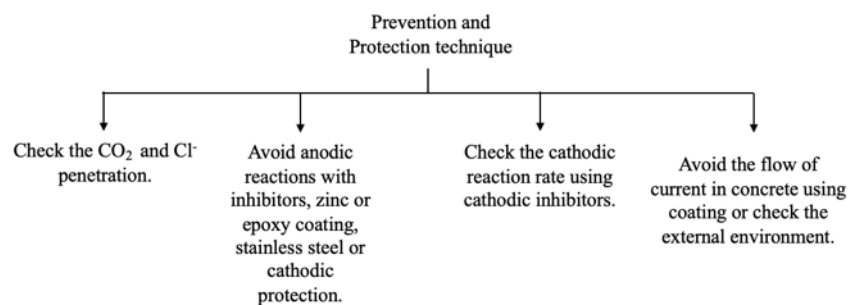
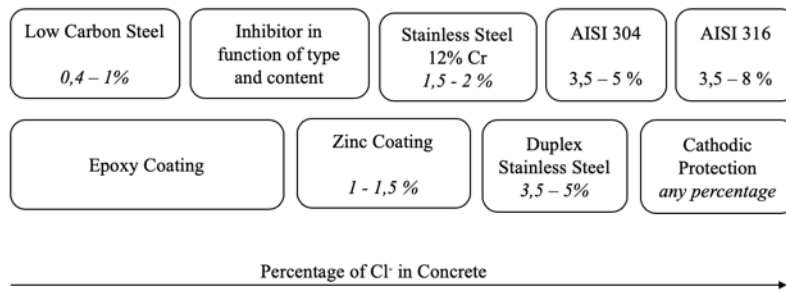


Figure 1.32 Mechanism of Additional Protection [34].



**Figure 1.33** Protection used in different Chloride Environments [34].

## 2 Materials

This thesis work is focused on evaluating the performance of enamel coatings on rebar surface and on the inner diameter of steel pipelines. In both study cases, two types of enamel are applied: T-001 slurry, supplied by TOMATEC, and GP2118 powder, supplied by PEMCO. The chemical composition is presented in Table 2.1. Firstly, the specimens are properly brushed to remove the superficial oxides that can compromise the coating adhesion. Subsequently, the enamel slurry is manually sprayed in the pipeline and on rebar surface using a spray gun jet with compressed air. After that, the specimens are heated at 150 °C for 15 min to drive off the water content afterwards, they are heated again until 815 °C for 15 min and finally cooled to room temperature. On the other hand, the GP2118 enamel powder, with an average particle size of 32.8  $\mu\text{m}$ , is deposited using electrostatic spraying. An electric field is generated between the specimen and the gun nozzle so the enamel powders are induced to cover the sample. After that, the coated specimens are heated at 843 °C for 10 min in a furnace and cooled to room temperature. An API 5L X65 steel pipeline, realized by MRC Global and manufactured by cold working plastic deformation, is the substrate taken into consideration. The steel chemical composition is shown in Table 2.2. On the contrary, the rebar is manufactured through a casting technique where the melted metal, with the chemical composition shown in Table 2.3, is poured inside a mold. The regarding rebars have 2.54 cm (1 inch) diameter. Furthermore, epoxy coated rebars are realized as a comparison with the enamel-coated ones. In this case, LOCTITE® Epoxy Marine is used to coat the samples.

**Table 2.1** Chemical Compositions of Borosilicate Glass T-001 and GP2118 (%wt).

<i>Elements</i>	<i>SiO<sub>2</sub></i>	<i>B<sub>2</sub>O<sub>3</sub></i>	<i>Na<sub>2</sub>O</i>	<i>CaO</i>	<i>MnO<sub>2</sub></i>	<i>Al<sub>2</sub>O<sub>3</sub></i>	<i>TiO<sub>2</sub></i>	<i>K<sub>2</sub>O</i>	<i>Fe<sub>2</sub>O<sub>3</sub></i>	<i>MgO</i>	<i>BaO</i>	<i>Others</i>
<i>T-001</i>	60.3	12.84	7.20	2.37	5.37	4.49	0.14	2.12	3.48	0.17	1.47	0.05
<i>GP2118</i>	57.5	16.95	9.60	3.31	4.70	1.02	1.41	3.63	1.49	0.21	0.04	0.14

**Table 2.2** Chemical Composition of Steel Pipe.

<i>Elements</i>	<i>C</i>	<i>Mn</i>	<i>P</i>	<i>S</i>	<i>Si</i>	<i>Cu</i>	<i>Ni</i>	<i>Cr</i>	<i>Mo</i>	<i>Al</i>	<i>V</i>	<i>Fe</i>	<i>Others</i>
<i>%wt</i>	0.17	1.15	0.07	0.02	0.26	0.10	0.04	0.07	0.07	0.024	0.02	98	0.006

**Table 2.3** Chemical Composition of Steel Rebar.

<i>Elements</i>	<i>C</i>	<i>Mn</i>	<i>P</i>	<i>S</i>	<i>Si</i>	<i>Cu</i>	<i>Ni</i>	<i>Cr</i>	<i>Mo</i>	<i>Sn</i>	<i>V</i>	<i>Co</i>	<i>Fe</i>
<i>%wt</i>	0.38	1.00	0.12	0.06	0.18	0.37	0.20	0.10	0.07	0.03	0.02	0.01	97.4



## 3 Methods

In this section are presented the theoretical models and the experimental techniques that are used in this thesis work. Firstly, the vibration pipe model is illustrated and secondly, the corrosion process and the characterization technique for the rebar samples are described.

### 3.1 Metal Pipe under Environmental and Vibrating Effects

#### 3.1.1 Soil-Pipe Interaction Model

To ensure safety acceptable level of stresses and deformation in a structure is necessary to understand how a structure interacts with the soil during the load application. In detail, the soil-pipe interaction induces vibration in the system, the vibration analysis is studied considering the soil reaction and the pipeline behaviour independently.

##### 3.1.1.1 Soil Model

The soil model is a mathematical expression that is developed in bi-dimensional space to approximate the behaviour of a tri-dimensional ground. These models are not a complete description of the ground but they only "capture" some key aspects of the interaction between the soil and the structure. Therefore, soil models do not provide a realistic description of the ground but an approximation starting on the material ground characteristic. Firstly, the soil can be classified into two different classes.

- *Coherent soil*. The applied load causes deformation in an extended portion of the soil, i.e. in some regions that are not located in the print load. It means that the soil is capable to transfer shear stresses. This is the typical behaviour of clay and rocky ground.

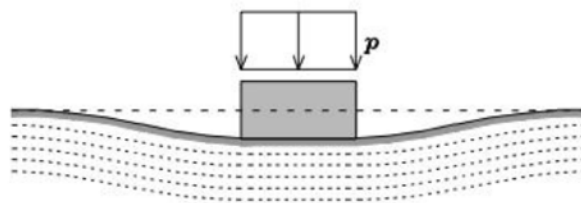


**Figure 3.1** Coherent Soil [37].

- *Incoherent soil*. The applied load interacts only with the print load without changing the external regions. An incoherent soil can be subjected only to dilatation and contraction but not to angular sliding. This soil does not support shear stresses.

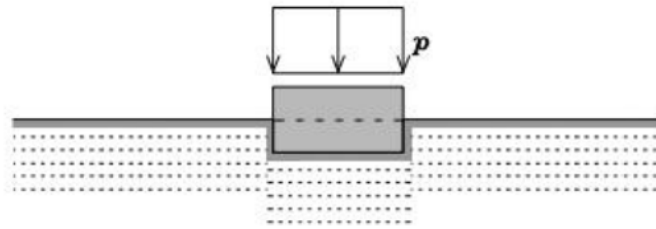


**Figure 3.2** Incoherent soil [37].

### 3.1.1.2 Winkler Elastic Soil

The Winkler elastic soil is a mathematical soil model that is used in the classification of structure bedrocks. This theory is based on the assumption that the soil, in a generic point moves proportionally respect to the surface normal force component, that acts in the same point. Consequently, the failure is elastic and independent of the force that is applied in the other points. Furthermore, from a physical perspective, the Winkler soil can be considered as a bed of independent elastic springs. The Winkler model characterizes the soil with a linear relationship between the subsidence soil-bedrocks at a specific point and the pressure  $\sigma_T(x)$  that acts in the same point. The typical equation for Winkler soil is shown in Equation (3.1).

$$\sigma_T(x) = K_S \cdot y(x) \quad (3.1)$$

where  $K_S$  is the modulus of subgrade reaction and it depends on the soil composition and  $y(x)$  is the soil deflection. The main difficulty of this model is the determination of the modulus of subgrade reaction, in fact, a real soil is based on a stratified structure, therefore,  $K_S$  should depend on the ground depth. For example, in clay soil  $K_S$  takes the value between 5 and 20 N/cm<sup>3</sup> instead for gravel soil the value of  $K_S$  can fluctuate between 10 and 20 N/cm<sup>3</sup>. However, often the value of  $K_S$  is decided with another constant  $k$ , which is evaluated experimentally, based on the soil response under an applied load using a standard plate (30 x 30 cm).

## 3.1.2 Flow Induced Vibrations in the Pipe

### 3.1.2.1 Mathematical Model

The vibrations inside a pipe are analysed using the elasticity linear theory. The pipeline is considered with a homogeneous cross-section that is clamped with rigid supports at both ends. The fluid flows through the pipe with an average velocity  $v$ , the pipe is long  $L$  and  $R$  is the radius of curvature when vibrations occur. Figure 3.3 shows the balance of forces that are applied to an element of fluid in the radial direction. The balance equation of this structure is presented in Equation (3.2).

$$F_{bend} + m \frac{d^2 y}{dt^2} + F_{cent} + \sigma_T = 0 \quad (3.2)$$

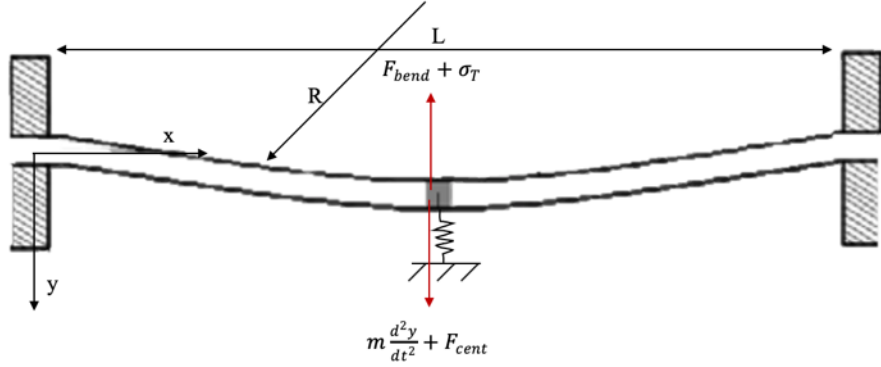


**Figure 3.3** Schematic Section of Vibrating Pipe [38].

where  $F_{bend}$  is the bending reaction,  $F_{cent}$  is the centripetal force related to the effect of the curvature in the pipe section vibration,  $m$  is the total mass of the pipe and fluid per unit length and  $y$  is the deflection at location  $x$  along the pipe.

The value  $F_{bend}$  of and  $F_{cent}$  can be expressed using Equation (3.3) and (3.4).

$$F_{bend} = EI \frac{d^2}{dx^2} \left( \frac{1}{R} \right) \quad (3.3)$$

$$F_{cent} = m_f v^2 \left( \frac{1}{R} \right) \quad (3.4)$$

where  $R$  is the radius of curvature,  $EI$  is the flexural rigidity and  $m_f$  is the fluid mass per unit of length. Replacing Equation (3.3) and (3.4) in Equation (3.2), it gets Equation (3.5).

$$EI \frac{d^2}{dx^2} \left( \frac{1}{R} \right) + m_{tot} \frac{d^2 y}{dt^2} + m_f v^2 \left( \frac{1}{R} \right) + K_s y = 0 \quad (3.5)$$

Where  $m_{tot}$  is the sum of fluid mass  $m_f$  and pipe mass  $m$  per unit of length. It is assumed that all turbulence effect and pipe-fluid friction are taken into account in  $v$  parameter. Reminding the curvature formula in Equation (3.6).

$$\left(\frac{1}{R}\right) = \frac{\frac{d^2 y}{dx^2}}{\left[1 + \left(\frac{dy}{dx}\right)^2\right]^{\frac{3}{2}}} \quad (3.6)$$

Then Equation (3.6) is introduced in Equation (3.5) to get Equation (3.7).

$$EI \frac{d^2}{dx^2} \left( \frac{\frac{d^2 y}{dx^2}}{\left[1 + \left(\frac{dy}{dx}\right)^2\right]^{\frac{3}{2}}} \right) + m_{tot} \frac{d^2 y}{dt^2} + m_f v^2 \left( \frac{\frac{d^2 y}{dx^2}}{\left[1 + \left(\frac{dy}{dx}\right)^2\right]^{\frac{3}{2}}} \right) + K_s y = 0 \quad (3.7)$$

Considering the pipe section sufficiently rigid, the pipe deflection is going to be small respect the pipe length so  $\frac{dy}{dx}$  in Equation (3.7) can be neglected and it is got Equation (3.8).

$$EI \frac{d^4 y}{dx^4} + m_{tot} \frac{d^2 y}{dt^2} + m_f v^2 \frac{d^2 y}{dx^2} + K_s y = 0 \quad (3.8)$$

Then the boundary conditions for a clamped pipe are shown in Equation (3.9), (3.10), (3.11) and (3.12).

$$y(0, t) = 0 \quad (3.9)$$

$$y(L, t) = 0 \quad (3.10)$$

$$\frac{dy}{dx}(0, t) = 0 \quad (3.11)$$

$$\frac{dy}{dx}(L, t) = 0 \quad (3.12)$$

The initial condition is reported in Equation (3.13).

$$y(x, 0) = 0 \quad (3.13)$$

Briefly, the Equation (3.8) is a partial differential equation, that describes the pipe vibration due to fluid flow and the solution has been studied with MATLAB program. The MATLAB code used to solve the system is shown in Appendices 9.1.

### 3.1.2.2 Maximum Elastic Deflection for Vibrating Pipe

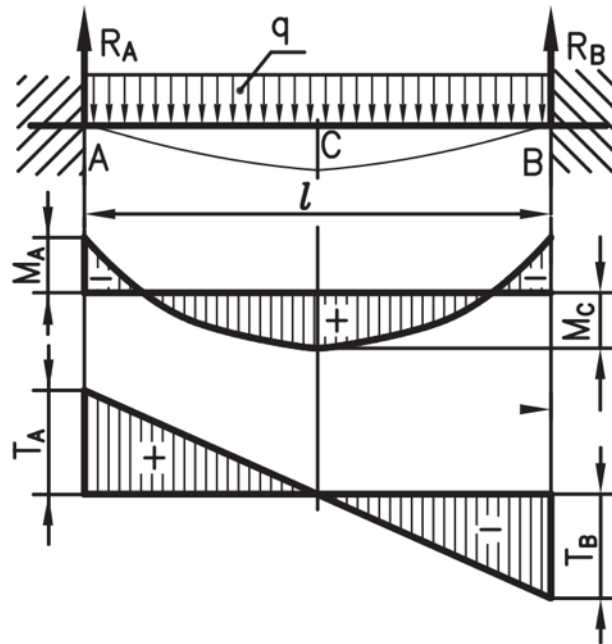


**Figure 3.4** Distribution of load in a double-clamped beam:  $R_A = R_B = ql/2$ ;  $M_A = M_B = -ql^2/12$ ;  $M_C = ql^2/24$ ;  $T_A = R_A$  and  $T_B = -R_A$ . Figure taken from Tabella H.1, “Travi variamente vincolate e sottoposte ai tipi di carichi più comuni”. Hoepli.

The fluid flow induces vibrations in the pipeline so it is essential that the maximum pipe deflection is lower than the plastic deformation to avoid a permanent modification in the line. To estimate this value of maximum deflection  $y_{max}$  is required some assumptions. The pipeline is considered as a beam with a pipe section, double clamped and subjected to uniform load, as shown in Figure 3.4.

In this model, the value of maximum deflection  $y_c$  in Figure 3.4 is equal to  $y_{max}$  and it is calculated with Equation (3.14).

$$y_{max} = \frac{ql^4}{384EI} \quad (3.14)$$

$q$  in the uniform load,  $l$  is the beam's length,  $E$  is Young's modulus and  $I$  is the inertia's moment. In this case of study, the system has a pipe section and the inertia moment is shown in Equation (3.15).

$$I = \frac{\pi \cdot (D^4 - d^4)}{64} \quad (3.15)$$

Where  $D$  is the outer diameter of the pipe and  $d$  is the inner diameter. All terms in Equation (3.14) are known except for the uniform load  $q$ , but it is achievable from Navier's formula mentioned in Equation (3.16).

$$\sigma_{\max} = \frac{M_C}{W} \quad (3.16)$$

This equation connects the normal stress  $\sigma_{\max}$ , that acts in the point C in Figure (3.4), with the ratio between bending moment  $M_C$ , that acts in the same point, and the resistance modulus  $W$ . The resistance modulus  $W$  can be achievable through Equation (3.17).

$$W = \frac{\pi \cdot (D^3 - d^3)}{32} \quad (3.17)$$

As I mentioned before, in this model the pipeline cannot be subjected to a permanent deformation so the highest value of the permissible normal stress  $\sigma_{\max}$  is equal to the yield strength  $\sigma_y$ , as shown in Equation (3.18).

$$\sigma_{\max} = \sigma_y = \frac{M_C}{W} = \frac{32ql^2}{24\pi(D^3 - d^3)} = \frac{4ql^2}{3\pi(D^3 - d^3)} \quad (3.18)$$

The yield strength  $\sigma_y$  for steel is approximately 235 MPa. In Equation (3.18) the normal stress  $\sigma_{\max}$  is known and the uniform load  $q$  is obtainable, as presented in Equation (3.19).

$$q = \frac{3\pi\sigma_y(D^3 - d^3)}{8E(D^4 - d^4)} \quad (3.19)$$

Finally, replacing Equation (3.19) in Equation (3.14), the maximum deflection  $y_{\max}$  is definitely shown in Equation (3.20).

$$y_{\max} = \frac{\sigma_y l^2 (D^3 - d^3)}{8E(D^4 - d^4)} \quad (3.20)$$

### 3.1.3 MATLAB Analysis of Steel Vibrating Pipe

This section is focused on predicting the behaviour of vibrating pipeline when some parameters of the Equation (3.8) are changed. For this work, it has been decided to keep constant all variables except one, that gets variable values. All the results are obtained by changing a parameter in MATLAB code, shown in Appendices 9.1.

#### 3.1.3.1 Pipe Diameter modify the Pipe Vibration

The changing of pipeline diameter, when fluid flow in a pipeline, influences the vibration of the structure. The pipes diameter for transmission pipeline is generally between 15.24 cm and 121.92 cm (6 in and 48 in) with a variable thickness from 2 mm to 38 mm, as mentioned from Pipe Safety Trust [39]. In this step are taken into account three different pipes with different size, mentioned in Table 3.1.

**Table 3.1** Size of the Pipes.

	<i>Outer Diameter D</i> (cm)	<i>Inner Diameter d</i> (cm)	<i>Thickness s</i> (mm)
<i>Pipe<sub>1</sub></i>	15,24	14,24	10
<i>Pipe<sub>2</sub></i>	50,8	50,3	5
<i>Pipe<sub>3</sub></i>	80	79,98	20

The pipes lengths  $L$  are 10 m, the ground constant  $K_s$  is  $5 \text{ N/cm}^3$  and the fluid rate  $v$  is  $25.78 \text{ m/s}$ . The pipelines are generally made in steel, which has Young's modulus equal to  $220 \text{ GPa}$  and the tensile strength is around  $235 \text{ MPa}$ . It has been supposed that the fluid carried in the pipeline is water, whose density  $\rho_f$  is  $1000 \text{ Kg/m}^3$ . As mentioned before, to avoid plastic deformation in the pipeline, it necessary evaluate the maximum deflection  $y_{max}$ , described in Section 3.1.2.2, for each diameter of pipeline  $D_1$ ,  $D_2$  and  $D_3$ . In Table 3.2 are presented the values of  $y_{max}$  for the considered pipes.

**Table 3.2** Maximum Deflection for Pipe with Diameter  $D_1$ ,  $D_2$  and  $D_3$ .

<i>Pipeline Diameter</i>	<i>Maximum Deflection (<math>y_{max}</math>)</i>
$D_1$	6,79 cm
$D_2$	2,13 cm
$D_3$	1,35 cm

Replacing the parameters just got in MATLAB code, shown in Appendices 9.1, the tendency of pipelines vibration with diameter  $D_1$ ,  $D_2$  and  $D_3$  is been achieved. The results are presented in Section 4.

### 3.1.3.2 Ground Constant modify the Pipe Vibration

The type of soil ground influences significantly the pipeline vibration's trend. For this reason, it is essential to examine how the pipeline shape varies in function of the ground soil  $K_s$ . Table 3.3 presents the typical value of  $K_s$  for two different types of ground.

**Table 3.3** Modulus of Subgrade Reactions for Clay and Gravel soil.

<i>Soil Ground</i>	<i>Modulus of Subgrade Reaction <math>K_s</math></i> ( $\text{N/cm}^3$ )
<i>Clay</i>	5 - 20
<i>Gravel</i>	10 - 30

The operating parameters are the same as Section 3.1.3.1, except for  $K_s$ , which is variable in this case and the pipeline diameter is fixed to  $D_1$ . It is tested for clay and gravel soil, the greater and the least values of subgrade reactions modulus  $K_s$ , mentioned in Table 3.3. The trend of how soils influence the vibration of the pipelines are presented in Section 4.1.2.

### 3.1.3.3 Fluid Density modify the Pipe Vibration

The pipeline vibration depends also on fluid density. In this section is studied three different liquid with density:  $\rho_1 = 1000 \text{ Kg/m}^3$  (water),  $\rho_2 = 800 \text{ Kg/m}^3$  (crude oil) and  $\rho_3 = 680 \text{ Kg/m}^3$  (gasoline). The pipe systems in the analysis have the same parameter mentioned in Section 3.1.3.1 but with a flow rate equal to  $v = 25.78 \text{ m/s}$ . After that, substituting the variable just got in MATLAB code, the predictions of pipeline vibrations are obtained, presented in Section 4.1.4.

### 3.1.4 Fluid Dynamic Regime

The motion of a fluid inside a pipeline can be described by two different fluid dynamic regimes, i.e. laminar regime and turbulent regime. Laminar flow, generally, occurs at a low flow rate. The fluid tends to flow without lateral mixing and there are no cross-currents perpendicular to the direction of flow, nor eddies or swirls of fluids. The laminar regime in the pipeline is developed when the Reynolds number is lower than 2100 ( $Re < 2100$ ) [40]. On the other hand, turbulent flow is characterized by chaotic changes in pressure and flow velocity, which lead to the creation of unsteady vortices, which interact each other. The fluid motion is considered turbulence if the Reynolds number is greater than 2100 ( $Re > 2100$ ) [40]. Therefore, the assessment of fluid motion in a pipeline can be easily predicted using the Reynolds number  $Re$ , shown in the Equation (3.21).

$$Re = \frac{dv\rho}{\eta} \quad (3.21)$$

Where  $d$  is the inner diameter of the pipeline,  $v$  is the fluid rate,  $\rho$  is the fluid density and  $\eta$  is the fluid viscosity.

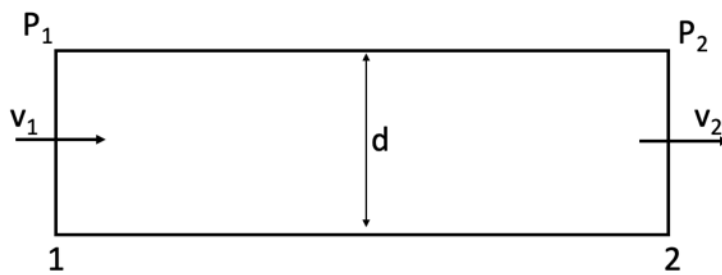


Figure 3.5 Schematic Representation of Pipeline System.

### 3.1.5 Assessment of Pipe Fluid Flow Rate for Turbulence Regime

Taking into consideration a pipeline system located on a plane soil, illustrated in Figure (3.5), in which flow a liquid with density  $\rho$ ,  $d$  is the pipeline diameter,  $v_1$  and  $v_2$  are the fluid rate in the section 1 and 2 and  $P_1$  and  $P_2$  are the pipeline pressure in the section 1 and 2.

The energy balance equation for the pipeline system in Figure (3.5) is presented in Equation (3.22).

$$\frac{v_2^2 - v_1^2}{2} + g(z_2 - z_1) + \frac{P_2 - P_1}{\rho} + R = -l \quad (3.22)$$

The first term is the kinetic contribution, the second term is the potential contribution, the third term is the pressure loss,  $R$  is the friction loss and as the last  $l$  is the fluid dynamic loss. Supposing that the conditions express in Equation (3.23), (3.24) and (3.25) are valid.

$$v_1 = v_2 \quad (3.23)$$

$$z_1 = z_2 \quad (3.24)$$

$$l = 0 \quad (3.25)$$

The Equation (3.22) turns into Equation (3.26).

$$R = \frac{P_2 - P_1}{\rho} \quad (3.26)$$

As mentioned in [41],  $R$  can be express as presented in Equation (3.27).

$$R = \frac{\xi Lv^2}{2d} \quad (3.27)$$

$\xi$  is called Darcy friction coefficient and it assumes for laminar regime the value illustrated in Equation (3.28).

$$\xi = \frac{64}{Re} \quad (3.28)$$

On the other hand, for turbulent regime  $\xi$  is evaluated using Equation (3.29), called Coolbrook Equation.

$$\frac{1}{\sqrt{\xi}} = -2 \log \left( \frac{2.51}{Re \sqrt{\xi + \frac{\epsilon}{3.71D}}} \right) \quad (3.29)$$

$\epsilon$  is the roughness of the pipeline, but often it is preferable to take into consideration the relative roughness  $\frac{\epsilon}{D}$ . Unfortunately, the Coolbrook Equation does not give a direct estimation of  $\xi$ . For this reason, the Moody diagram is used to estimate the parameter  $\xi$ . This diagram is shown in Figure 3.6, where  $\xi = \xi \left( \frac{\epsilon}{D}, Re \right)$ . The pipeline roughness  $\epsilon$  and the Reynolds number  $Re$  are known so the Darcy coefficient  $\xi$  is determined easily using Moody's diagram. Observing the

graph, when the fluid flow fully in a turbulent regime ( $Re > 2100$ ),  $\xi$  no longer depends on  $Re$ . Moreover, if the pipeline walls are smooth, the term  $\frac{\epsilon}{D}$  is negligible. Experimentally, after the determination of relative roughness  $\frac{\epsilon}{D}$ , the Darcy coefficient  $\xi$  is got using the Moody diagram. Afterwards, replacing the Equation (3.27) in Equation (3.26), the Equation (3.30) is obtained.

$$\frac{\xi Lv^2}{2d} = \frac{P_2 - P_1}{\rho} \quad (3.30)$$

Finally, defining  $\Delta P = P_2 - P_1$ , the fluid rate  $v$  is presented in Equation (3.31).

$$v = \sqrt{\frac{2d\Delta P}{\rho\xi L}} \quad (3.31)$$

### 3.1.5.1 Fluid Rate modify the Pipe Vibration

The pipeline deflection depends on the fluid rate and its estimation involves a two steps procedure. Firstly, the fluid-dynamic regime and the fluid rate  $v$  are determined, secondly, the pipeline deflection is predicted. Taking into consideration a pipeline with diameter  $D = 15.24$  cm, length  $L = 10$  m, roughness  $\epsilon = 0.025$  mm. The soil constant  $K_s = 5$  N/cm<sup>3</sup> and the fluid density  $\rho = 1000$  Kg/m<sup>3</sup>. For transmission pipeline, the pressure loss  $\Delta P$  is between 14 bar and 100 bar, as mentioned by Pipeline Safety Trust [6]. Considering three different cases  $\Delta P_1 = 14$  bar,  $\Delta P_2 = 50$  bar and  $\Delta P_3 = 100$  bar, the flow rate  $v_1, v_2$  and  $v_3$  is derived using Equation (3.31), where for steel pipeline  $\epsilon = 0.5$  mm then the relative roughness  $\frac{\epsilon}{D}$  is obtained in Equation (3.32).

$$\frac{\epsilon}{D} = \frac{0.5\text{mm}}{142.4\text{mm}} = 0.0035 \quad (3.32)$$

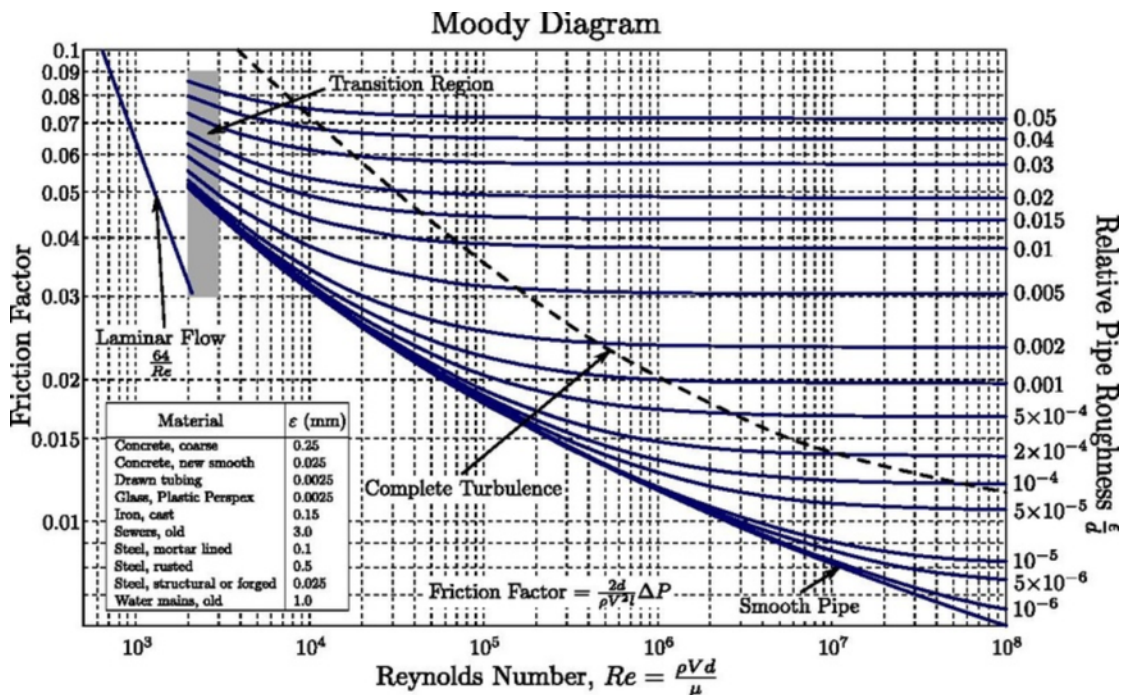


Figure 3.6 Moody Diagram [40].

The Darcy coefficient  $\xi$  for the turbulent regime is defined from Moody diagram and it is shown in Equation (3.33).

$$\xi = 0.06 \quad (3.33)$$

Finally, the flow rate  $v_1$ ,  $v_2$ , and  $v_3$  are estimated as shown in Table 3.4.

**Table 3.4** Fluid Flow Rate.

<i>Pressure Loss <math>\Delta P</math> (bar)</i>	<i>Fluid Rate (m/s)</i>
14	25.78
50	48.72
100	68.89

Substituting the variable just got in MATLAB code, the prediction of pipes vibration are obtained and presented in Section 4.1.3.

### 3.1.6 Flow Induced Vibration in Enamel Coated Pipe

#### 3.1.6.1 Mathematical Model

The mathematical model for the uncoated steel pipeline, mentioned in Section 3.1.2.1, is excellent to describe also vibration in the steel enamel coated pipeline. An update of the Equation (3.8) is required to apply this mathematical model also to the coated ones. Therefore, the partial differential equation for the enamel coated pipeline is presented in Equation (3.31).

$$(E_t I_t + E_c I_c) \frac{d^4 y}{dx^4} + m'_{tot} \frac{d^2 y}{dt^2} + m_f v^2 \frac{d^2 y}{dx^2} + K_s y = 0 \quad (3.31)$$

where  $E_t I_t$  is the pipe flexural rigidity,  $E_c I_c$  is the coating flexural rigidity and  $m'_{tot}$  is the total mass of the system per unit of length and its value is calculated using Equation (3.32).

$$m'_{tot} = \frac{m_t + m_f + m_c}{L} \quad (3.32)$$

in which  $m_t$  is the pipe mass,  $m_c$  is the coating mass and  $m_f$  is the fluid mass inside the pipe. The value of  $m'_{tot}$  is made knowing the different material density, for steel  $\rho_t$  is 7700 Kg/cm<sup>3</sup>, for enamel  $\rho_c$  is approximately 2230 Kg/cm<sup>3</sup> instead for the fluid, it is related to its nature. The mass values are got using the density inverse relationship presented in Equation (3.33).

$$m = \rho \cdot V \quad (3.33)$$

$V$  is the volume of the considered material. The maximum allowable deflection for the coated pipeline cannot be evaluated as done in Section 3.1.2.2. The ceramic coating is characterized by a brittle behaviour so when the applied stress is equal to tensile stress the breaking occurs.

For this reason, ceramic materials are commonly tested in compression instead of traction. Therefore, Equation (3.20) is not valid to describe deflection in steel coated pipeline.

### 3.1.7 MATLAB Analysis of Enamel Coated Pipe

The solutions of Equation (3.31) are studied using the MATLAB code mentioned in Appendices 9.2. In which are used the same initial condition and boundary condition presented in Equations (3.9) to (3.13).

#### 3.1.7.1 Pipe Diameter modify the Vibration in Coated Pipe

As mentioned in Section 3.1.3.1, the changing of pipe diameter influences the pipe deflection. In particular, in this section are studied the vibration in the pipeline enamel coated with the outer diameter  $D_1$ ,  $D_2$  and  $D_3$  and pipes thickness  $s_1$ ,  $s_2$  and  $s_3$ . The coating thickness  $\delta$  is equal to  $340 \mu\text{m}$ , the fluid flow rate  $v$  is  $25.78 \text{ m/s}$ , the pipe length  $L$  is  $10 \text{ m}$  and the Winkler constant  $K_s$  is  $5 \text{ N/cm}^3$ . These data are introduced in MATLAB code, shown in Appendices 9.2 and the results are presented in Section 4.2.1.

#### 3.1.7.2 Coating Thickness modify the Vibration in Coated Pipe

The coating thickness depends on the deposition technique, in particular, this thesis is focused on slurry and powder deposition techniques. The first one provides  $230 \mu\text{m}$  thickness coating instead the second one  $340 \mu\text{m}$  thickness coating [41]. The pipe vibration analysis is done considering these thickness values. Moreover, it is taken into account a system with diameter  $D_1$ ,  $D_2$  and  $D_3$ , the fluid flow rate  $v$  is  $25.78 \text{ m/s}$ , the pipe length  $L$  is  $10 \text{ m}$  and the Winkler constant  $K_s$  is  $5 \text{ N/cm}^3$ . These parameters are replaced in the MATLAB code, shown in Appendices 9.2, and the results are presented in Section 4.2.2.

#### 3.1.7.3 Fluid Flow Rate modify the Vibration in Coated Pipe

This section is focused on analyzing how the fluid flow rate influences the vibrations in a coated pipe. In particular, resuming the procedure explains in Section 3.1.5.1. Firstly, the fluid dynamic regime and the fluid rate  $v$  are determined and secondly, the pipe deflection is achieved. The system has a pipe diameter equal to  $D_1$  and a pipe length  $L$  of  $10 \text{ m}$ . The chosen fluid is water, so the density  $\rho$  is  $1000 \text{ Kg/m}^3$  and the viscosity  $\eta$  is  $0.894 \cdot 10^3 \text{ Pa} \cdot \text{s}$ . The pressure loss  $\Delta P$  is variable and assumes values  $\Delta P_1 = 14 \text{ bar}$ ,  $\Delta P_2 = 50 \text{ bar}$  and  $\Delta P_3 = 100 \text{ bar}$ . Supposing a laminar fluid dynamic regime, the flow rate  $v$  can be obtained using the Poisselle Equation, mentioned in Equation (3.34).

$$v = \frac{\Delta P d^2}{32\eta L} \quad (3.34)$$

Taking into consideration all above mentioned parameters, in the Equation (3.34)  $\Delta P$  is replaced by  $\Delta P_1$  and  $d$  by  $D_1$  then Equation (3.35) is obtained.

$$v = \frac{\Delta P_1 D_1^2}{32\eta L} = 113661 \frac{\text{m}}{\text{s}} \quad (3.35)$$

Using Equation (3.21), the value of the Reynolds number is presented in Equation (3.36).

$$\text{Re} = \frac{D_1 v \rho}{\eta} \sim 10^9 \quad (3.36)$$

In short, in this system, the fluid dynamic regime is completely turbulent. Furthermore, the enamel surface roughness  $\epsilon$  is 0.0025 mm, as shown in Figure 3.6, so the relative roughness is achieved using Equation (3.37).

$$\frac{\epsilon}{d} = \frac{0.0025 \text{ mm}}{142.4 \text{ mm}} = 1.64 \cdot 10^{-5} \quad (3.37)$$

Known these parameters and using the Moody diagram, shown in Figure 3.6, the Darcy coefficient  $\xi$  is achievable and presented in Equation (3.38).

$$\xi = 0.009 \quad (3.38)$$

In summary, the fluid rate  $v'_1$ ,  $v'_2$  and  $v'_3$ , that are associated with pressure losses  $\Delta P_1$ ,  $\Delta P_2$  and  $\Delta P_3$ , are obtained using Equation (3.31). The resulting values are presented in Table 3.5.

**Table 3.5** Fluid Rate in Enamel Coated Steel Pipeline for several Pressure Loss.

<i>Pressure Loss <math>\Delta P</math> (bar)</i>	<i>Fluid Rate <math>v'</math> (m/s)</i>
14	217
50	411
100	582

The values of fluid rate  $v'_1$ ,  $v'_2$  and  $v'_3$  are then replaced in the MATLAB code and the results are presented in Section 4.2.3.

### 3.1.7.4 Ground Constant modify the Vibration in Coated Pipe

The pipe vibrations in an enamel coated pipe depend also on the ground nature. The most diffused types of soil and the typical values of  $K_s$  are presented in Table 3.3. In this section, it is considered a coated pipe with diameter  $D_1$ , length  $L$ , fluid rate  $v_1$  and the coating thickness equal to 340  $\mu\text{m}$ . The values of ground soil tested are the same as described in Section 3.1.3.2, in which the corresponding parameters are replaced in the MATLAB code and the result are got, as mentioned in Section 4.2.4.

## 3.2 Corrosion Performance of Steel Rebar Enamel Coated

In this section is presented the main steps to prepare the rebar specimens and the electrochemical analysis, that are used to evaluate the enamel coating performance.

### 3.2.1 Sample Preparation

First of all, the rebars are cut into 5.08 cm (2 inches) length specimens, especially for enamel coated rebar an epoxy mark is required to avoid coating breaking during the cutting operation, as presented in Figure 3.7. Furthermore, epoxy coating and un-coated samples are prepared and tested as a comparison with enamel coating rebars. In this case, LOCTITE® Epoxy Marine is used to cover the steel rebars, that are previously brushed to remove the superficial oxides layers. After that, an electric wire is jointed at one end of each sample using adhesive copper tape then the two cutting surfaces of every specimen are covered with epoxy resin to insulate these areas from corrosion during the electrochemical test. For epoxy-coated samples, the resin is applied also on the external surface of steel samples. This is illustrated in Figure 3.8 and 3.9. Finally, the specimens are dried in air for 3 days before the beginning of the electrochemical test.



Figure 3.7 Marked Enamel Coated Rebar.



Figure 3.8 Samples Jointed with Wire and Copper Tape.



**Figure 3.9** Epoxy Coated Samples.

### 3.2.2 Visual Observation

The coating quality is checked through a visual observing before the starting of the electrochemical test. The enamel-coated samples have some damaged points where the coating is no longer continuous. These spots are probably due to the contact of the rebars with the furnace supports during the firing step therefore they could act as corrosion starting points and compromise the final coating performance. For this reason, epoxy resin is added on these spots to avoid localized corrosion phenomena. The final result is shown in Figure 3.10.



**Figure 3.10** Epoxy Coated Damages Points.

### 3.2.3 Electrochemical Test

The samples are divided in two groups, the first one is immersed in 3.5 %wt NaCl to examine the corrosion resistance in presence of chloride instead the second one is dipped in a saturated solution of  $\text{Ca}(\text{OH})_2$  with pH 14 to estimate the coating's performance in a similar concrete environment. The solutions are prepared by adding NaCl and  $\text{Ca}(\text{OH})_2$  (Fisher Scientific, Inc.) into distilled water. The samples are monitored periodically for 70 days measuring Open Circuit Potential (OCP), Linear Polarization Resistance (LPR) and Electrochemical Impedance

Spectroscopy (EIS). These tests are done using an Interface 1000E Potentiostat/Galvanostat coupled with ECM8 Electrochemical Multiplexer made by Gamry Instruments. A standard three-electrode system is used for these tests, including a graphite counter electrode, a Saturated Calomel Electrode (SCE) as the reference electrode and the coated sample as the working electrode. An example of the cell is illustrated in Figure 3.11.



**Figure 3.11** Cell for Electrochemical Test.

The analysis set-up is based on record the stable OCP for 1 hour, secondly, the EIS test is performed with a sinusoidal potential wave of 10 mV in amplitude around the OCP and with frequency between 100 kHz and 5 mHz. Finally, the LPR test is determined by a scanning range of  $\pm 15$  mV around the OCP at a scan rate of 0.167 mV/s. All experimental set-up, for clarity, is presented in Figure 3.12, 3.13 and 3.14.

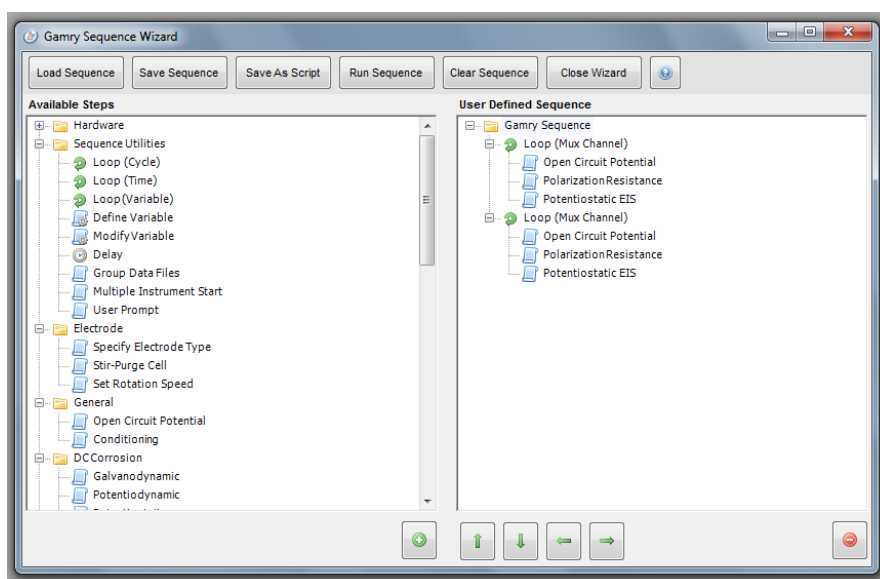


**Figure 3.12** Set-up of Electrochemical Tests.

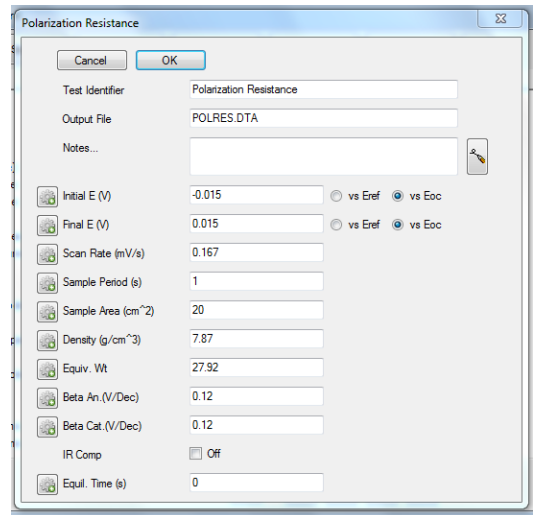
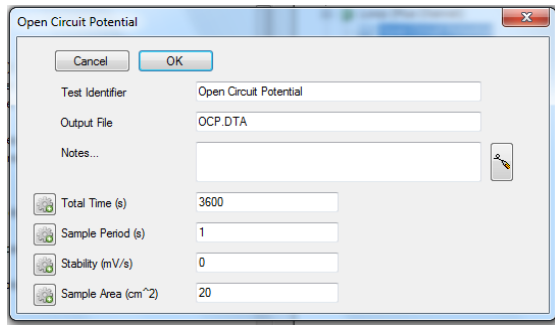


**Figure 3.13** Open Circuit Potential (OCP) and Polarization Resistance Set-up.

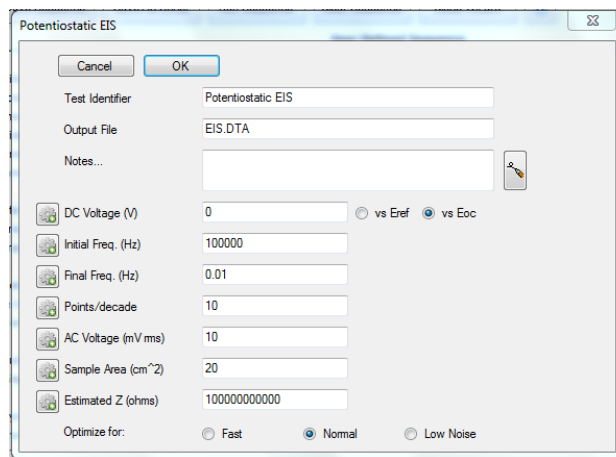


**Figure 3.14** Potentiostatic EIS Set-up.

### 3.2.3.1 Open Circuit Potential (OCP)

The OCP is the potential between the working electrode and the reference electrode when there is no current or potential applied in the cell. This value is determined as the first step and it is used as a reference in the following tests.

### 3.2.3.2 Linear Polarization Resistance (LPR)

The LPR is an electrochemical technique that estimates the polarization resistance ( $R_p$ ) in samples subjected to corrosion phenomena. This value is required to determine the corrosion current density ( $i_{corr}$ ) by the Stern-Geary Equation, illustrated in Equation (3.39).

$$i_{corr} = \frac{\beta_a \beta_c}{[2.303 \cdot R_p (\beta_a + \beta_c)]} \quad (3.39)$$

Where  $\beta_a$  and  $\beta_c$  are the anodic and cathodic Tafel constants and they are equal to 0.12. The polarization resistance ( $R_p$ ) is determined measuring the slope of linear approximation in LPR curve close to zero current, as mentioned in Equation (3.40).

$$R_p = \frac{\Delta E}{\Delta i} \quad (3.40)$$

Where  $\Delta E$  and  $\Delta i$  are the voltage and current increments in the linear portion of the polarization curve at  $i = 0$  [43, 44].

### 3.2.3.3 Electrochemical Impedance Spectroscopy (EIS)

Electrochemical impedance is measured by applying a small sinusoidal AC potential to the electrochemical cell and the response is an AC current signal with the same frequency but shifted in phase. The excitation signal is a function of the time and it is shown in Equation (3.41).

$$E(t) = E_0 \cdot \sin(\omega t) \quad (3.41)$$

$E_0$  is the amplitude of the signal and  $\omega$  is the radial frequency (rad/s), expressible in function of frequency (Hz) through Equation (3.42).

$$\omega = 2\pi f \quad (3.42)$$

The response current signal  $I(t)$ , described in Equation (3.43), is shifted from a phase angle  $\phi$ .

$$I(t) = I_0 \cdot \sin(\omega t + \phi) \quad (3.43)$$

$I_0$  is the current amplitude. Therefore, following the Ohm's law, the impedance is determined from Equation (3.44).

$$Z = \frac{E(t)}{I(t)} = \frac{E_0 \cdot \sin(\omega t)}{I_0 \cdot \sin(\omega t + \phi)} = Z_0 \frac{\sin(\omega t)}{\sin(\omega t + \phi)} \quad (3.44)$$

Where the impedance  $Z$  is a function of the amplitude  $Z_0$  and the phase angle  $\phi$ . The result can be plotted setting the current signal  $I(t)$  on X-axis and imposed the potential  $E(t)$  on Y-axis. The obtained curve has an oval shape, called Lissajous Figure, presented in Figure 3.17. For convenience, the impedance formula is often rewritten with the imaginary unit by the Euler's formula presented in Equation (3.45).

$$\exp(j\phi) = \cos(\phi) + j \cdot \sin(\phi) \quad (3.45)$$

Therefore, it is possible to express the applied potential and the current response as complex function, shown in Equation (3.46) and (3.47).

$$E(t) = E_0 \cdot \exp(j\omega t) \quad (3.46)$$

$$I(t) = I_0 \cdot \exp(j\omega t) \quad (3.47)$$

Finally, the impedance complex function is obtained in Equation (3.48).

$$Z(\omega) = \frac{E(t)}{I(t)} = Z_0 \cdot \exp(j\phi) = Z_0 \cdot (\cos\phi + j\sin\phi) \quad (3.48)$$

Generally, the impedance is plotted with the absolute value of the impedance  $|Z|$  on Y-axis or the shifted phase angle  $\phi$  in function of the logarithm of frequency on the X-axis. These graphs are called Bode plots and an example is shown in Figure 3.18.

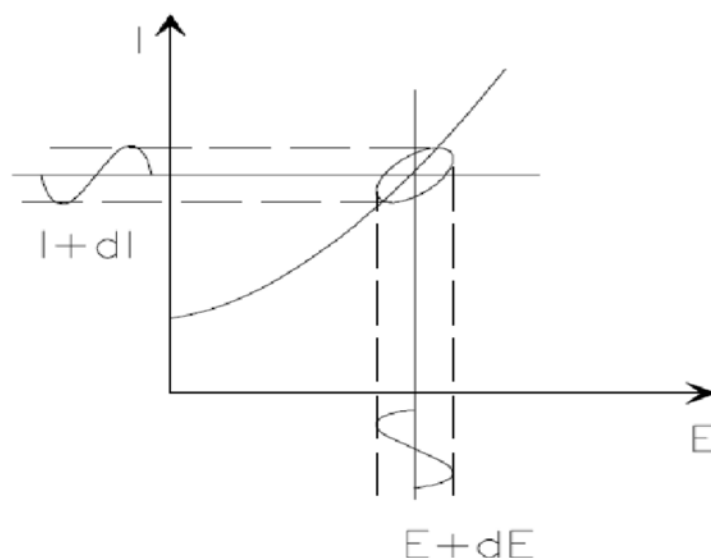


**Figure 3.17** Lissajous Figure. Taken from “Basics of Electrochemical Impedance Spectroscopy” by Gamry Instruments.

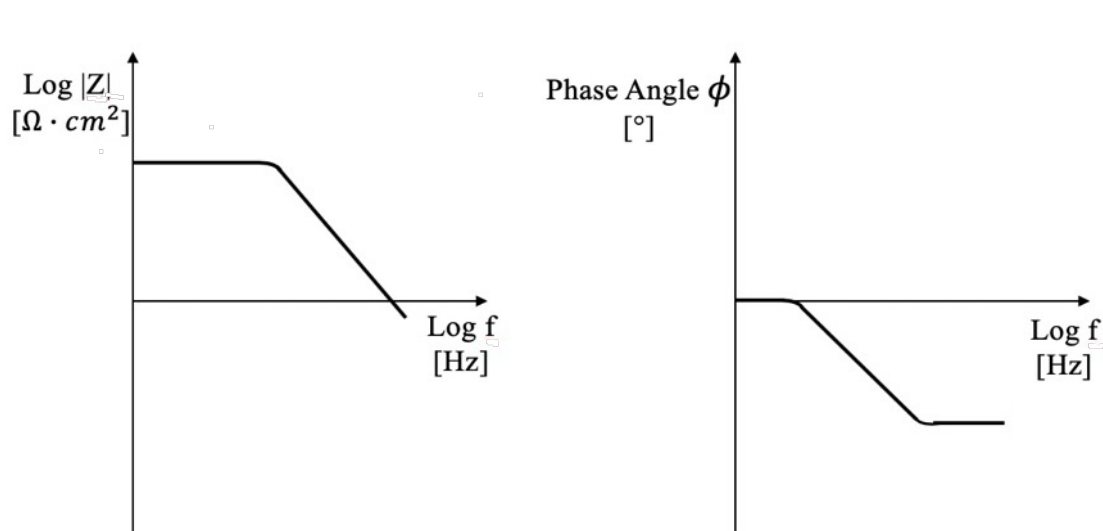


**Figure 3.18** Bode Plot. Taken from “Basics of Electrochemical Impedance Spectroscopy” by Gamry Instruments.

Additionally, the EIS data are analysed by fitting an equivalent Electrical Circuit Model (EEC) of the cell, using the Gamry Electrochemical Analyst Software [42]. This electrical circuit needs to be made properly to predict the coating behaviour in contact with aggressive solutions. In particular, two different circuits are made to predict the enamel coating behaviour. The first one, shown in Figure 3.19, provides a good solution in the first 18 days of specimen immersion when the mass transport phenomena are predominant. The oxygen and water molecules arrive close to the coating surface and they promote corrosion reaction where there is the failure in the coating due to open pores or pinholes.

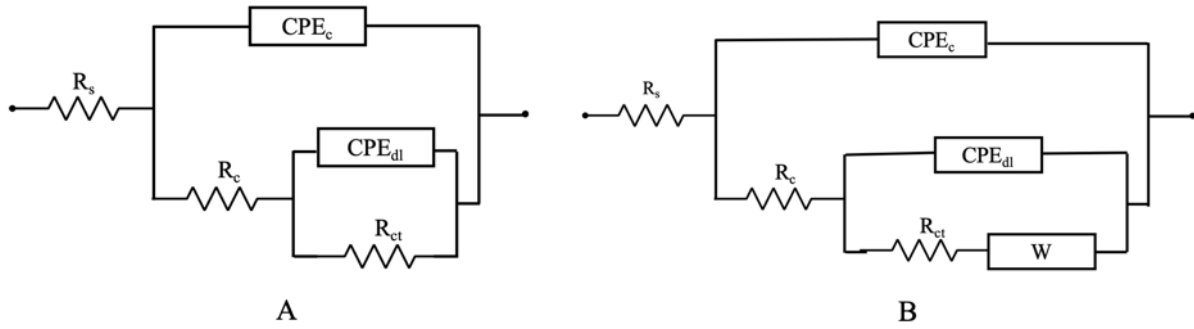


**Figure 3.19** Equivalent Electric Circuit (EEC) Models for Enamel and Epoxy Coated Specimens: A) in the first 10<sup>th</sup> day; B) from the 18<sup>th</sup> day to the end of the tests.

Specifically,  $R_s$  represents the solution resistance,  $R_c$  and  $C_c$  are the coating resistance and capacitance,  $R_{ct}$  is the charge transfer resistance and  $C_{dl}$  is the double layer capacitance. To take into consideration the coating irregularity, as thickness or roughness, and a non-uniform distribution of surface potential, the coating capacitance  $C_c$  and the double layer capacitance  $C_{dl}$  are replaced with two constant phase elements  $CPE_c$  and  $CPE_{dl}$ . A CPE is an equivalent electrical circuit component that models the behavior of an imperfect capacitor and its impedance is obtained by Equation (3.49).

$$Z_{CPE} = Y^{-1} (j\omega)^{-a} \quad (3.49)$$

Where  $Y$  is proportional to the pure capacitance,  $j$  is the imaginary unit,  $\omega$  is the angular frequency and  $a$  assumes a value between 0 and 1;  $a = 1$  describes an ideal capacitor while  $a = 0$  describes a pure resistor. If the  $Y$  and  $a$  parameters are known, the effective capacitance based on CPE values can be easily obtained by Equation (3.50).

$$C = Y^{\frac{1}{a}} \cdot R^{\frac{1-a}{a}} \quad (3.50)$$

Where  $R_c$ ,  $Y_c$ , and  $a_c$  are used to calculate the effective coating capacitance instead  $C_c$  and  $R_{ct}$ ,  $Y_{dl}$  and  $a_{dl}$  are used to calculate the effective double layer capacitance. The second equivalent electric circuit model, shown in Figure 3.19B, is used to describe the coating behavior after 10 days of immersion. The circuit is completely similar to the first one, except for the Warburg impedance element located in series with double layer resistance  $R_{dl}$ . This additional element takes into account the diffusion contribution on the coating surface due to the accumulation of corrosion products.

### **3.2.4 Visual Observation**

After 70 days, at the end of the electrochemical test, the specimens are removed from the solutions, they are dried and subjected to a visual observation to obtain a first description of the corroded surfaces.

### **3.2.5 Microstructural Analysis**

The coating microstructure is studied using the scanning electron microscope (SEM) because the average dimension of the coating thickness is less than 400 micron so it is impossible to appreciate this details with the traditional optical microscope. The device used for the study is Helios NanoLab DualBeam, which is able to provide a clear description of the coating microstructure and the morphology, using a second electron detector. However, the optical microscope Hirox KH-8700 is used only in the specimens preparation to check the quality of the polish operation.

#### **3.2.5.1 Samples Preparation**

For each kind of samples, it is selected the specimen that apparently shows the better coating surface. After that, all chosen specimens are arranged inside a plastic container in parallel one to the other and raised from the bottom of the container using two wooden sticks. The EpoxyMount Resin and Hardener, provided by Allied High Tech Products, Inc., are combined together in a 3:1 ratio in a beaker and properly mixed to achieve a homogeneous solution. After that, the resin, that is curing, is poured in the container, the polymerization reaction continues for 2 hours until the epoxy resin is completely cured. When the polymerization is ended, the massive block of epoxy resin, that embedded the metal rebars, are sent to the cutting step to obtain square specimens with side of 3 cm and thickness of 0.5 cm. Afterwards the specimen's surfaces are polished until they are lucid. This process is based on the rubbing between the sample and an abrasive disc, in specific, during this step it is essential that the applied pressure is equal in all surface to preserve the flatness of the surface. In addition every time that the abrasive disc is changed from a course one to a fine one, the specimen needs to be rotated of 90°. The polishing operation begins using the coarse abrasive discs, which allow to remove the superficial oxide scale and the finer abrasive discs are used to gradually reduce the surface roughness, until the desired grade of polish is obtained. Basically, it is used the 80, 180, 320, 600, 800 and 1200 grit in succession to polish the samples surfaces. At the end the quality of the polished surfaces is checked using the optical microscope. Before starting the SEM analysis, all polished surfaces are coated with a thin layer of Pd/Au for 45 s using a sputtering technique.



## 4 Results

In this section are presented the results of the experimental analysis and the simulation models. Firstly, the prediction of pipe vibration is shown using the MATLAB code, presented in Appendices 9. Secondly, the electrochemical results are described to evaluate the performance of the enamel coating on steel rebar.

### 4.1 MATLAB Simulations for Steel Vibrating Pipe

The final vibrating models for no-coated pipe is presented in this subsection, in specific the results take into consideration the first 10 s of oscillation.

#### 4.1.1 Pipe Diameter modify the Pipe Vibration

The simulation models described in Section 3.1.3.1 provides the graphs, shown in Figure 4.1. In all of them, it is observable that the maximum displacement of each pipe due to the vibration is lower than the maximum deflection  $y_{max}$  estimated in Table 3.2. Consequently, it is legitimate to assume that the pipelines are not subjected to plastic deformation during operating conditions. Furthermore, increasing the pipe diameter the vibration profile goes gradually from having a sinusoidal trend to an irregular one.

#### 4.1.2 Ground Constant modify the Pipe Vibration

The soil characteristic also influences the pipe vibration, as confirmed in Figures 4.2 and 4.3. The maximum oscillation amplitude in the y-direction is not more than 0.01 m, therefore, any plastic deformation occurs in the pipes. Moreover, looking to the vibration profiles, it is noted that for clay soil there is any change of the curves so the pipe vibration does not depend significantly on this parameter. On the contrary, for a gravel soil with  $K_s = 10 \text{ N/cm}^3$ , the pipe vibrations tend to move periodically from small to high amplitude of oscillation. Instead, for soil with  $K_s = 30 \text{ N/cm}^3$ , the vibration amplitude of oscillation remains constant in the time but there is longitudinal shift respect to the zero axes.

#### 4.1.3 Fluid Rate modify the Pipe Vibration

The fluid rate is a crucial process parameter because an increase of fluid rate operatively means a decrease in the pumping time. The simulation models, shown in Figure 4.4, illustrated how fluid rate influences the pipe vibration. In particular, there is evidence that the oscillation profile is not subjected to any change, in fact, all the curves have the same sinusoidal shape.

#### **4.1.4 Fluid Density modify the Pipe Vibrations**

The pipeline can carry different types of liquids is based on the need. For this reason, it is evaluated which is the dependency of vibration from three different kinds of fluid, such as water, crude oil, and gasoline. The results, presented in Figure 4.5, show that with the increase of fluid density there is a shift of the pipe vibration from sinusoidal to irregular profile, even if the maximum displacement never passes the plastic region.

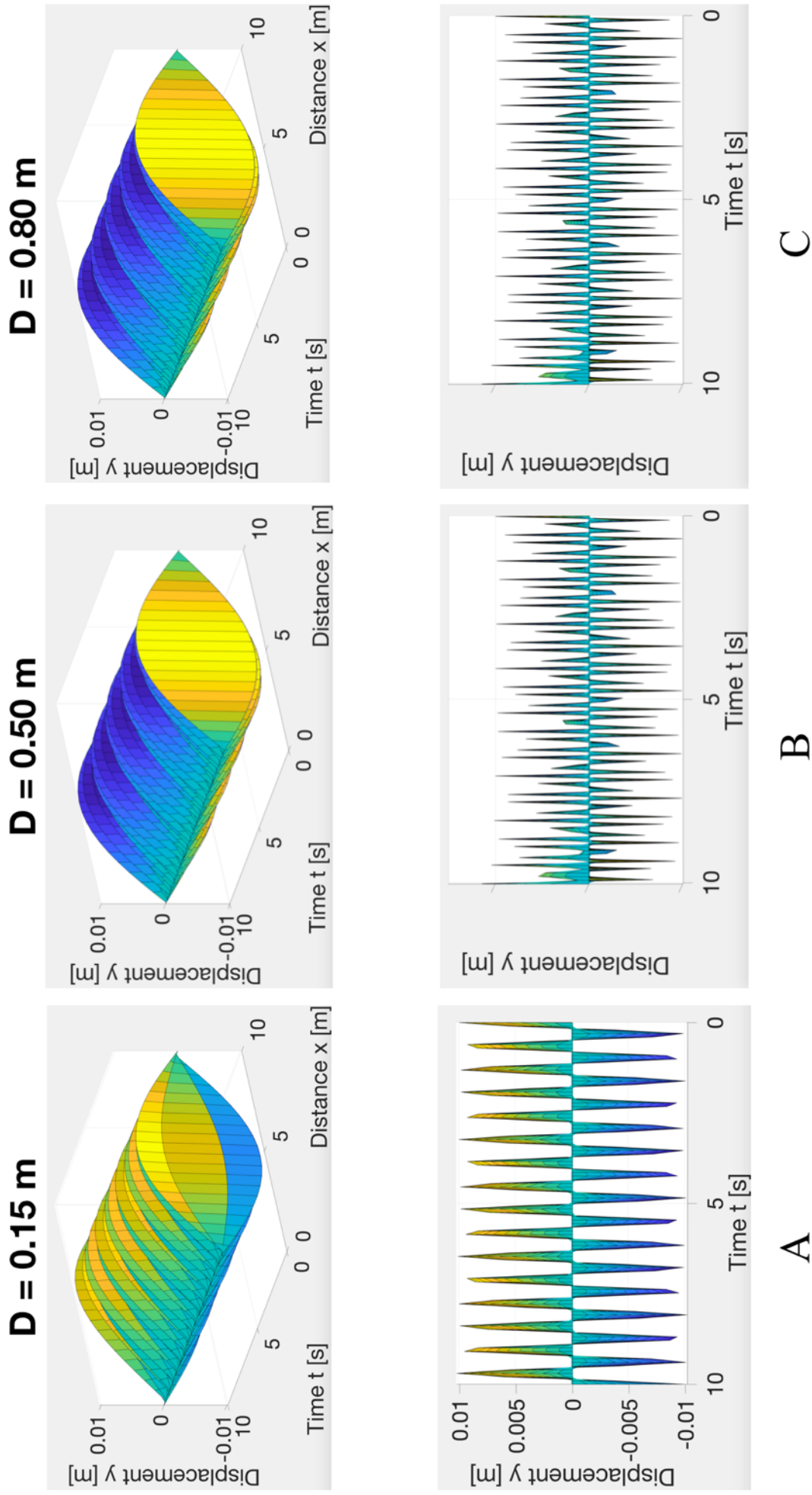


**Figure 4.1** Study of Pipeline Vibration with three Different Diameter: A)  $D_1$ , B)  $D_2$  and C)  $D_3$ .

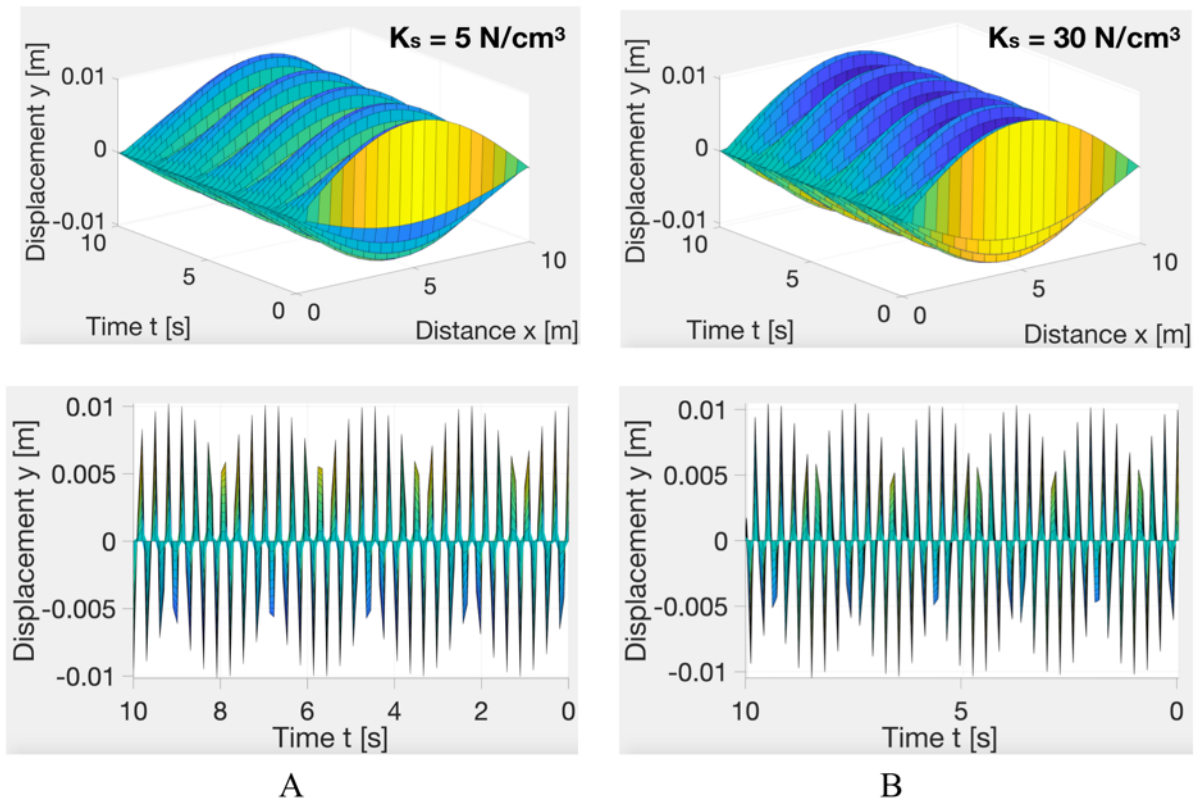


**Figure 4.2** Study of Pipelines Vibration with Clay Soil: A)  $K_s = 5$  N/cm<sup>3</sup>, B)  $K_s = 30$  N/cm<sup>3</sup>.

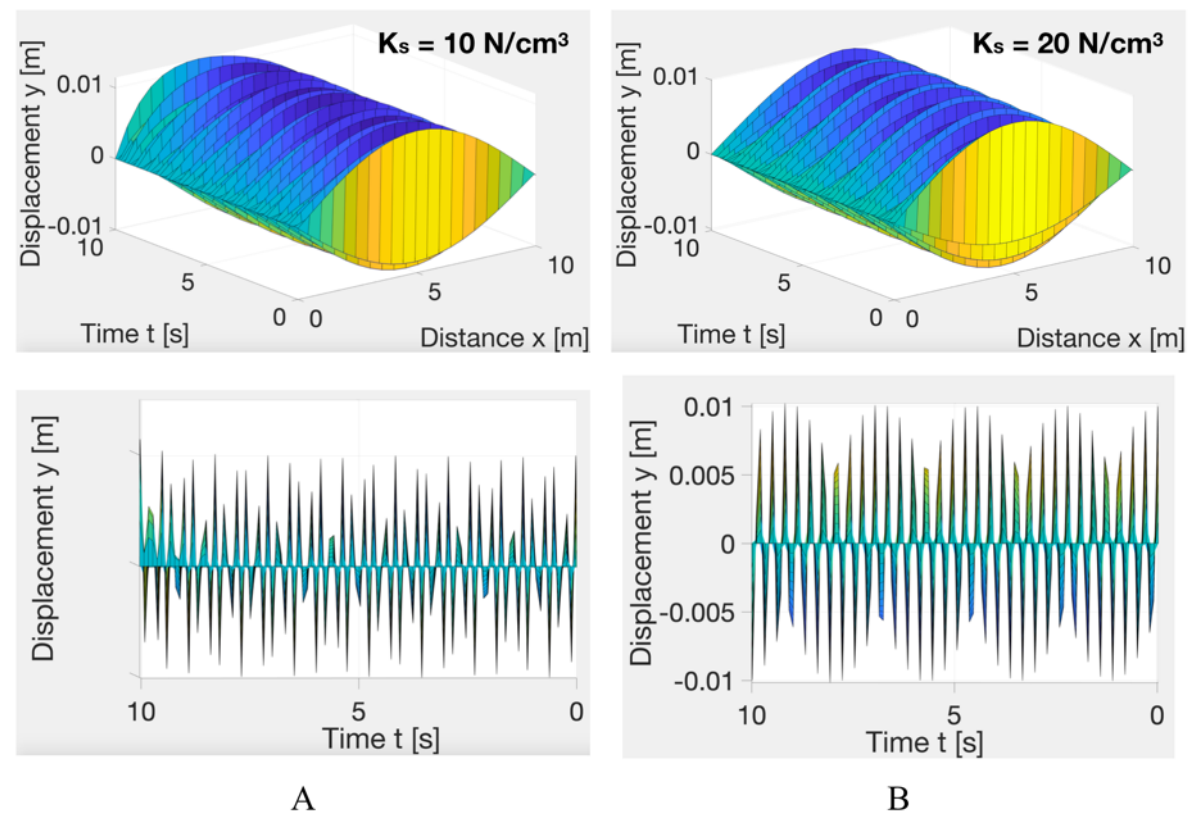


**Figure 4.3** Study of Pipelines Vibrations with Gravel Soil: A)  $K_s = 10$  N/cm<sup>3</sup>, B)  $K_s = 20$  N/cm<sup>3</sup>.

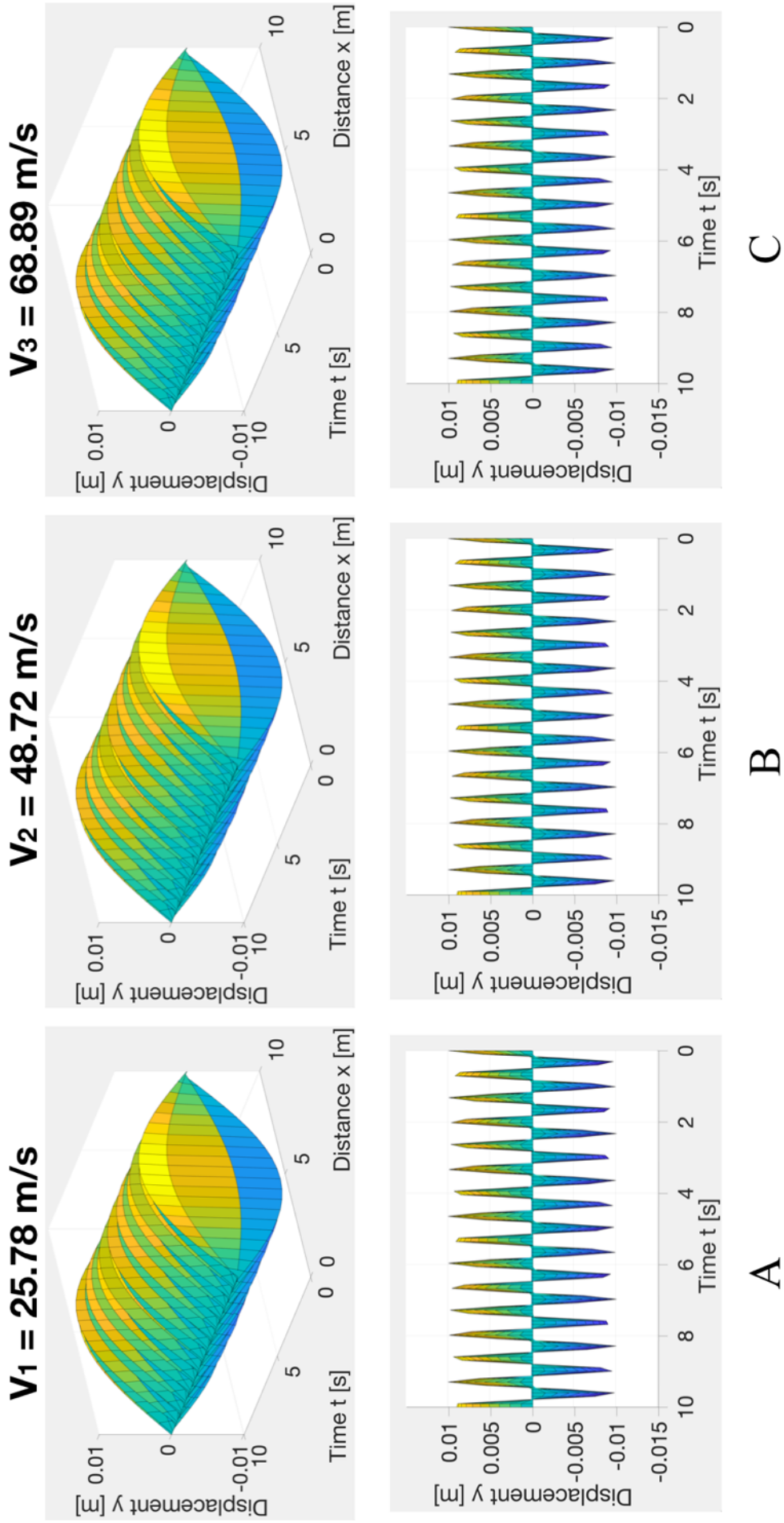


**Figure 4.4** Study of Pipelines Vibration when Flow Rate is variable: A)  $v_1 = 25.78$  m/s, B)  $v_2 = 48.72$  m/s and C)  $v_3 = 68.89$  m/s.

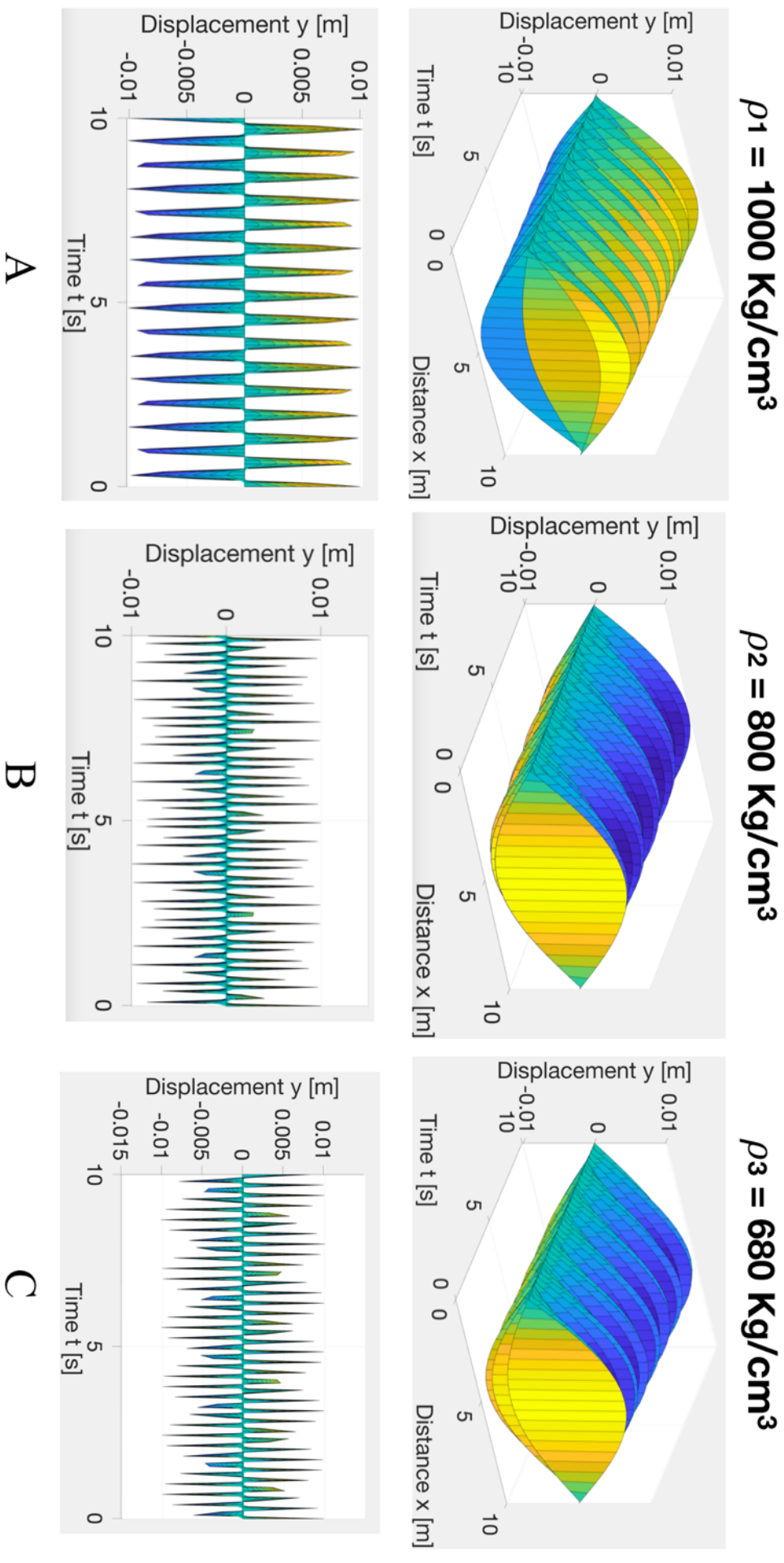


**Figure 4.5** Study of Pipelines Vibration when Fluid Density is variable: A)  $\rho_1 = 1000 \text{ Kg/cm}^3$ , B)  $\rho_2 = 800 \text{ Kg/cm}^3$  and C)  $\rho_3 = 680 \text{ Kg/cm}^3$ .

## **4.2 MATLAB Simulations for Steel Vibrating Pipe Enamel Coated**

The result of the vibrating models for steel pipe coated with enamel are illustrated in this section.

### **4.2.1 Pipe Diameter modify the Coated Pipe Vibrations**

As mentioned before in Section 4.1.1, the pipe diameter is a parameter that influences directly the pipe vibration. In particular, an increase of diameter does not induce a modification in the vibration profile, in fact, the oscillation follows in all cases a sinusoidal profile, as shown in Figure 4.6. The main difference between these three graphs is related to the vibration amplitude, in specific, when the diameter becomes bigger the period of oscillation decreases considerably. Furthermore, the maximum of deflection is less than  $y_{max}$ , the value estimated in Table 5, then any plastic deformation occurs in steel during operative conditions.

### **4.2.2 Coating Thickness modify the Coated Pipe Vibrations**

The coating thickness is another parameter that affects the pipe vibration. In Figure 4.6 and 4.7, are presented the results for two enamel coating with similar chemical composition but different thicknesses. In both figures, it is noticed a similar trend, the oscillation profile remains sinusoidal in all cases and it is not influenced by the increase of diameter. Therefore, the pipe diameter affects more these dynamic models that the coating thickness.

### **4.2.3 Fluid Flow Rate modify the Enamel Coated Pipe Vibrations**

In Section 4.1.3 it was noticed that the increasing of the rate did not modify the pipe vibration so the sinusoidal oscillation remained constant. On the contrary, for the enamel-coated pipe the vibration trend is completely irregular and further from looking sinusoidal. Specifically, this behaviour is observed in all graphs in Figure 4.8. In addition as mentioned in the previous graph, the maximum deflection never passes the material elastic region.

### **4.2.4 Ground Constant modify the Enamel Coated Pipe Vibrations**

The soil nature influences drastically the vibration behavior in enamel coated pipe. Figure 4.9 presents the simulation results for clay soils, where the increasing of the soil constant  $K_s$  the pipe oscillation gradually changes its trend from sinusoidal to a constant amplitude of vibration, but with the shifted value from zero axes. On the other hand, in Figure 4.10 is shown the results for gravel soils, where the pipe vibration behavior remains completely irregular at the changing of the soil constant. This trend is the same that was noticed in the previous Section 4.1.2 for the no-coated pipes.

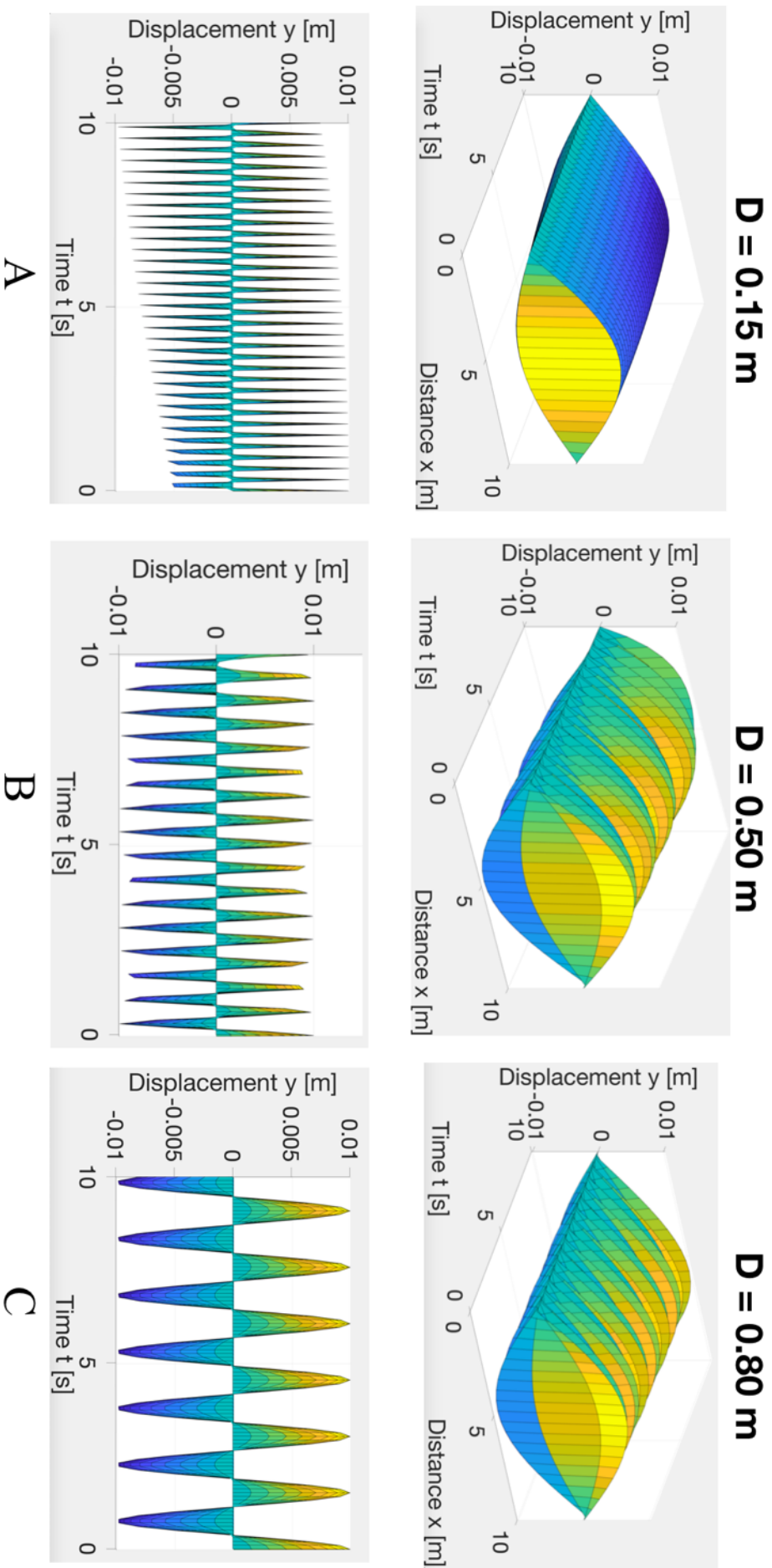


**Figure 4.6** Study of Pipe Vibrations with 340  $\mu\text{m}$  thickness coating and with Diameter: A)  $D_1$ , B)  $D_2$  and C)  $D_3$ .

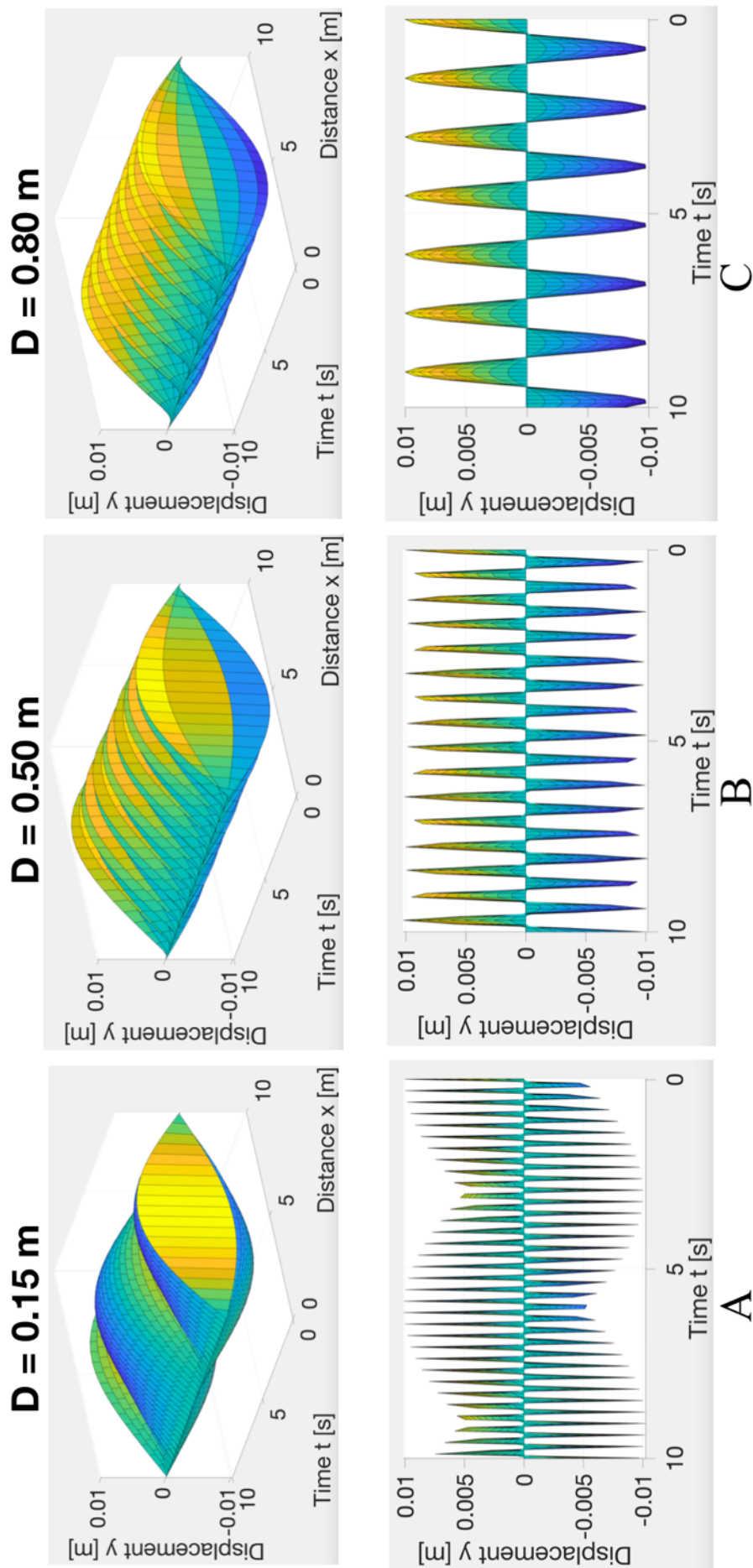


**Figure 4.7** Study of Pipe Vibrations with  $230\ \mu\text{m}$  thickness coating and variable Diameter: A)  $D_1$ , B)  $D_2$  and C)  $D_3$ .

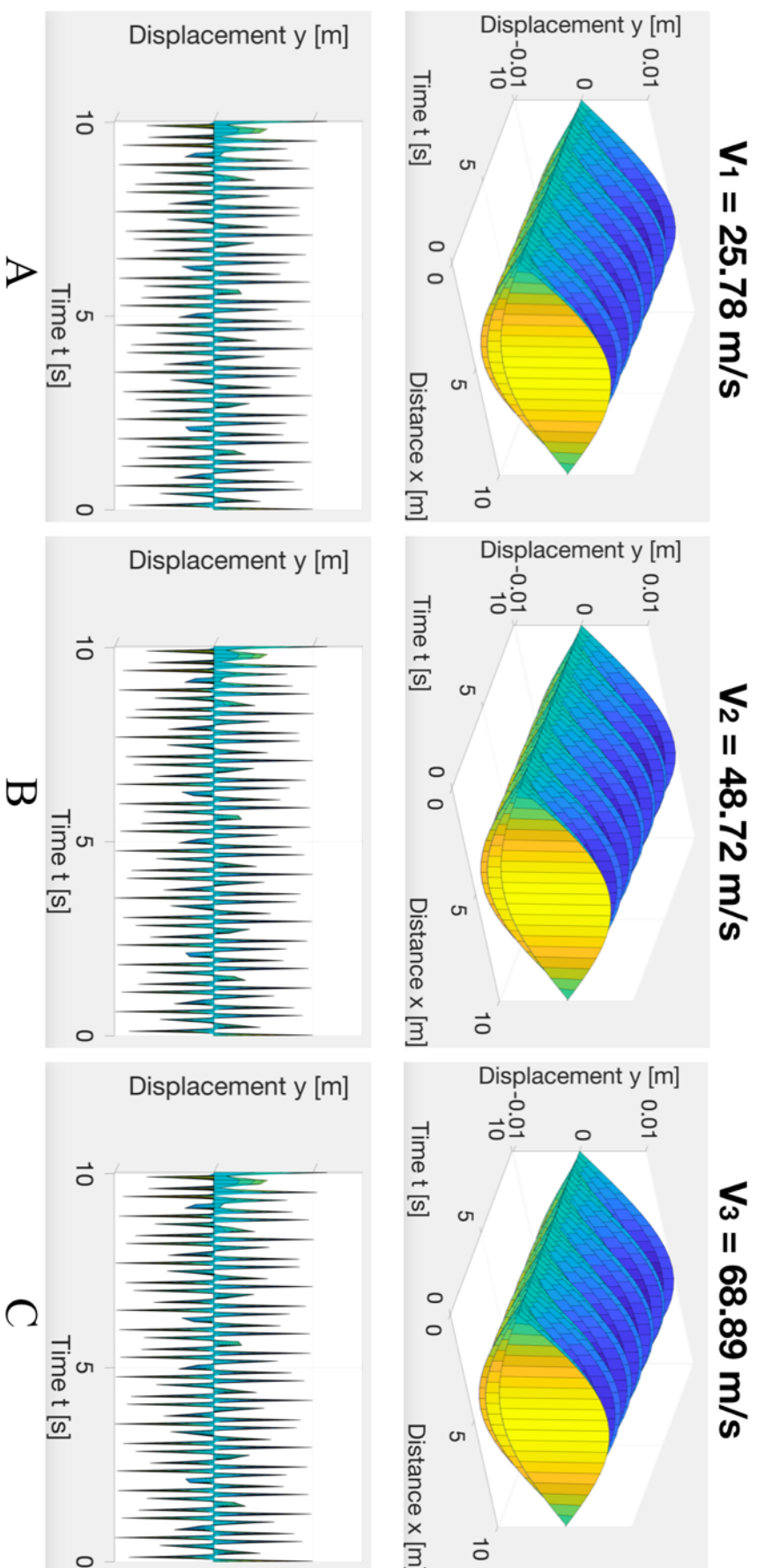


**Figure 4.8** Study of Enamel Coated Steel Pipeline Vibrations with Different Fluid Rate: A)  $v_1$ , B)  $v_2$  and C)  $v_3$ .

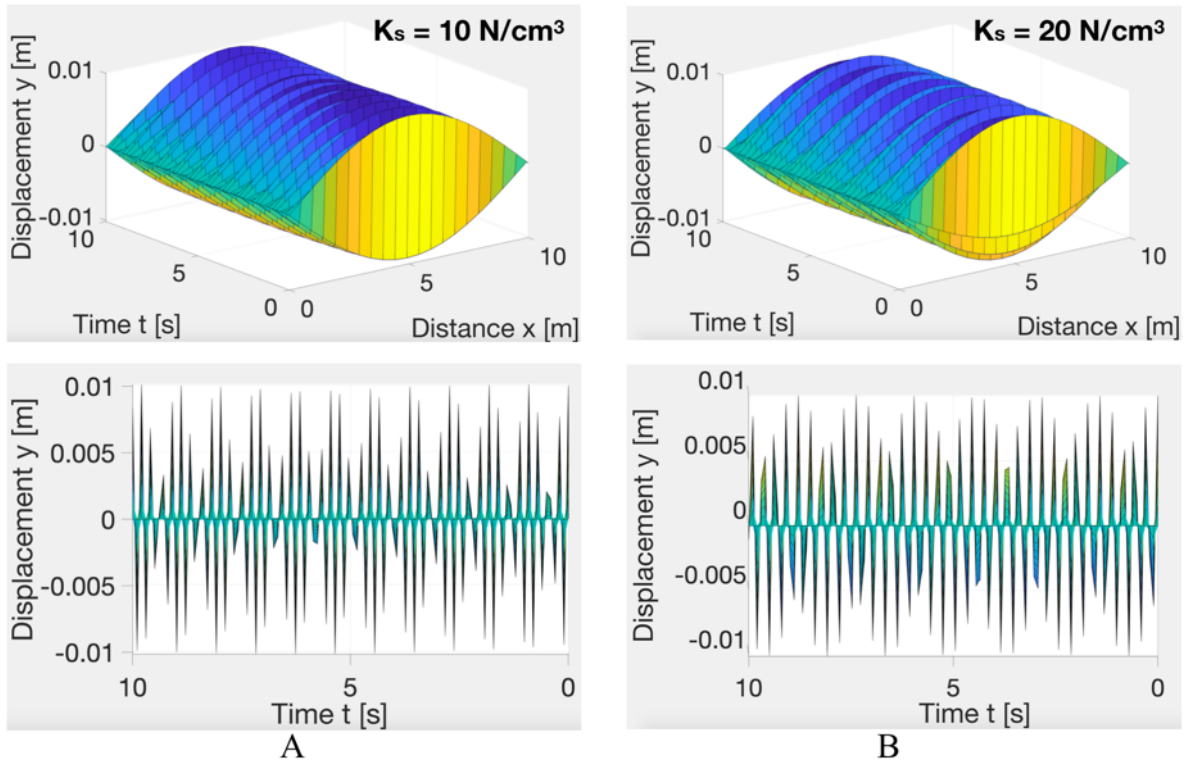


**Figure 4.9** Study of Pipelines Vibration with Clay Soil: A)  $K_s = 10 \text{ N/cm}^3$ , B)  $K_s = 20 \text{ N/cm}^3$ .

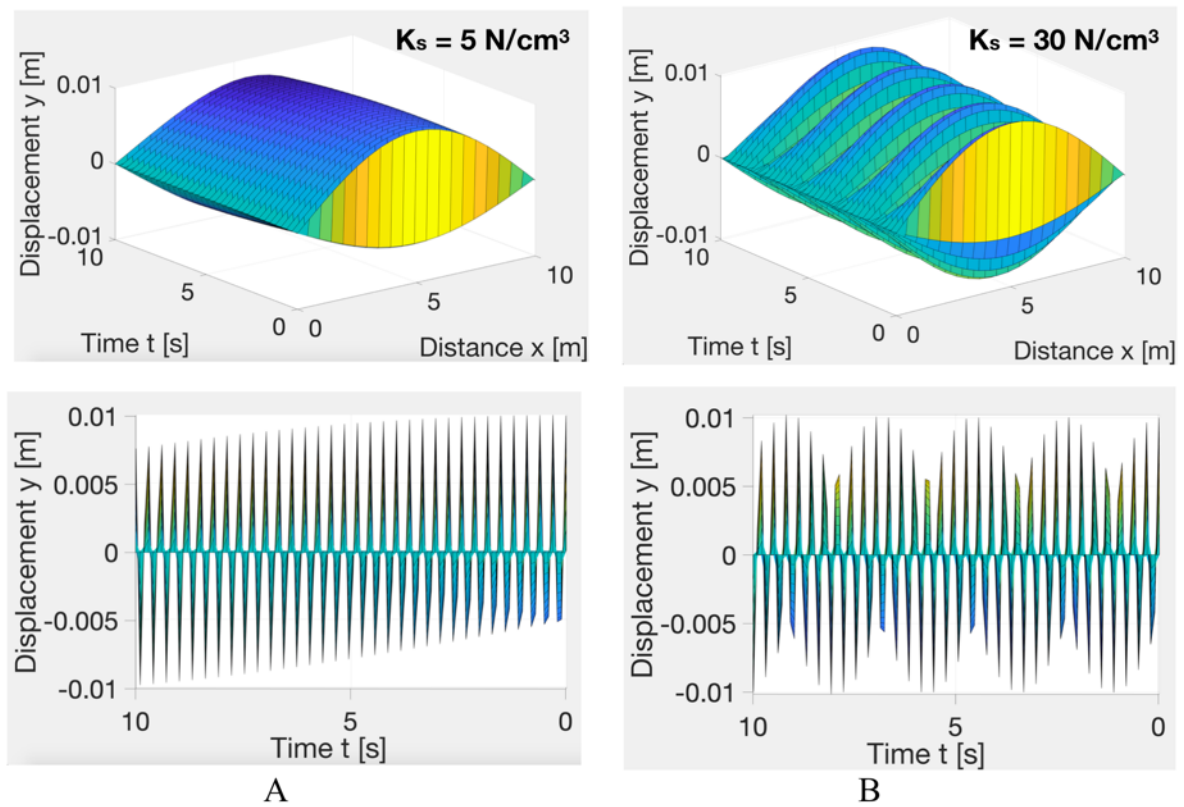


**Figure 4.10** Study of Pipelines Vibrations with Gravel Soil: A)  $K_s = 5 \text{ N/cm}^3$ , B)  $K_s = 30 \text{ N/cm}^3$ .

### 4.3 Performance of Enamel Coating

The results of the electrochemical tests and the SEM analysis are presented in this section, in specific, the  $\text{Ca}(\text{OH})_2$  results are mentioned first and followed by the NaCl ones.

#### 4.3.1 Electrochemical Test

*Open Circuit Potential (OCP).* Figure 4.11 shows the deviation values of OCP for specimens that are immersed in  $\text{Ca}(\text{OH})_2$  solution for 70 days. In the first 10 days the values are unstable and they oscillate between -0.33 V and -0.5 V. In the following days, there is a dramatic drop down of the potentials, that reaches the coatings potential approximately to -0.56 V. The OCP values for GP2118 and T-001 coatings keep rapidly the constant value around -0.48 V. On the contrary, the uncoated and epoxy-coated samples show gradual decreasing of the OCP values after the 18<sup>th</sup> day of immersion, but after 46 days, it takes the defined value of -0.68 V. Regarding the samples that are immersed in the NaCl solution, the OCP results are shown in Figure 4.12. In the first 10 days, the potentials slightly fluctuated, but after that, the curves achieve a constant trend. Specifically, the uncoated sample have the lowest potential around -0.73 V instead the epoxy coated specimens has the highest OCP values until the 32<sup>nd</sup> day. Afterwards there is a slight potential reduction from -0.58 V to -0.63 V. The two enamel coated specimens rapidly get stable OCP values with a limited fluctuation of the potential at -0.68 V.

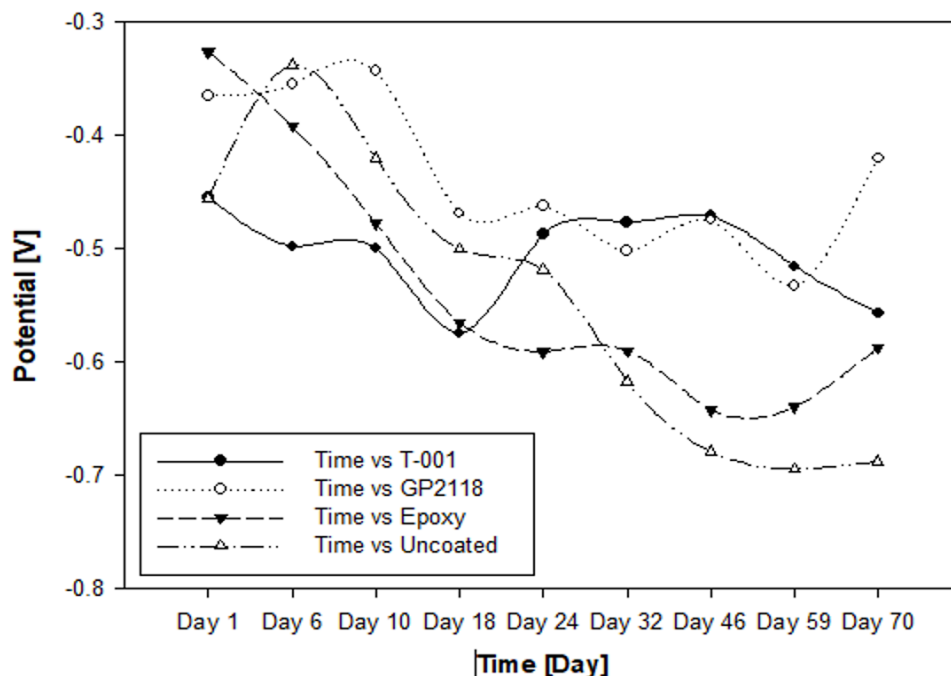


Figure 4.11 Open Circuit Potential for  $\text{Ca}(\text{OH})_2$  Solution.

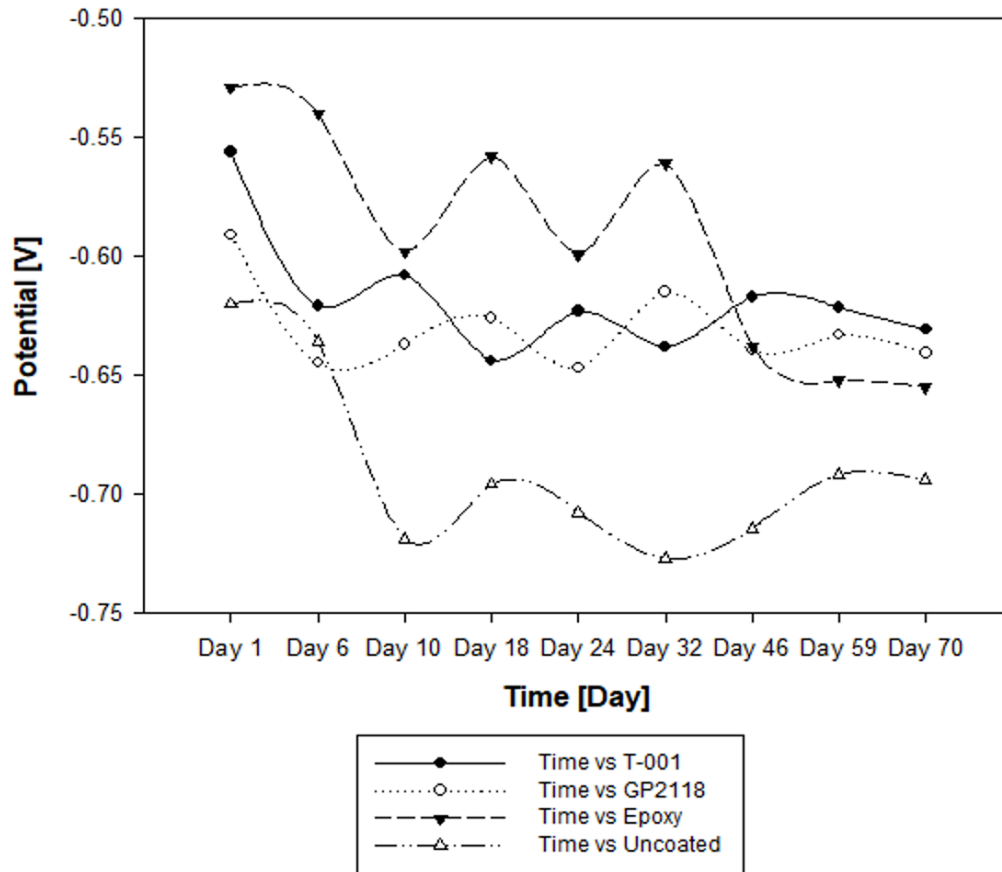


Figure 4.12 Open Circuit Potential for NaCl Solution.

*Linear Polarization Resistance ( $R_p$ )*. The trend of polarization resistance curves is presented in Figure 4.13 and 4.14. The first figure shows the deviation values for specimens in  $\text{Ca}(\text{OH})_2$  solution, in which the polarization resistance has a gradually decrease for all samples in the first 20 days, but in the following days, they achieve a constant value. The enamel and epoxy coatings have a comparable polarization resistance around  $5 \times 10^5 \Omega/\text{cm}^2$  instead the uncoated sample shows a polarization resistance of  $1 \times 10^2 \Omega/\text{cm}^2$ . In specific, both enamel coatings show a higher resistance than the epoxy one. In other words, greater is the polarization resistance better is the protection that the coating provides, then, the T-001 slurry coating presents the best performance. The second figure illustrates the trend of  $R_p$  for specimens that are immersed in NaCl solution. In this case, the overall performance has a pronounced fall in the first 10 days, but after that, the curves continue to decline with a lower slope than before. In particular, the uncoated specimens also present a significantly below polarization resistance than the coated rebars, in fact, there is a great difference of value between these samples, approximately five orders of magnitude.

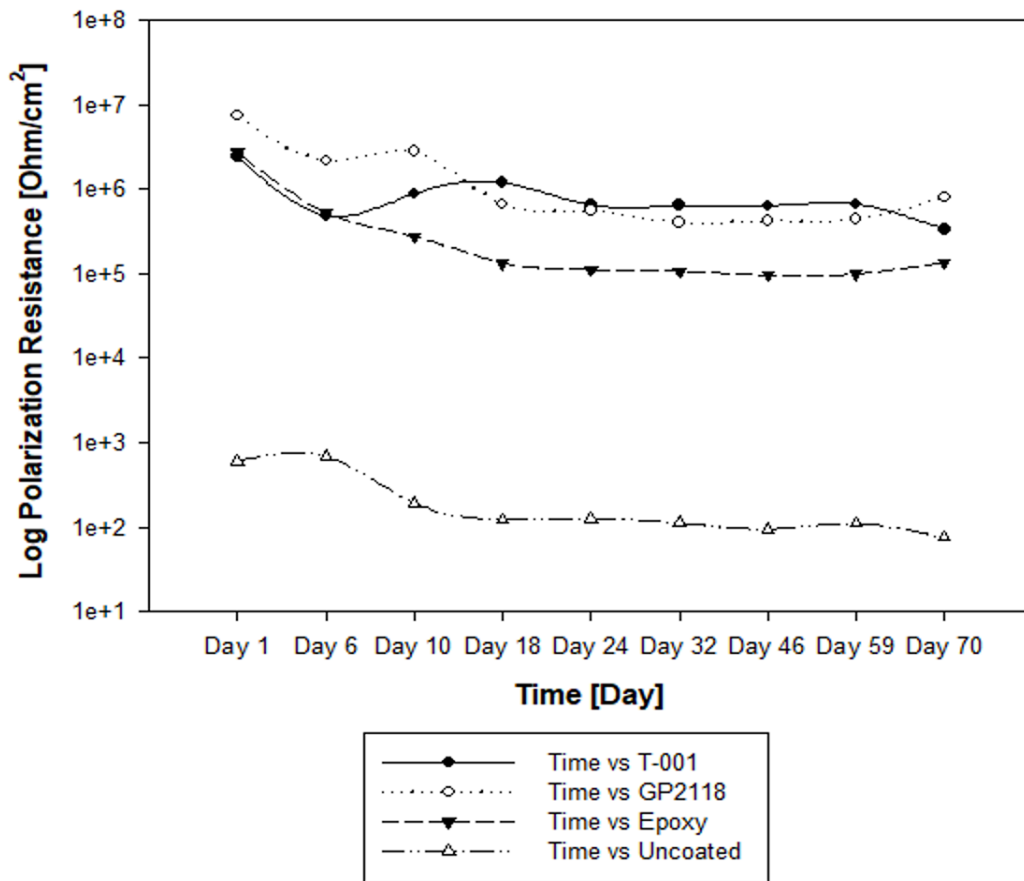


Figure 4.13 Linear Polarization Resistance for Ca(OH)<sub>2</sub> Solution.

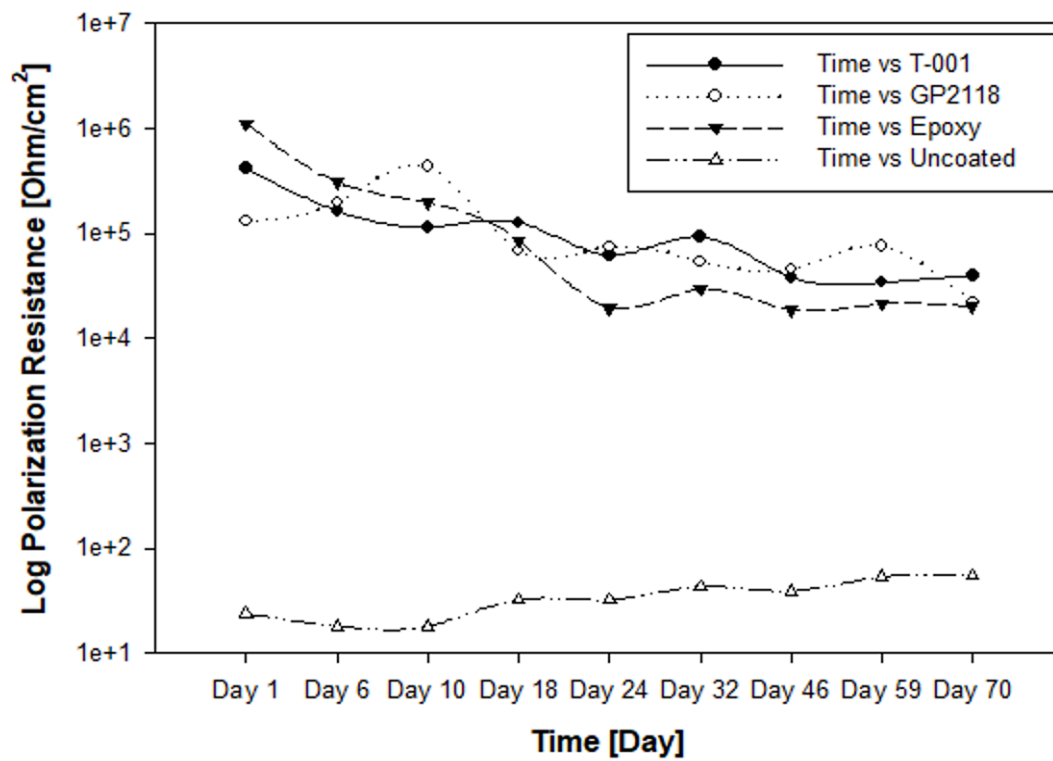
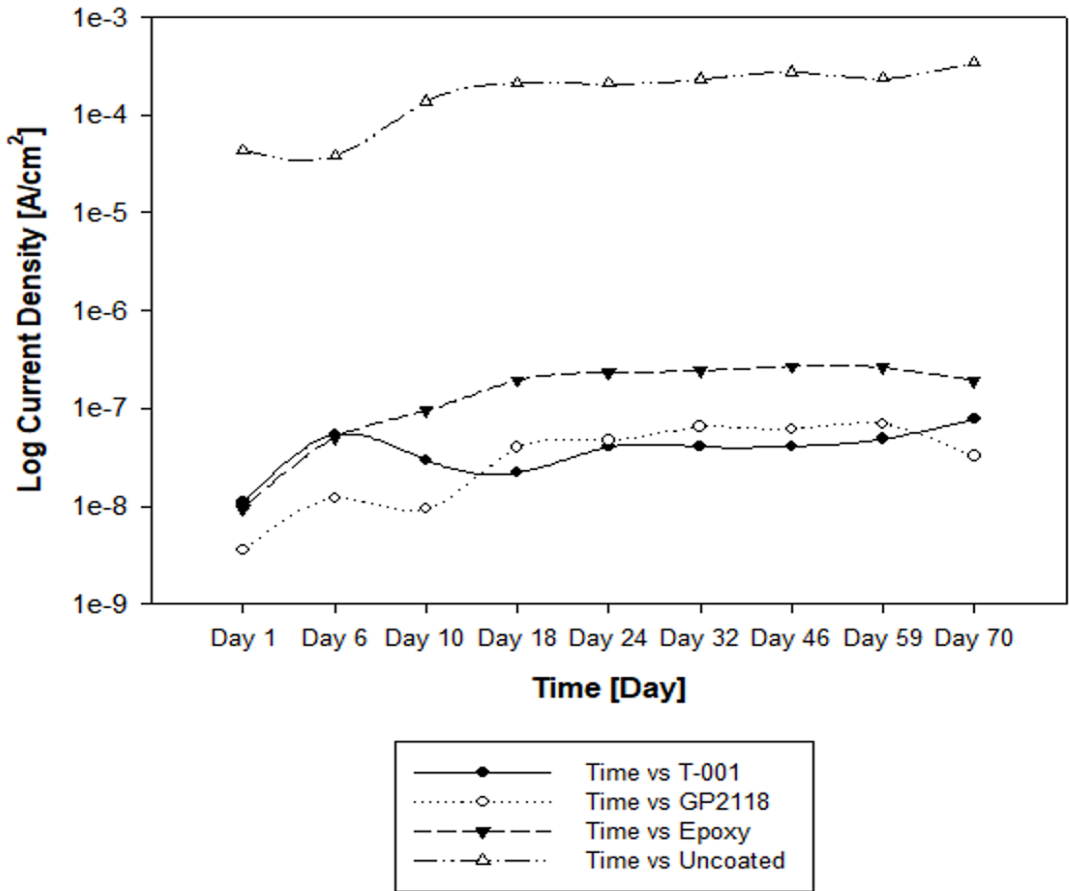
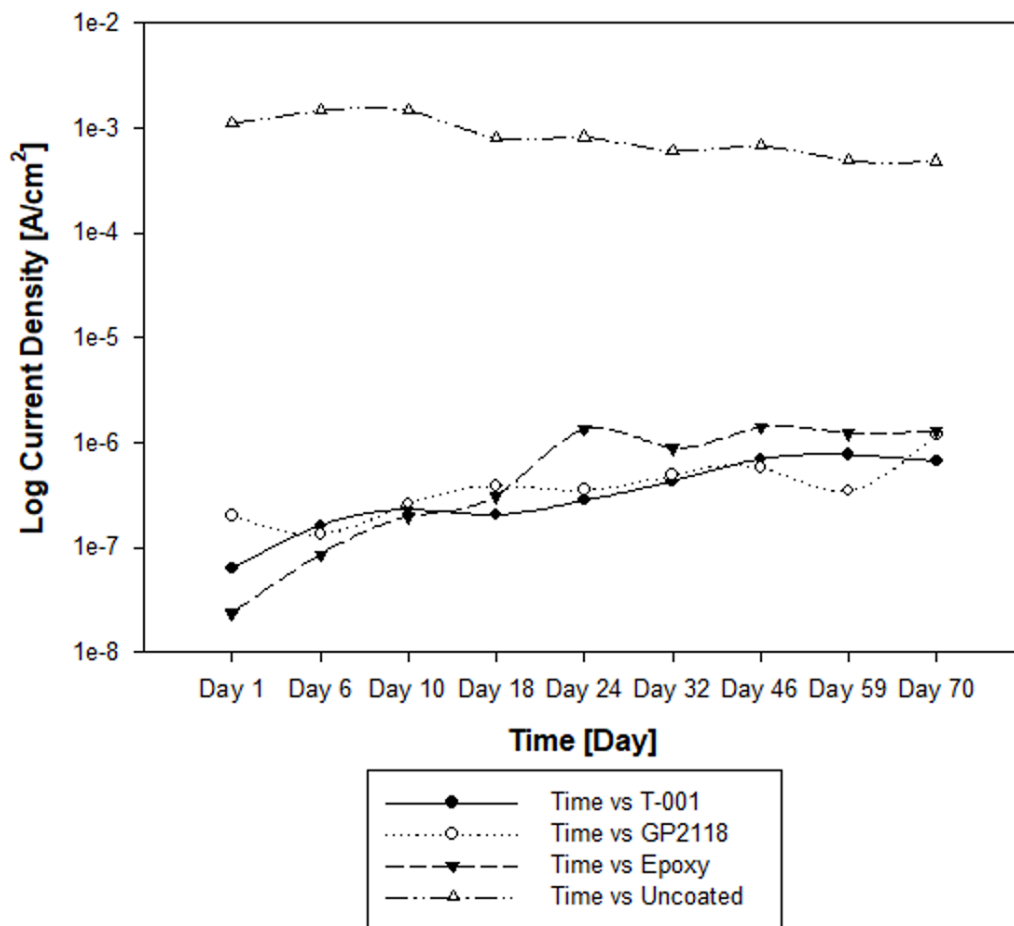


Figure 4.14 Linear Polarization Resistance for NaCl Solution.

*Corrosion Current Density ( $i_{corr}$ )*. The density of corrosion current is calculated using Equation (3.39), knowing the values of polarization resistance. Figures 4.15 and 4.16 show the trend of  $i_{corr}$  in 70 days of specimen monitoring. In Figure 4.15, the samples in  $\text{Ca}(\text{OH})_2$  solution present the same trend, because, in the first 20 days the penetration of electrolyte solution in the coating promotes the chemical reaction that forms a protective layer. After 20 days, the current density gets a constant profile because the oxides layer is completely adhesive to the surface of the rebars and avoid an increase of corrosion reaction rate. Comparing the coated with the uncoated values, it is observed a large gap of  $i_{corr}$ , therefore, the coated rebars have a better performance than uncoated ones. In particular, the slurry T-001 enamel coating has the least current density of  $6 \times 10^{-8} \text{ A/cm}^2$  so it provides the most effective behaviour. In addition the GP2118 powder coating has good protection because his  $i_{corr}$  curve is relatively close to the slurry one. On the contrary, the epoxy coating curve has approximately one order of magnitude of current density higher than the two enamel coatings. Figure 4.16 presents the result of the current density for the specimens immersed in the  $\text{NaCl}$  solution. The overall performance for coated samples has the same trend, in fact, they tend gradually to increase the current values. In specific, the growth is rapid in the first 20 days, but after that, there is a significant reduction, and the slope of the curves is considerably reduced. Furthermore, in the first 20 days, the epoxy coating has the least current density but due to the penetration of the electrolyte solution, there is a reverse of the trend and the enamel coating current density is dramatically lower than the epoxy one. Shortly, it is possible to conclude that the enamel coatings provide better protection than the traditional epoxy coating in both environments.



**Figure 4.15** Density of Corrosion Current in  $\text{Ca}(\text{OH})_2$  Solution.



**Figure 4.16** Density of Corrosion Current in NaCl Solution.

*Electrochemical Impedance Spectroscopy (EIS)*. Figure 4.17 to 4.20 present the EIS Bode diagrams for epoxy coated, enamel coated and uncoated samples after 70 days of immersion in a solution 3.5% wt of NaCl. The epoxy coated specimens, in Figure 4.17A, show a constant trend at low and medium frequency, but exceeding the frequency of  $10^3$  Hz, a rapid decrease of impedance's modulus  $|Z|$  occurs. The presence of the horizontal platform ensures that the coating is intact and continuous. In addition the curve's trend remains exactly the same and does not depend on time immersion, although, the platform at low frequencies tends to shift to lower values of  $|Z|$ . The coating provides protection to corrosion attack only when the impedance's modulus  $|Z|$  is higher than  $10^5 \Omega \cdot cm^2$ , therefore, after 46 days the epoxy coating partially loses its barrier's properties and electrochemical reactions start to be promoted [42]. Furthermore, as the days passed, the curves present an extension of the platform region, this means that the coating resistance is reducing, as a result of the increase of the coating capacitive. This behaviour is due to the penetration of the electrolytic solution through the epoxy coating. On the other hand, analysing the Bode diagram for epoxy coating where the phase angle is a function of frequency, Figure 4.17B, it is noticed that at low frequencies, the phase angle remains equal to zero until at  $10^2$  Hz the trend of the curves rises, and at high frequencies, it reaches  $-90^\circ$ . This is the typical trend that is provided from an intact coating as a validation of the previous result of Figure 4.17A. Moreover, it is observed that with the increasing of the days immersion the curves get to  $-90^\circ$  with a higher slope that causing a shift downward. The main reason for this displacement is related to the penetration of the NaCl solution through the coating.

Figure 4.18 and 4.19 show the EIS Bode diagrams for the enamel coatings T-001 and GP2118. In particular, focusing on the impedance's modulus  $|Z|$  - frequency  $f$  graphs, presented in Figure 4.18A and 4.19A, it is noted a similar curves trend. In both cases, the figures do not present horizontal platforms, but all curves decrease gradually at low and medium frequencies, due to the presence of coating damages. However, the impedance's modulus  $|Z|$  at low frequencies is around  $10^5 \Omega \cdot cm^2$ , so the coatings partially protect the substrate, although, there are some points in which the electrolyte solution penetrate through it, and corrosion reactions are promoted. Moreover, at the frequency of  $10^4$  Hz, there is a clear change of the slope of the curve and as time goes on, the curves shift toward lower impedance's modulus values. The same behaviour is observed also in epoxy coating's Bode diagram when the coating resistance decrease allowing the growth of coating capacitance, as a result of the solution's penetration through the coating. Regarding Figure 4.18B and 4.19B, they present the tendency of the phase angle as a function of frequency for the enamel coatings T-001 and GP2118. In both cases, the curves reach the value of  $-90^\circ$  at high frequencies, as a confirmation that the coating partially acts as a barrier against corrosion. Unfortunately, the curves have deep fluctuations at the range of medium frequencies, this is a sure sign that the coating is damaged and non-continuous. In specific, the enamel coating T-001, Figure 4.19B, shows more marked oscillation, therefore, the coating quality is lower than the powder coating, due to the greater presence of coating damages [43]. In these diagrams also, there is an increase in the slope of the curves to achieve  $-90^\circ$  with the time goes on, a similar trend was noticed in the same diagram for epoxy coating. Furthermore, as a comparison with the coated specimens, it is also tested the uncoated traditional rebar and the EIS Bode diagrams are presented in Figure 4.20. In specific, Figure 4.20A illustrates how impedance's modulus  $|Z|$  changes as a function of frequency and immersion time. The curves have an immediate decrease at low frequencies and assume a fairly constant value at medium and high frequencies. The starting value of  $|Z|$  at low frequencies is  $10 \Omega \cdot cm^2$ , an extremely lower value than  $10^5 \Omega \cdot cm^2$  presented in the previous Bode diagrams, therefore, the corrosion occurs freely. On the other hand, Figure 4.20B presents the trend of phase angle at the increase of frequency when the time goes on. All curves show negative phase angles at low frequencies around  $-60^\circ$  and with the increase of frequencies the trend of the curves moves to positive angles. This behaviour is dramatically different than the coated specimens, studied in Figure 4.17B, 4.18B and 4.19B, in fact, there is any coating deposited on the rebar surface to avoid corrosion mechanism.

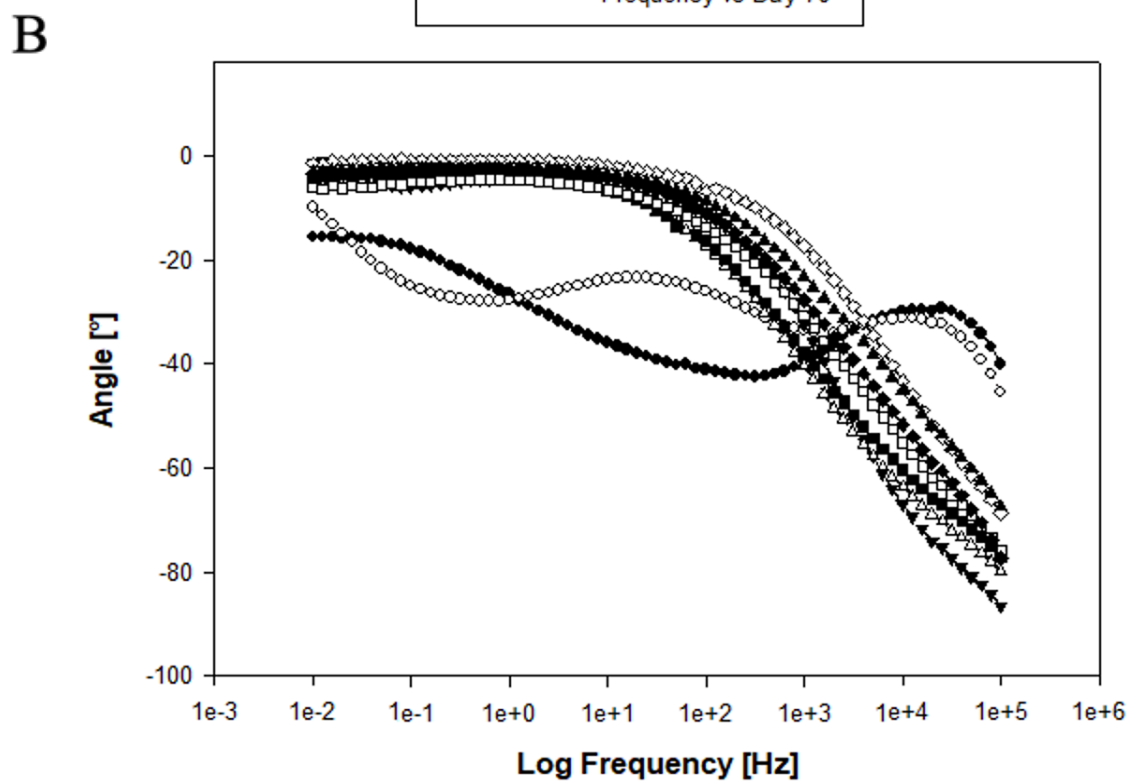
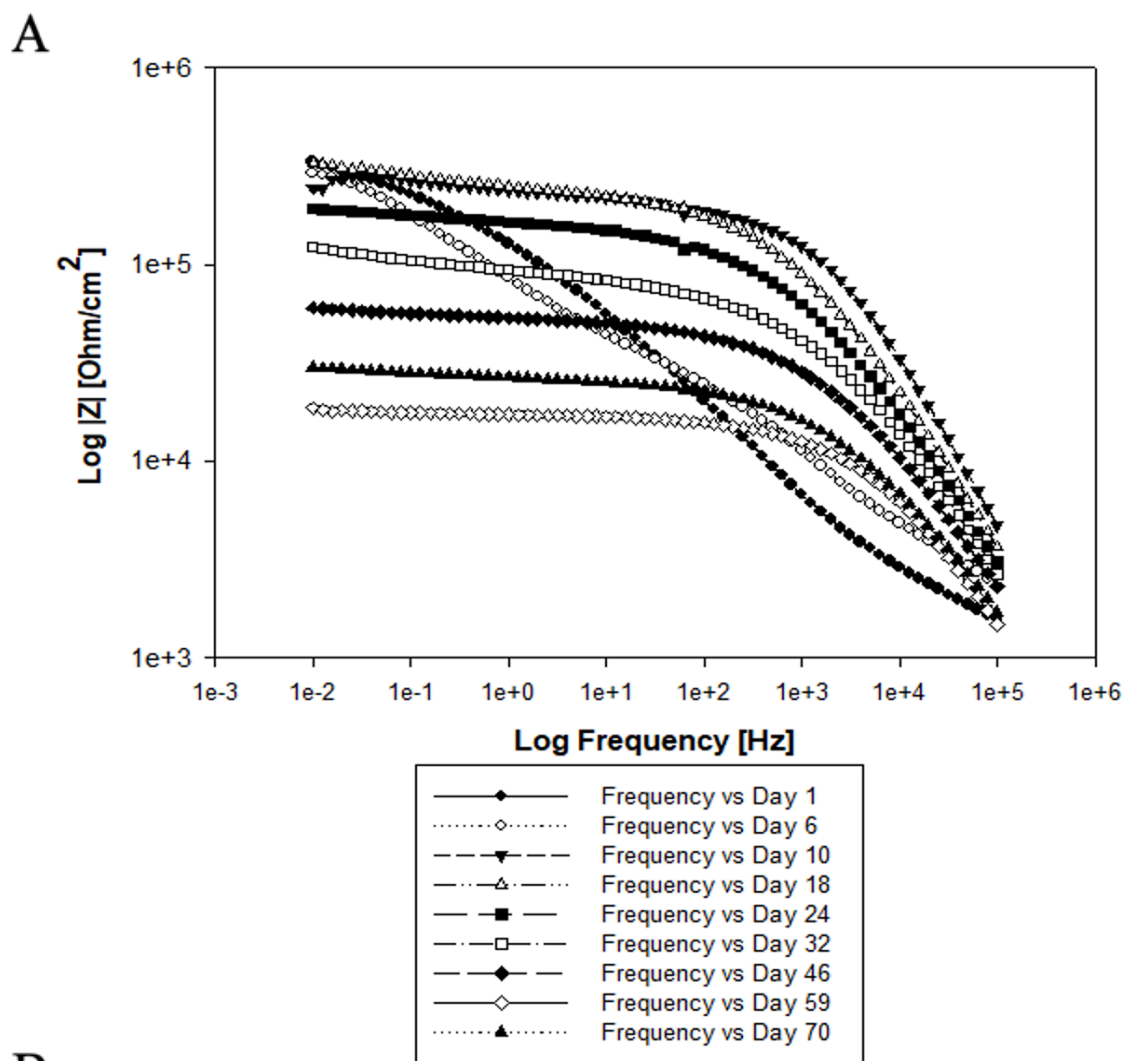


**Figure 4.17A and 4.17B** Bode Diagrams for Epoxy Coating Samples in NaCl Solution.

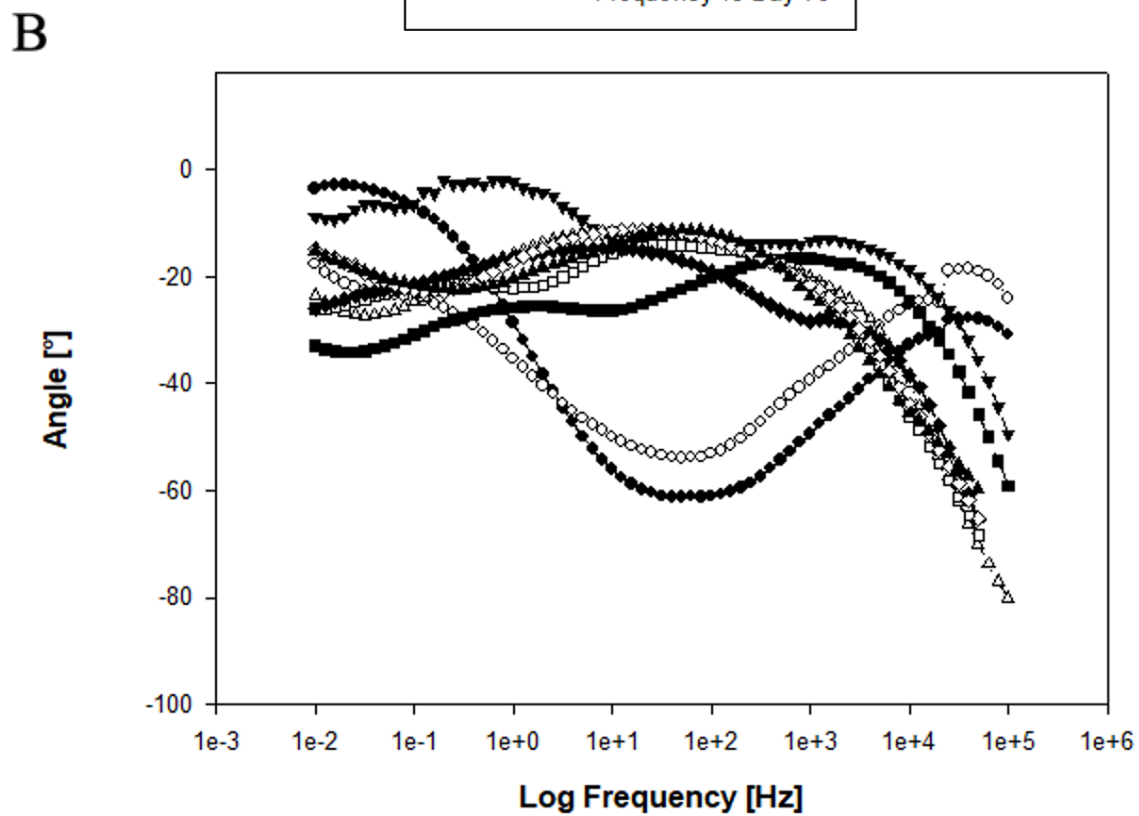
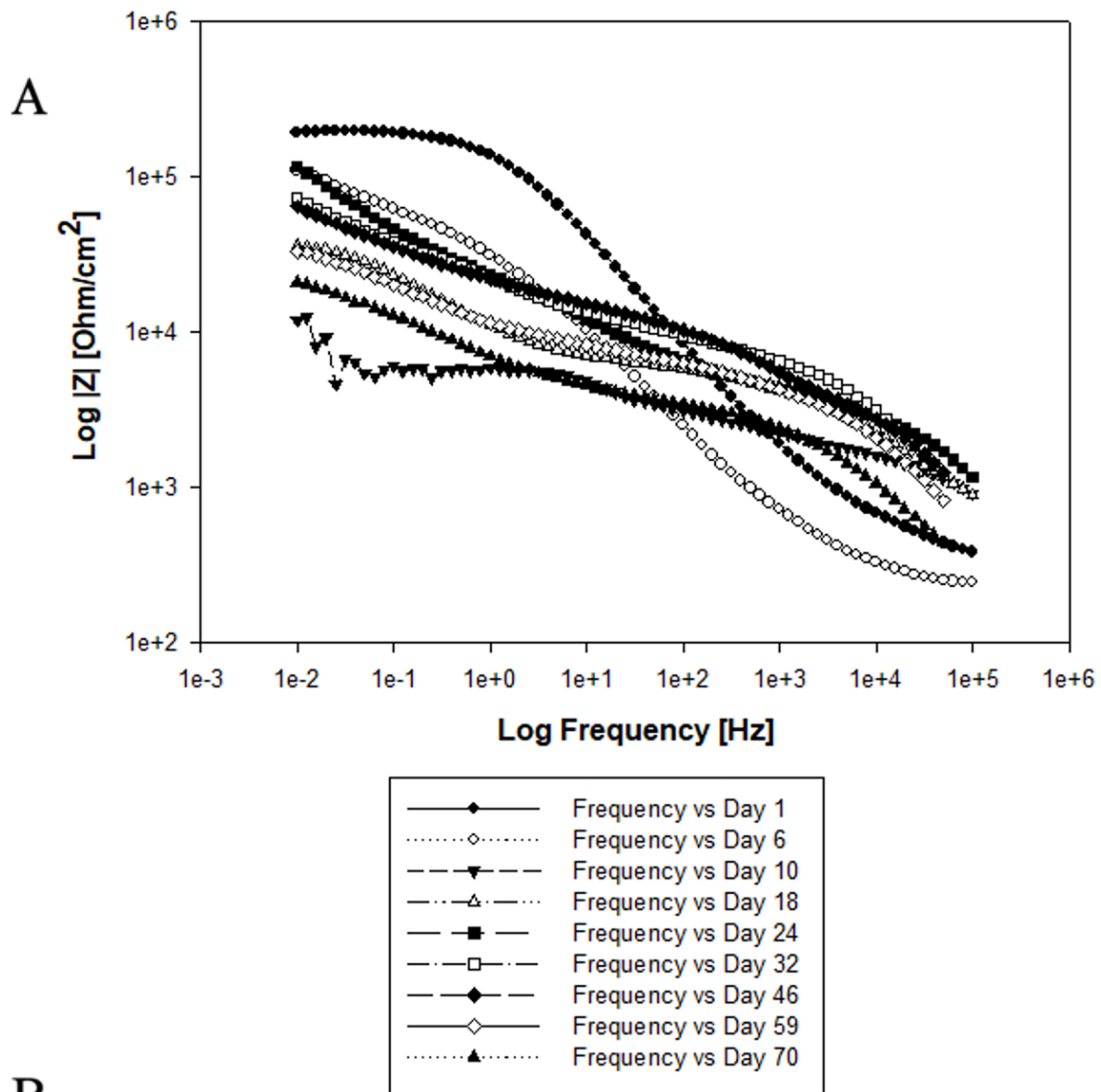


**Figure 4.18A and 4.18B** Bode Diagrams for GP2118 Powder Enamel Coating Samples in NaCl Solution.

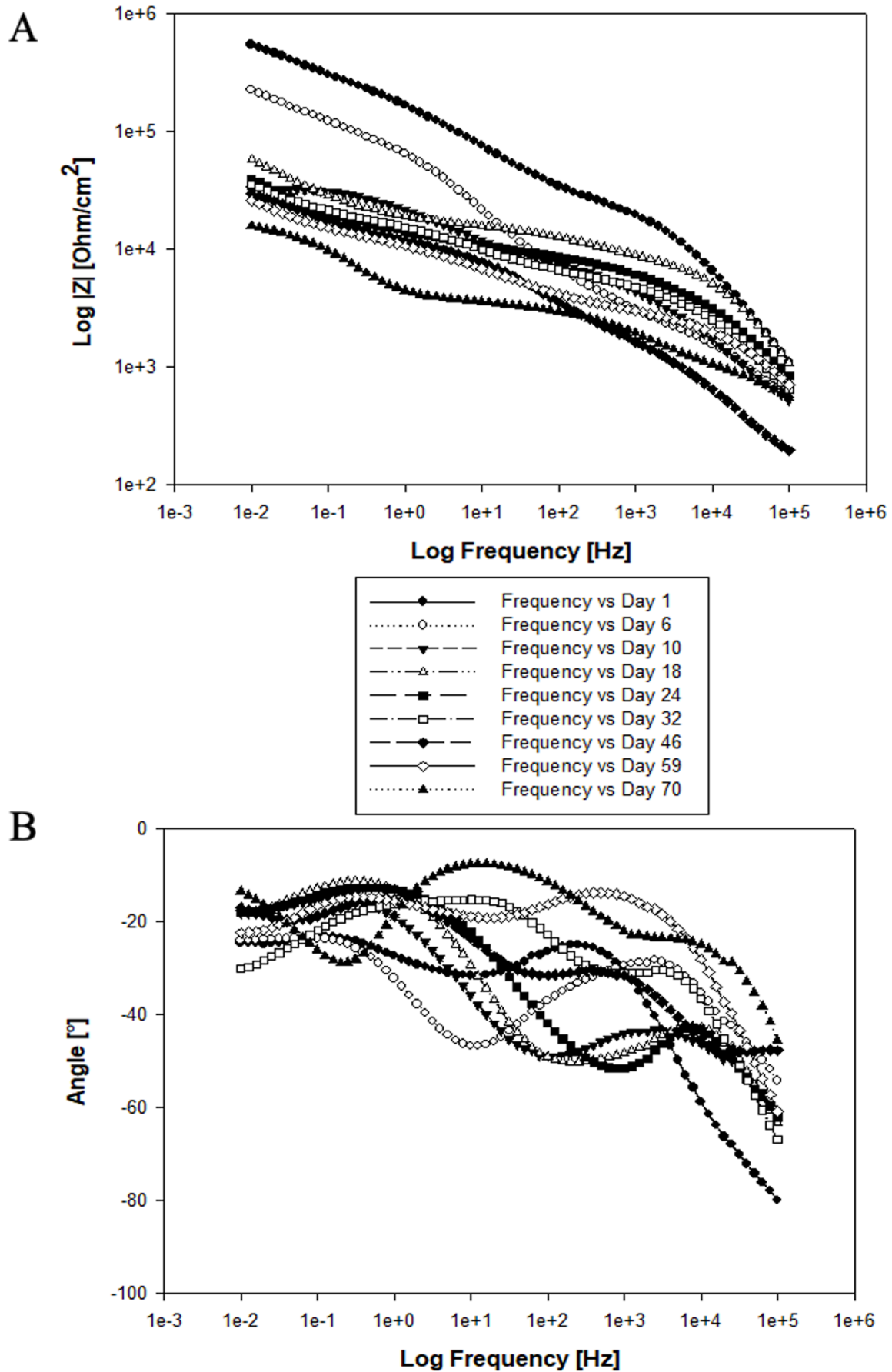


**Figure 4.19A and 4.19B** Bode Diagrams for T-001 Slurry Enamel Coating Samples in NaCl Solution.

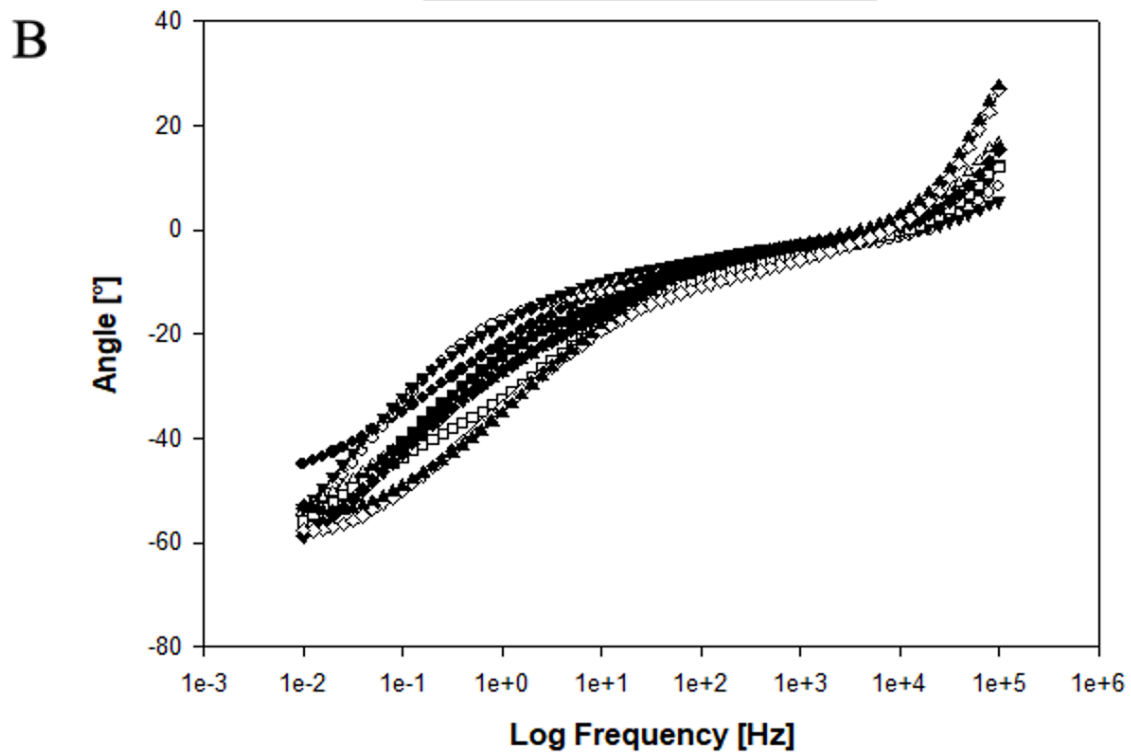
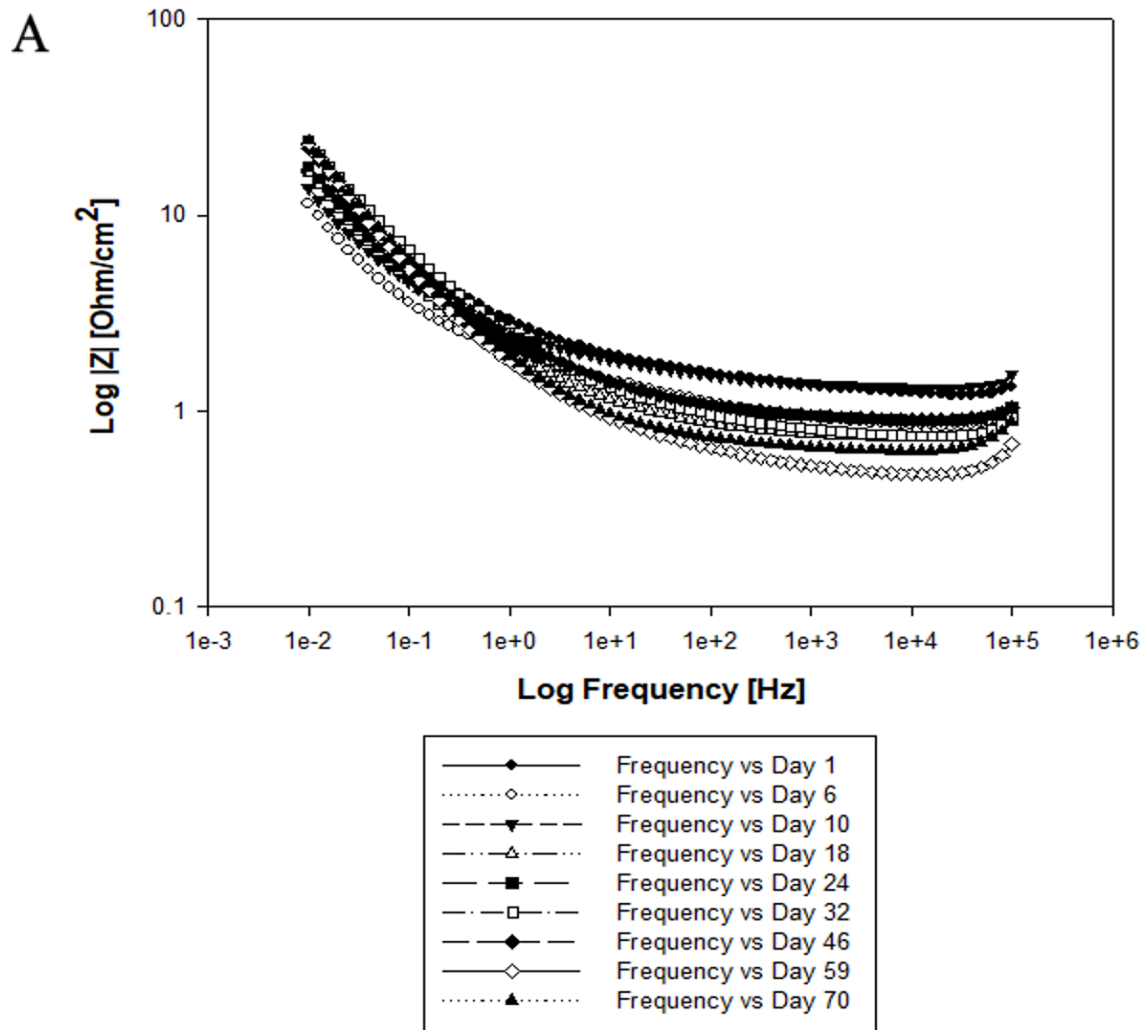


Figure 4.20A and 4.20B Bode Diagrams for Uncoated Coating Samples in NaCl Solution.

The following part presents the EIS results for the specimens immersed in the  $\text{Ca}(\text{OH})_2$  solution for 70 days, shown in Figure 4.21, 4.22, 4.23 and 4.24. In particular, Figure 4.21 shows the EIS Bode diagrams for the epoxy coated samples, where Figure 4.21A illustrates the impedance's modulus as a function of frequency. The curves trend has a similar shape than the curves in NaCl solution in Figure 4.17A, in fact, at low and medium frequencies there is a plateau at the value of  $10^5 \Omega \cdot \text{cm}^2$ , therefore, the coating is intact and provide good protection against corrosion. Furthermore, it is noticed that the impedance's modulus shifts forward lower values only in the first 10 days, after that, the curves present the same trend. This behaviour is related to the formation of the samples surface a passive layer that avoids the propagation of corrosion reactions. Moreover, the platform does not tend to extend with the time goes on, but it appears constant, this means that the coating resistance is not subjected to a significant reduction. Focusing on the Bode diagram that shows the trend of the phase angle as a function of frequency in Figure 4.21B, it is evident that all curves assume angles around  $0^\circ$  at low and medium frequencies but there is a rapid growth to  $-90^\circ$  at high frequencies values. As a result, this is a confirm of the high quality and homogeneity of the epoxy coating.

Figure 4.22 and 4.23 present the EIS Bode diagrams for the enamel coating specimens that remain in  $\text{Ca}(\text{OH})_2$  solution for 70 days. Specifically, Figure 4.22A and 4.23A, show for all the testing periods a similar trend; in the first 18 days the curves have a higher slope at low and medium frequencies, but after that, there is a significant reduction of these values. The curves tend to take a partially horizontal trend, that reminds the platform shape, analysed before in Figure 4.21A. This trend is due to the formation of a passive layer on the sample's surface. In the beginning, the enamel coatings present surface damages, but thanks to the chemical reactions, that occur at the contact with the electrolyte solution, the failure points are gradually covered by a protective oxides layer. Therefore, the corrosion reactions reduce their rate and the curves show a platform shape at low and medium frequencies. In addition all curves present at low frequencies an impedance's modulus  $|Z|$  around  $10^6 - 10^7 \Omega \cdot \text{cm}^2$ , then, the specimen's surfaces are completely protected. The previous results can be confirmed by the phase angle Bode diagrams, shown in Figure 4.22B and 4.23B. Overall, the curves have the phase angle equal to  $0^\circ$  at low frequencies, but when the frequency increase, there is a rapid growth until  $-90^\circ$  at high frequencies. Surely, the coatings provide good protection after the 18 days because there is no fluctuation of the curves in the medium frequency region, on the contrary, these oscillations are quite pronounced in the first 18 days owing to the presence of holes or pinholes on the coatings.

Ultimately, the EIS Bode diagrams for uncoated samples are shown in Figure 4.24 after 70 days of immersion in  $\text{Ca}(\text{OH})_2$  solution. In particular, Figure 4.24A presents the variation of impedance's modulus as a function of frequency and time. The curves show in the first 10 days a decreasing trend, but after that time, the curves reduce their slope and take a horizontal trend around  $10^2 \Omega \cdot \text{cm}^2$ . There is no reduction of  $|Z|$  also at high frequencies, therefore, the corrosion is not promoted in this environment due to the formation of a passive layer, that avoid the corrosion to goes on. Naturally, this kind of protection has a different nature and thickness than epoxy or enamel coating, which is directly deposited on the surface. It makes sense that the impedance's modulus  $|Z|$  is quite lower compared to epoxy or enamel coating because these materials are insulating so they do not promote the passage of current. On the contrary, the passive layer, which is produced from the reaction of the surface with the electrolyte solution, is made primarily from an oxides layer, which has a limited thickness but it is strongly adherent to the surface so it is able to provide higher protection. Moreover, to validate the results obtained from the previous Bode diagram, it is possible to make a comparison with Figure 4.24B, where the phase angle is presented as a function of frequency. In the first 18 days, the curves decrease

gradually at low frequencies from  $-50^\circ$  to  $-20^\circ$ , but after that, the curves remain stable at  $-20^\circ$ , as a result of the formation of the passive layer. All curves have a decreasing trend, at  $10^3 \Omega \cdot \text{cm}^2$  where there is a minimum point at  $0^\circ$ , followed by a dramatically increasing to the negative values. This behaviour is different than the enamel coating Bode diagram, in fact, the curves never move to positive angles as in Figure 4.20B so the corrosion processes do not occur. Furthermore, there is no fluctuation, as a clear sign that the passive layer is uniform and continuous on the rebar surface.

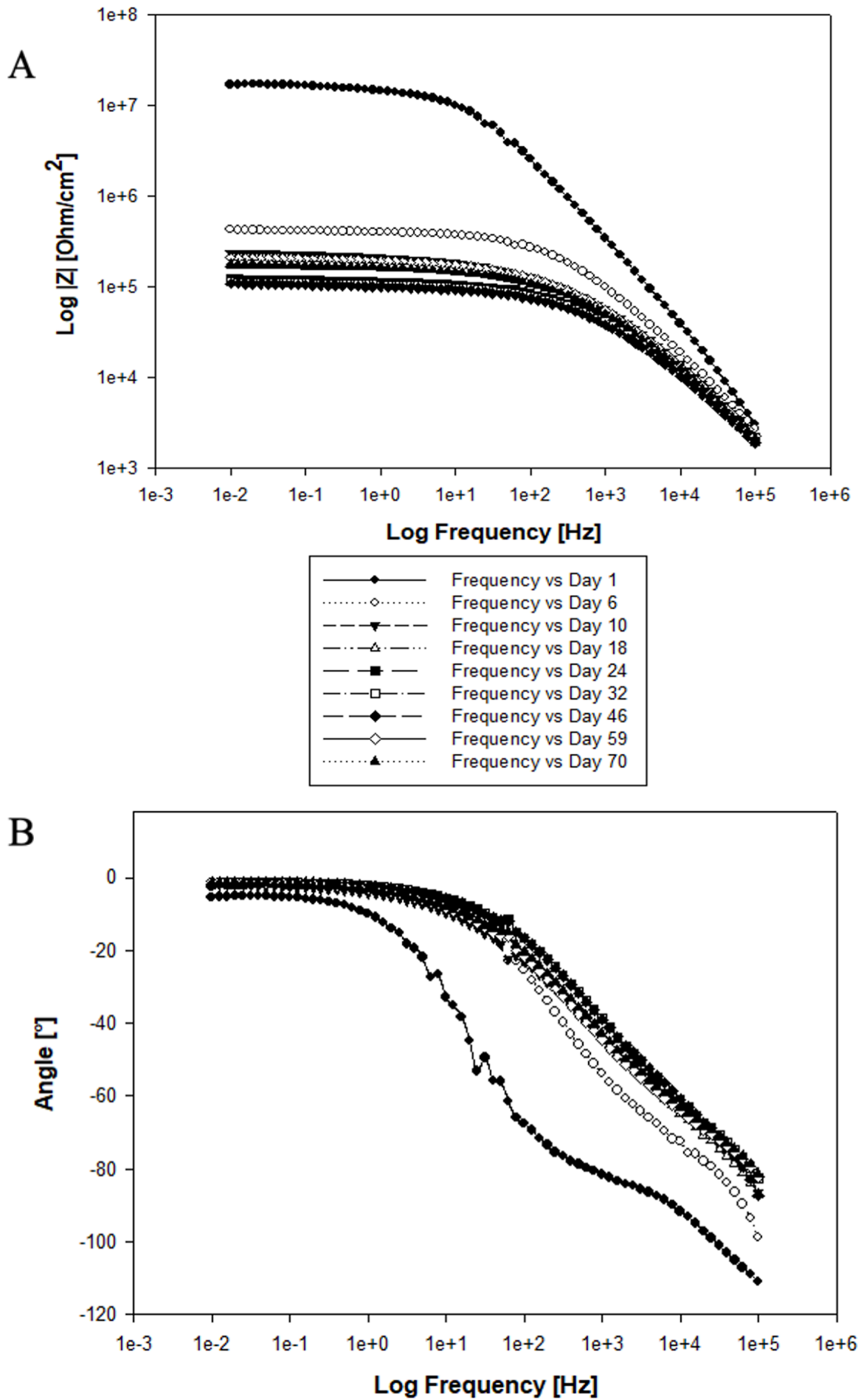
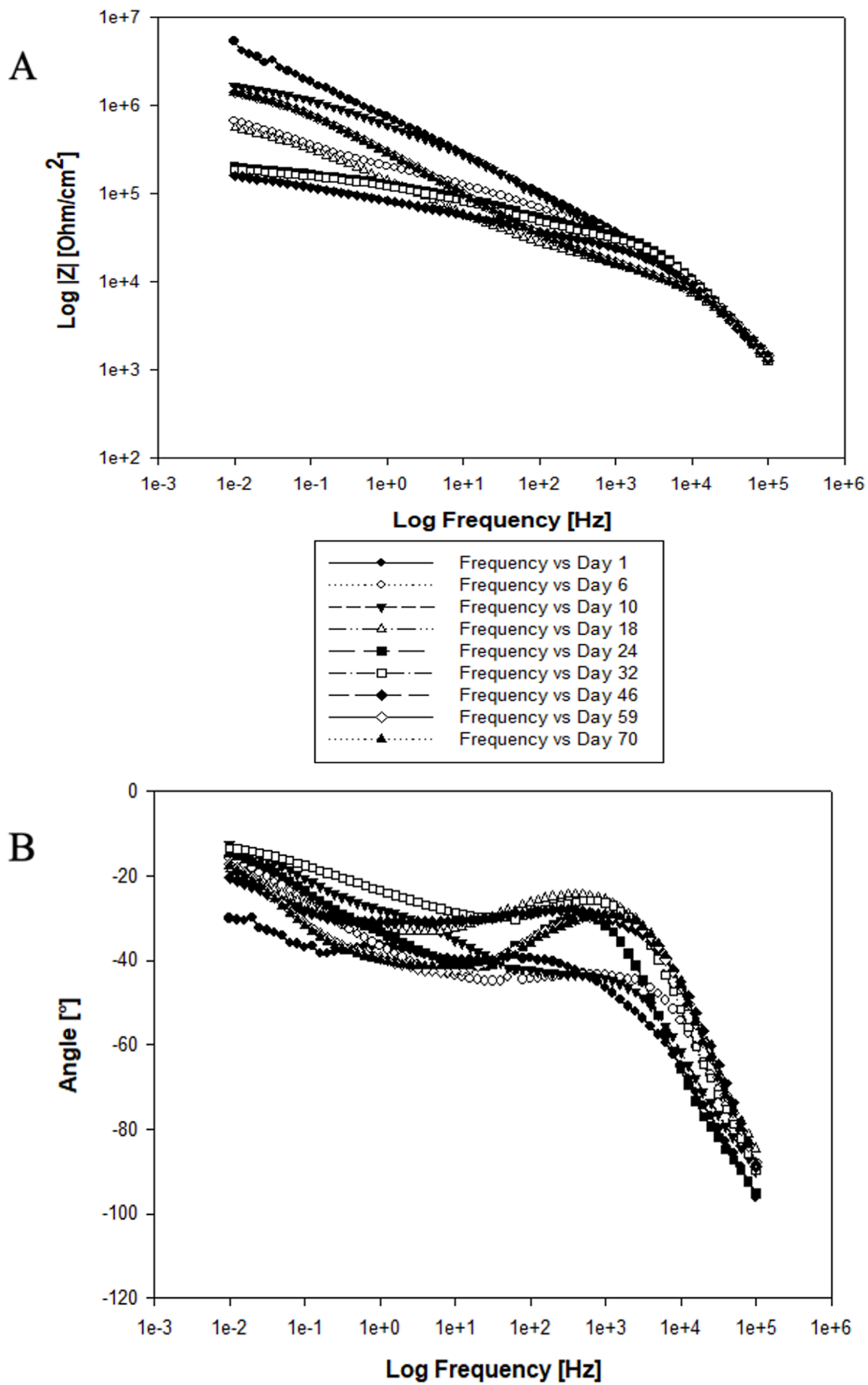
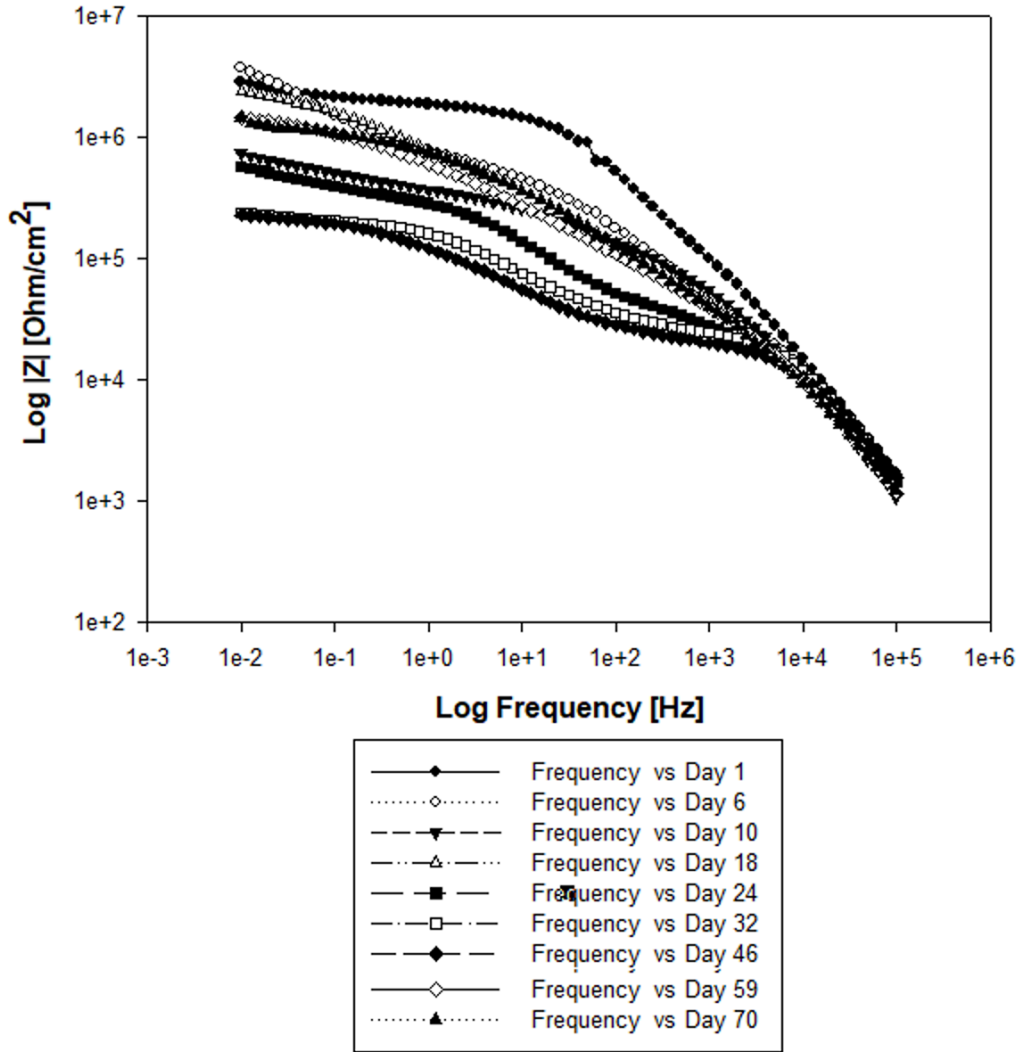


Figure 4.21A and 4.21B Bode Diagrams for Epoxy Coating Samples in  $\text{Ca}(\text{OH})_2$  Solution.



A



B

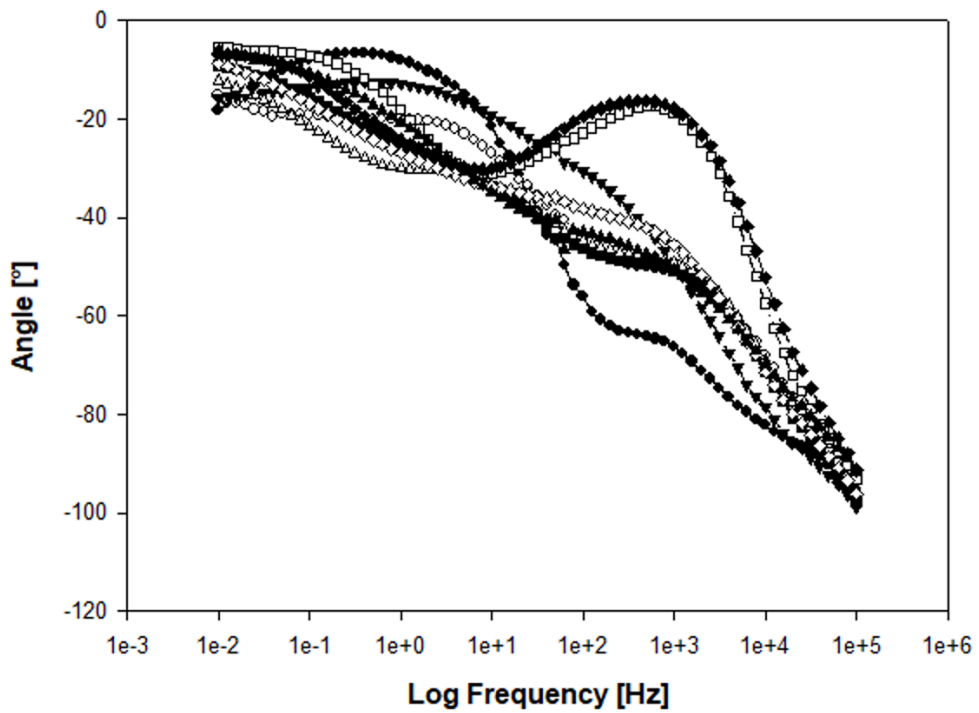


Figure 4.23A and 4.23B Bode Diagrams for T-001 Slurry Enamel Coating Samples in  $\text{Ca(OH)}_2$  Solution.

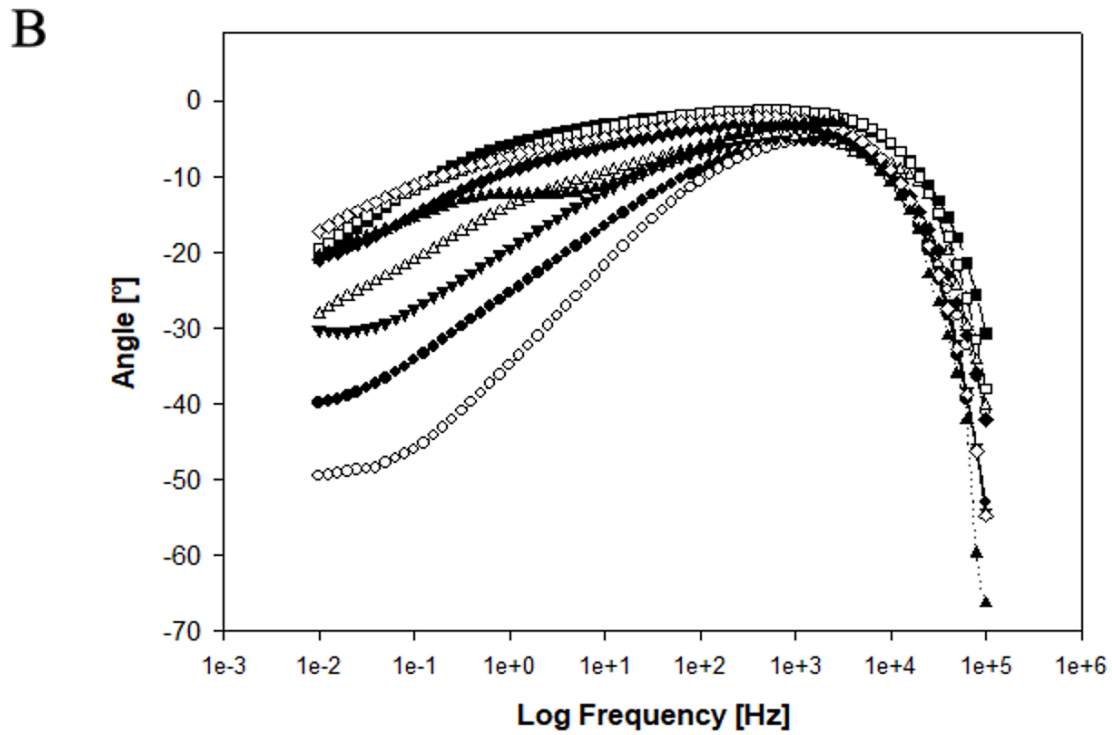
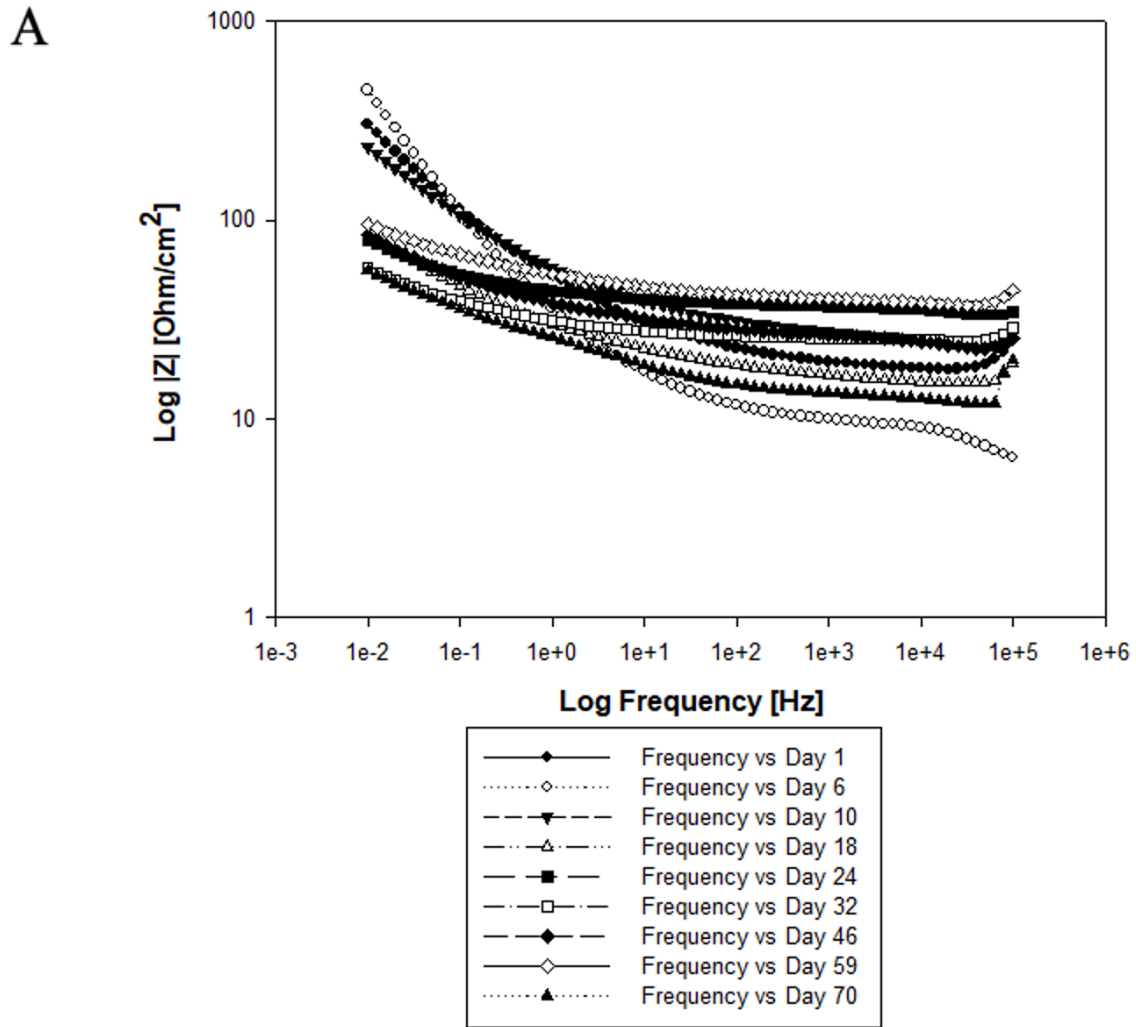


Figure 4.24A and 4.24B Bode Diagrams for Uncoated Coating Samples in  $\text{Ca}(\text{OH})_2$  Solution.

*Equivalent Electric Circuit (EEC)*. The real systems show complex behaviour that could be quite hard to fully understand. For this reason, to facilitate the analysis is commonly referred to a theoretical circuit that retains all of the electrical characteristics of a given system. In this specific case are been identified two different equivalent circuits, presented in Figure 3.19. The A circuit describes the system behavior in the first 18 days instead the B circuit is used for all the remain days. The main difference between these two is the presence of a Warburg impedance that takes into consideration the diffusion behavior due to the accumulation of the corrosion products in the active sites. Figure 4.25 and 4.26 present the changing trend of coating resistance  $R_c$ , coating capacitance  $C_c$ , charge transfer resistance  $R_{ct}$  and double layer capacitance  $C_{dl}$  for coated specimens immersed in  $\text{Ca}(\text{OH})_2$  solution for 70 days. The coating resistance determines the quality of the coating as a barrier against electrolyte solution penetration which is directly related to the coating microstructure, such as the presence of holes or pinholes. On the contrary, the coating capacitance measures the diffusion of the solution through the coating, and it depends on the dielectric properties, microstructures, and coating thickness. As described in Figure 4.25, the epoxy and T-001 slurry coatings present a downward trend, marked in the first 20 days, followed by an almost constant trend. Moreover, the epoxy coating has a coating resistance around  $10^5 \Omega/\text{cm}^2$  instead the T-001 slurry enamel coating shows a lower value around  $2.5 \cdot 10^4 \Omega/\text{cm}^2$ . On the other hand, the GP2118 powder enamel coating immediately has a stable horizontal trend at  $10^4 \Omega/\text{cm}^2$ . As a result, the epoxy coating provides the highest resistance compared to the enamels. Regarding the coating capacitance, it is observed an upward trend in correspondence to the decrease of the coating resistance for epoxy and T-001 slurry coating. At the first moment, the curves tend to rise, but secondly, they go to the asymptotic value of  $10^{-8} \text{ F}/\text{cm}^2$ .

Afterward, Figure 4.27 and 4.28 show the steel/solution interfacial properties for epoxy and enamel coated samples, in specific, the charge transfer resistance  $R_{ct}$  and the double layer capacitance  $C_{dl}$  are analysed. The charge transfer resistance measures the performance of the electrons to be transferred across the surface and it is directly proportional to the corrosion current  $i_{\text{corr}}$ . Overall, Figure 4.27 shows for epoxy and enamel coated samples a rapidly decrease with the immersion time, in particular, the epoxy coating presents the lowest value of resistance, that is significantly smaller than the enamel coatings, in fact, these specimens show a charge transfer resistance of  $10^6 \Omega/\text{cm}^2$ , which is two orders of magnitude higher than the epoxy coated samples. After that, the double layer capacitance curves are analysed in Figure 4.28, in specific, all curves have an upward trend, even if the epoxy curve presents the lower value in the first 18 days, but after a rapid rising, it shows a stable asymptotic value to  $10^{-4} \text{ F}/\text{cm}^2$ , that is higher than the T-001 and GP2118 enamel coatings.

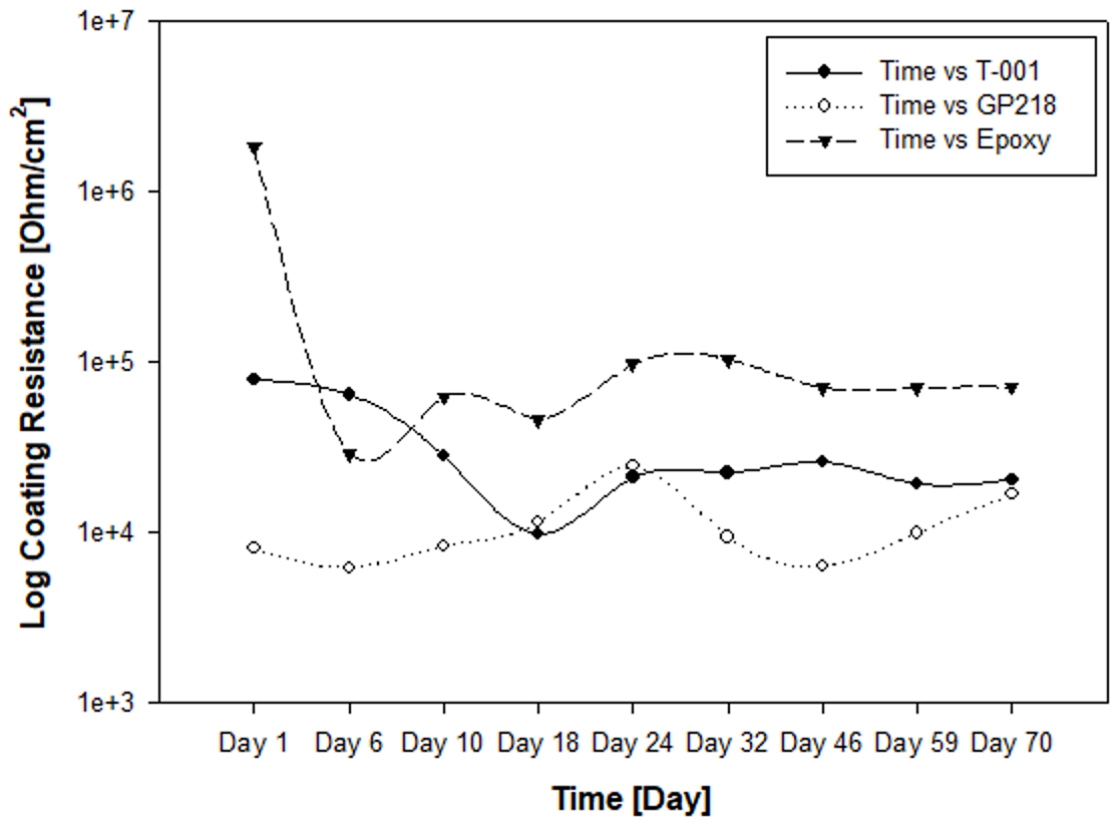


Figure 4.25 Coating Resistance in Ca(OH)<sub>2</sub> Solution.

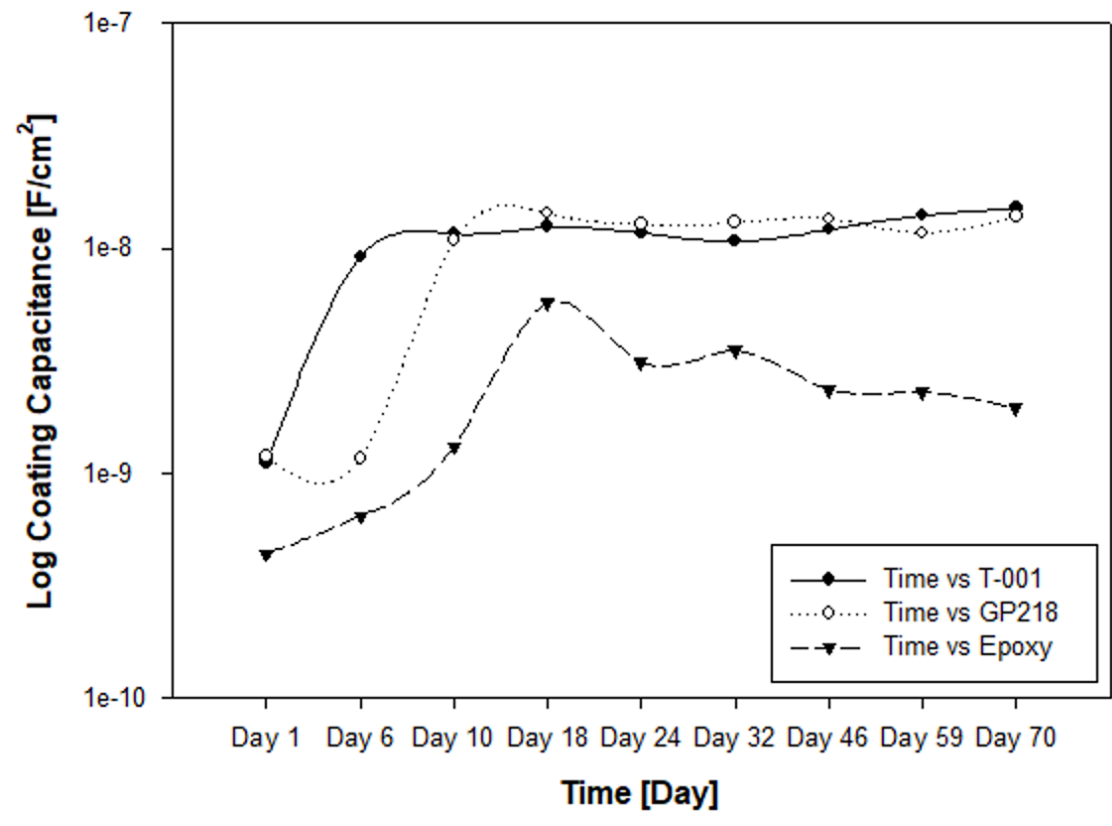


Figure 4.26 Coating Capacitance in Ca(OH)<sub>2</sub> Solution.

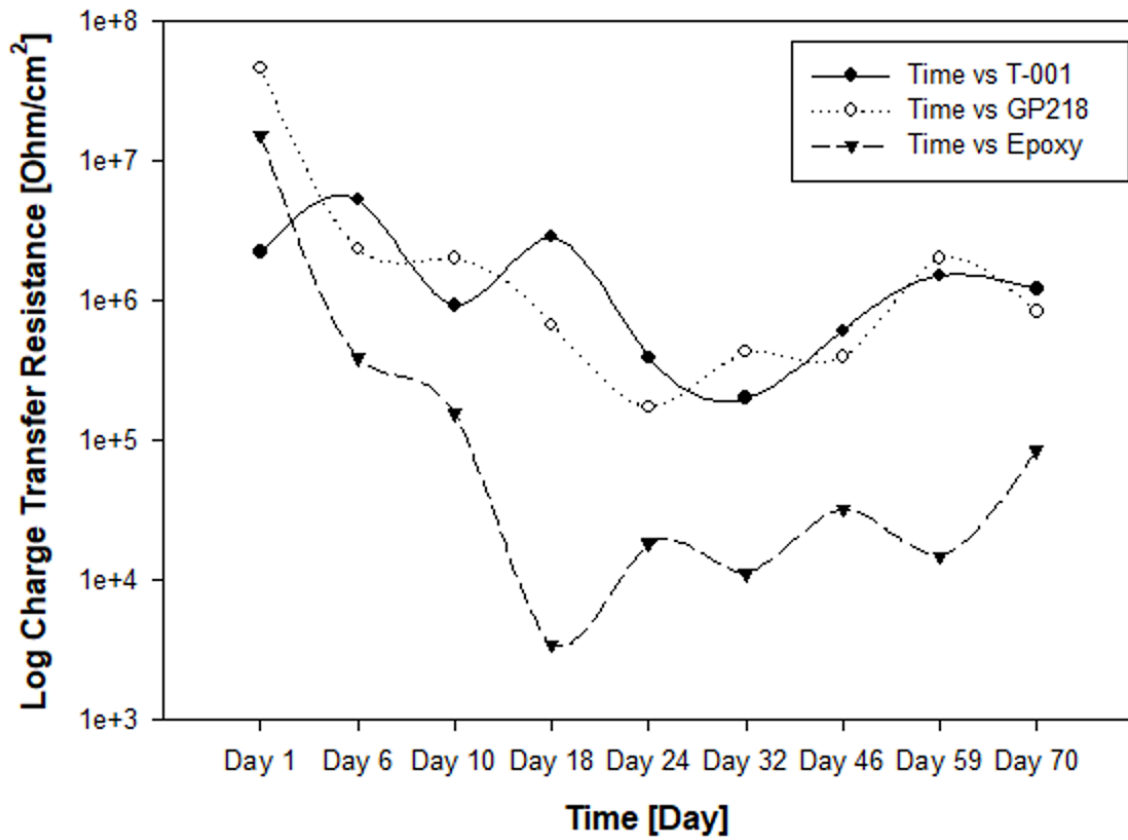


Figure 4.27 Charge Transfer Resistance in Ca(OH)<sub>2</sub> Solution.

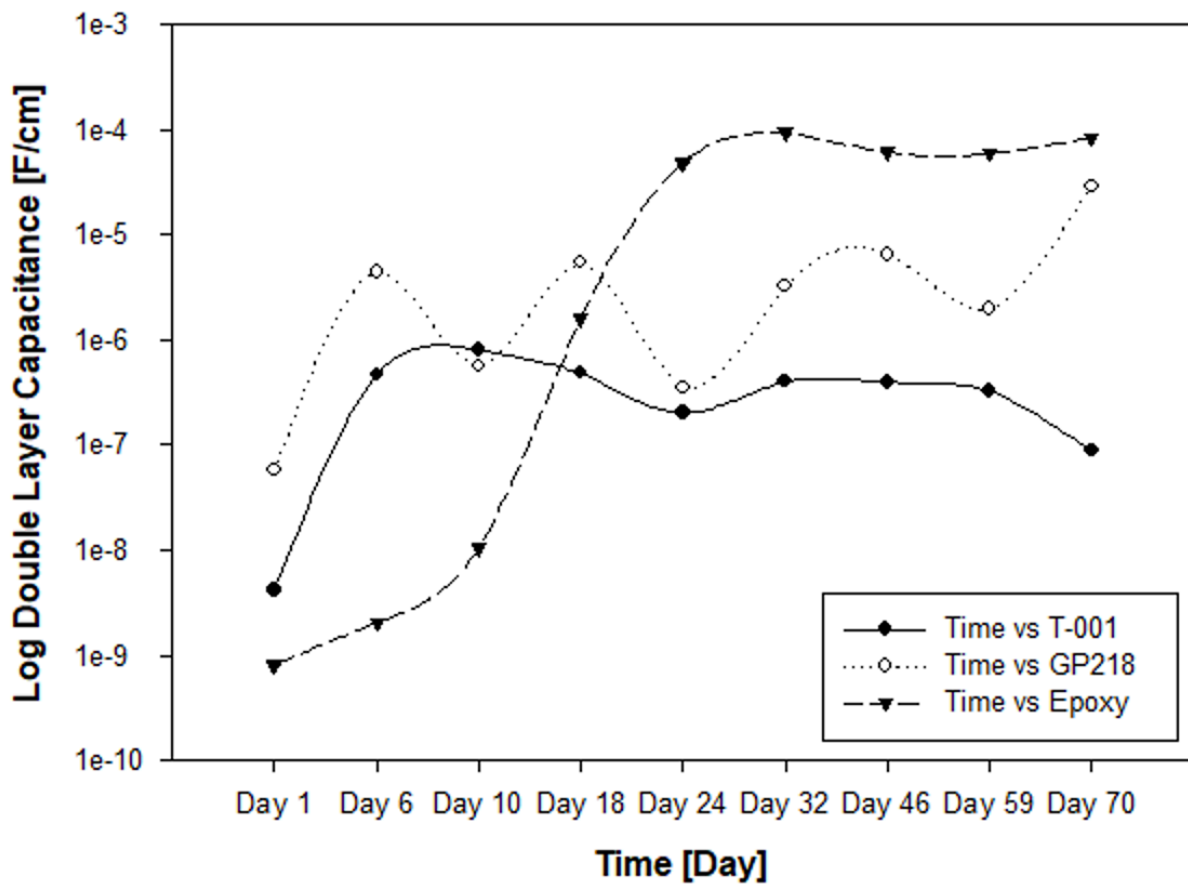


Figure 4.28 Coating Resistance in NaCl Solution.

In the later part are illustrated the EEC results for the coated specimens that are dipped in NaCl solution for 70 days. Figure 4.29 shows the trend of the coating resistance as a function of time, all the curves tend to decrease gradually. The T-001 slurry and the GP2118 powder coatings have a similar trend and it is measured a resistance value around  $5 \cdot 10^3 \Omega/cm^2$  after 50 days of immersion. On the other hand, the epoxy coating presents a mild inclination at the beginning of the test, but after that, the curve is stabilized at a constant profile at  $2.5 \cdot 10^4 \Omega/cm^2$ . Analysing Figure 4.30, the coating capacitance shows completely the opposite behaviour, the curves rapidly rise. The epoxy coating shows the smallest values of capacitance during all 70 days, instead, the enamel specimens present a capacitance value of one order of magnitude higher than the epoxy-coated steel. As mentioned before, the coating resistance and capacitance are directly related, in fact, the reduction of the resistance induces an increase of the capacitance due to the penetration of the electrolyte solution across the coating. Looking at Figure 4.31, it describes the trend of the charge transfer resistance as a function of the time in epoxy and enamel coated samples. Overall, the curves have a downward trend where the epoxy coated curve shows the higher resistance for the first 30 days, but after that, there is a reversal of the trend and the enamel specimens obtain greater values than the epoxy coating. Finally, the double layer capacitance trend for epoxy and enamel coating is described in Figure 4.32. The figure clearly shows a reverse of the trend between the 30<sup>th</sup> day and the 40<sup>th</sup> day, in fact, in the first period the epoxy sample has a lower value than the enamel specimens, but once passed the 40<sup>th</sup> day, the smallest values of capacitance are associated with the T-001 slurry and GP2118 powder rebars.

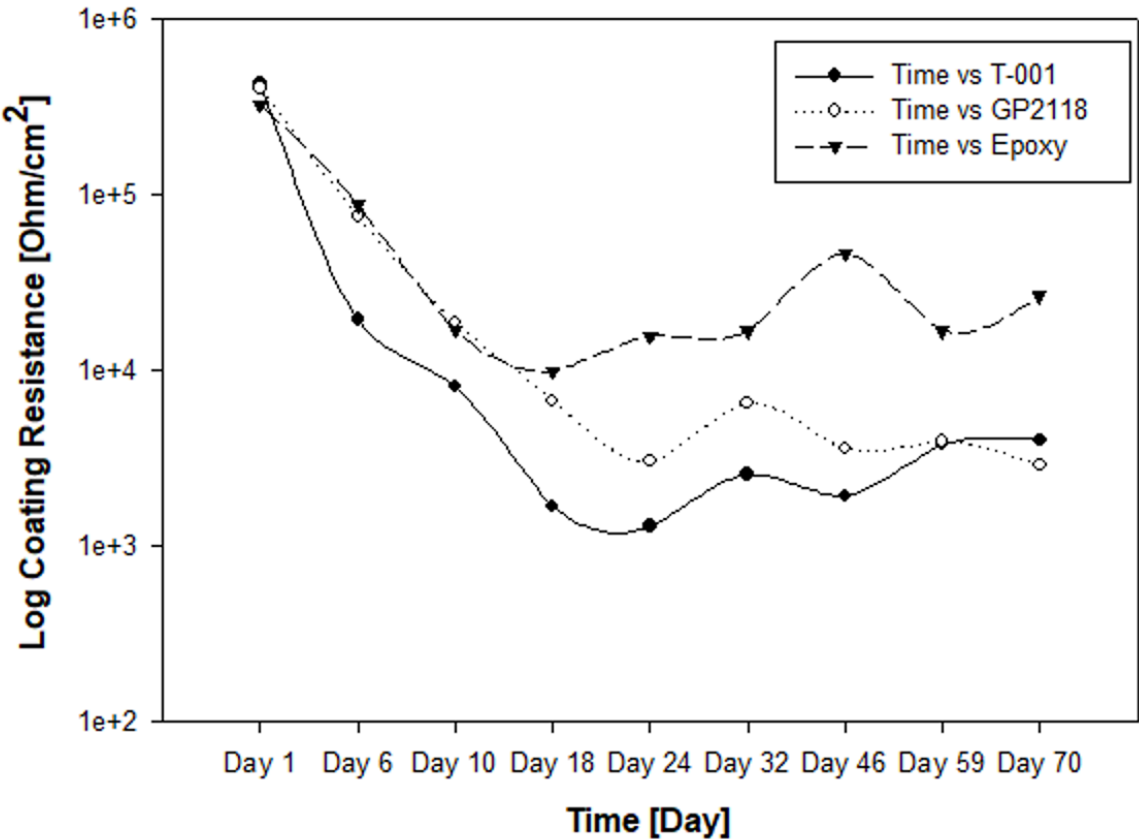


Figure 4.29 Coating Resistance in NaCl Solution.

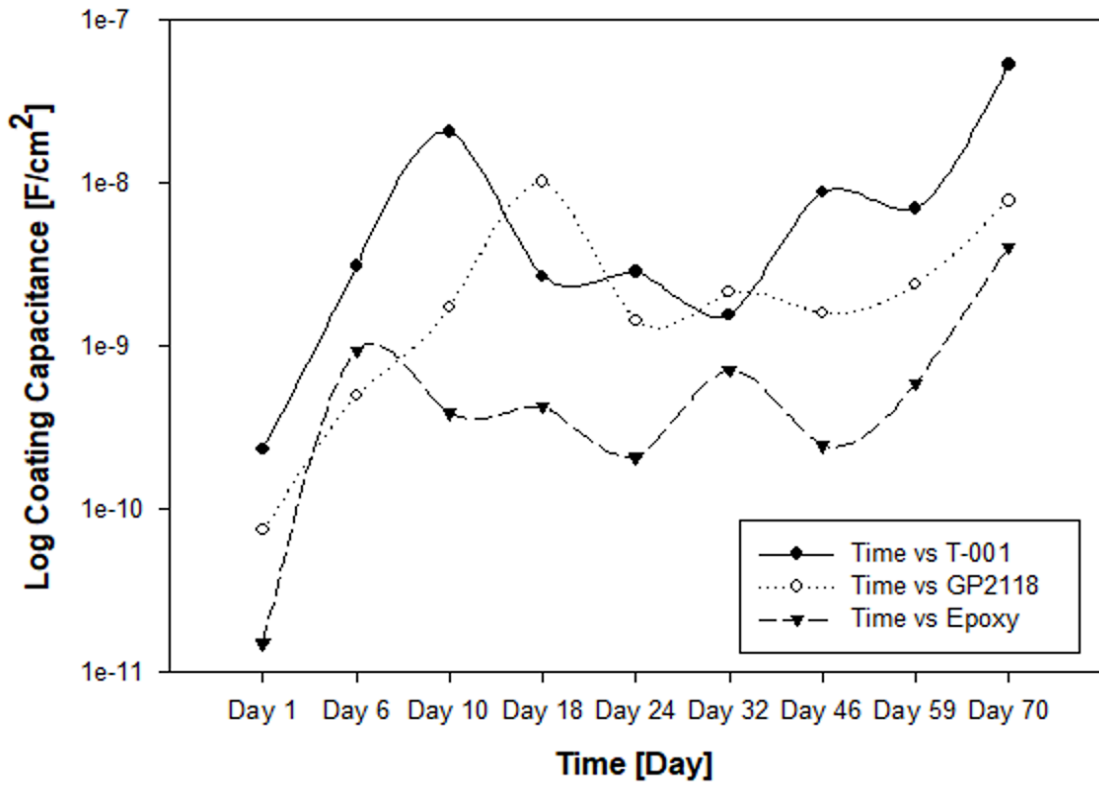


Figure 4.30 Coating Capacitance in NaCl Solution.

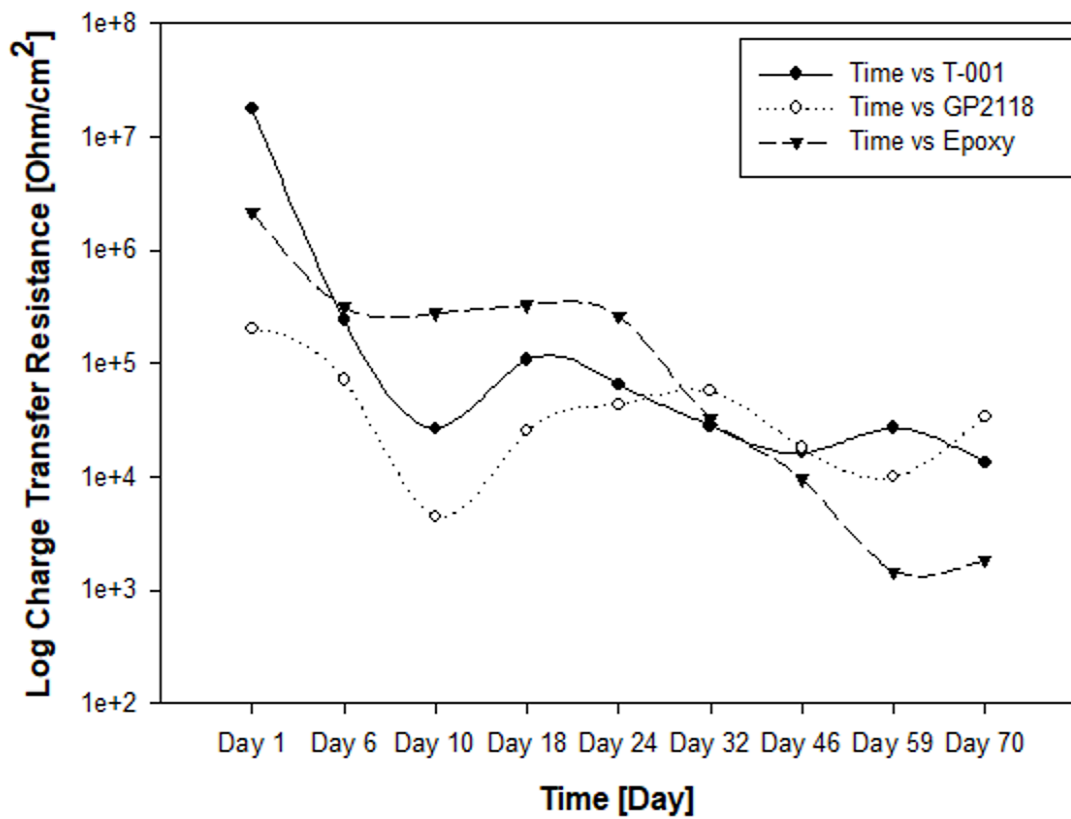


Figure 4.31 Charge Transfer Resistance in NaCl Solution.

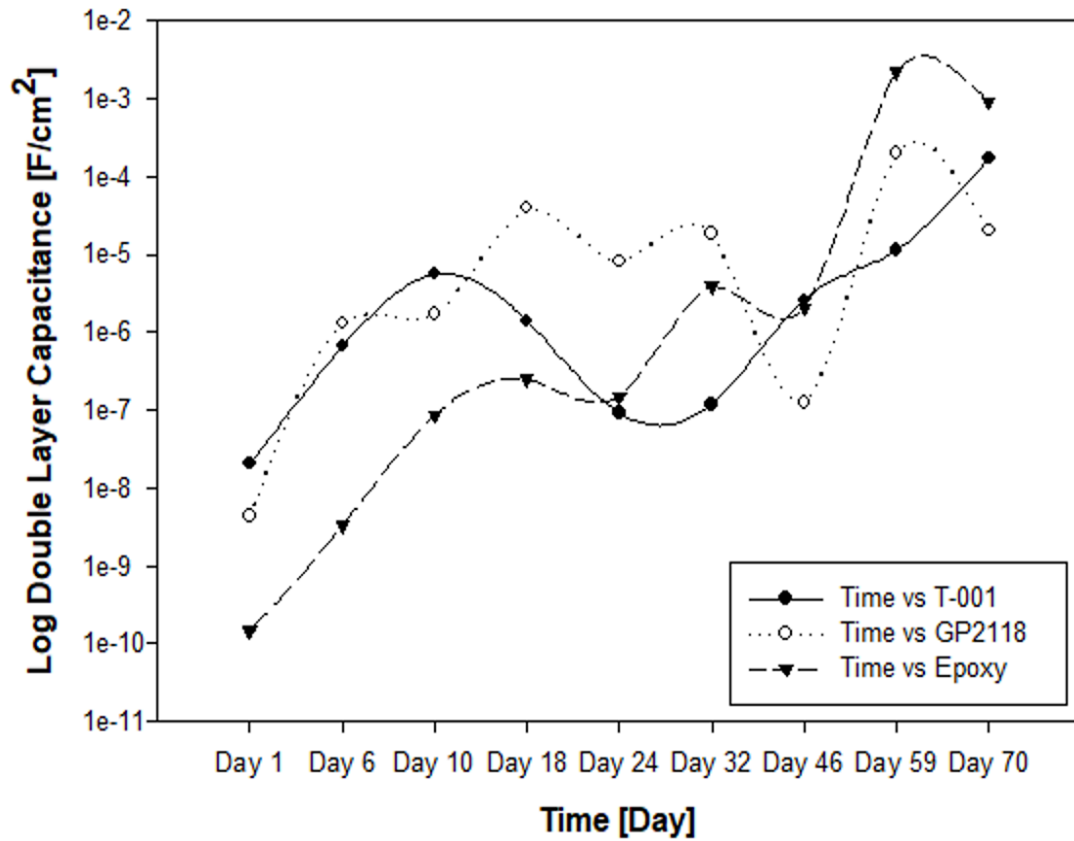


Figure 4.32 Double Layer Capacitance in NaCl Solution.

#### 4.4 Visual Observation

The enamel coated samples, that were immersed in NaCl solution, shows multiple rust points on the surfaces as was predicted by the EIS diagrams. The epoxy coating, instead, is continuous and uniform in all specimens and there are not evidently visible defects. On the other hand, the uncoated specimens present generalized corrosion on the surface as it was expected. Regarding the samples immersed in Ca(OH)<sub>2</sub> solution, it is observed the presence of a thin layer of calcium hydroxide/calcium carbonate deposit that covers all samples. This happens because it has worked with a saturate solution then the specimen surface is a preferential site for the deposition. Both enamel and epoxy coating rebars do not show a trace of corrosion, on the contrary, the uncoated rebars are only partially protected from corrosion, in fact, there are on the samples surfaces wide areas without corrosion alternate by areas where there is rust.

#### 4.4.1 Microstructural Analysis

Cross section SEM images at the interface with different magnification are presented in Figures 4.33 to 4.38. The enamel coating shows strong adhesion at the interface but there is a high-density of disconnected air-bubbles through the coating thickness; this structure affects both the slurry and the powder enamel coating. The air-bubbles are formed during the heating step, in fact, the high temperature promotes the chemical reaction between the carbon in the substrate and the coating oxides in order to produce carbon dioxide, that induces the bubbles generation. Observing the magnification images that show the coating/steel structure close to the interface (Figures 4.33B, 4.34B, 4.35B and 4.36B), all images present small-Fe protrusions that grow from the metal substrate to the enamel coating. This morphology increases the contact area between the steel and the enamel and they work as anchor points for the coating therefore the interface bounding is more efficient. The epoxy coating microstructure is also studied as a comparison with enamel coating performance (Figures 4.37 and 4.38). The epoxy coating has a compact and dense structure but at the interface there is a thin layer of corrosion between the epoxy and the steel due to low adhesion force in this area. The bounding between the epoxy and the steel is purely mechanical, in fact, any chemical reaction is involved during the deposition step that promotes the formation of protrusions or transition zones. As a result, disbondment corrosion can occur due to the loss of the adhesion at the interface, as shown in Figure 4.37B and 4.38B.

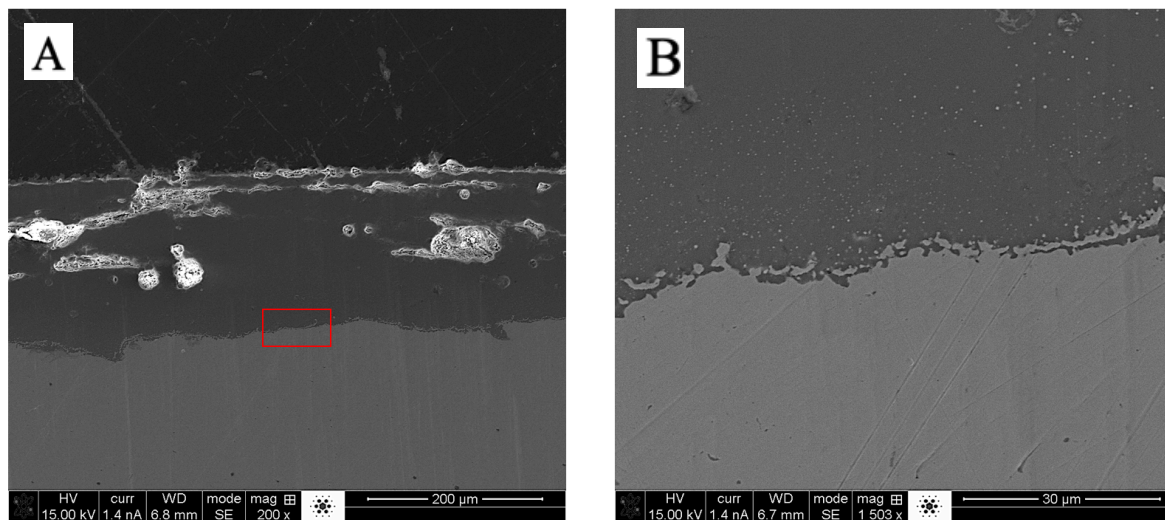


**Figure 4.33** Cross-sectional SEM images of T-001 in NaCl with different magnification: A) 200x and B) 1500x.

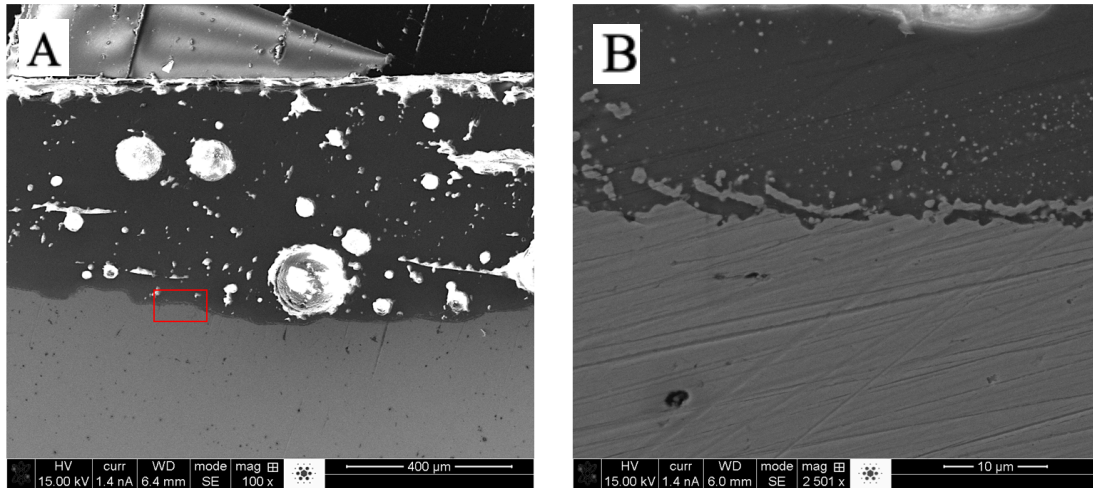


**Figure 4.34** Cross-sectional SEM images of T-001 in  $\text{Ca}(\text{OH})_2$  with different magnification: A) 100x and B) 2500x.

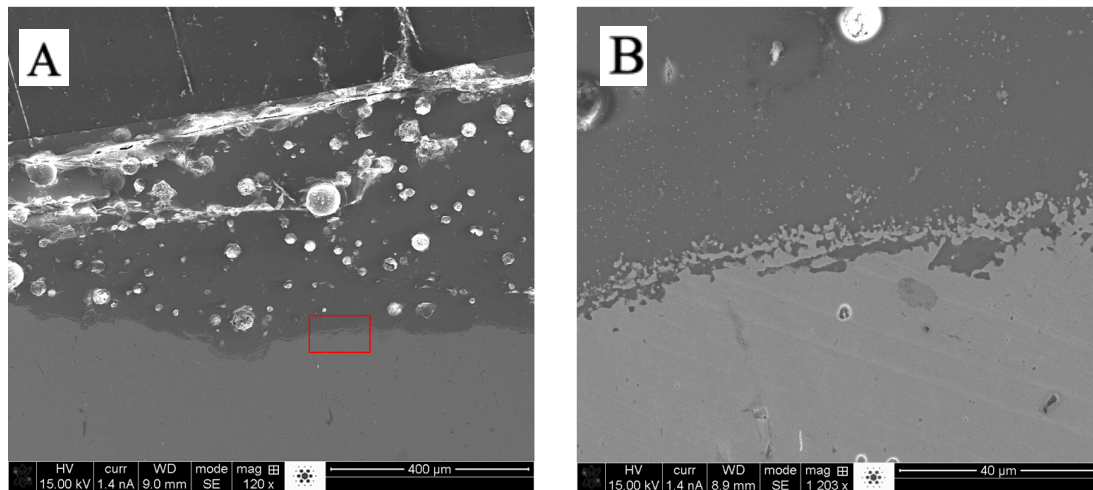


**Figure 4.35** Cross-sectional SEM images of GP2118 in  $\text{NaCl}$  with different magnification: A) 120x and B) 1200x.

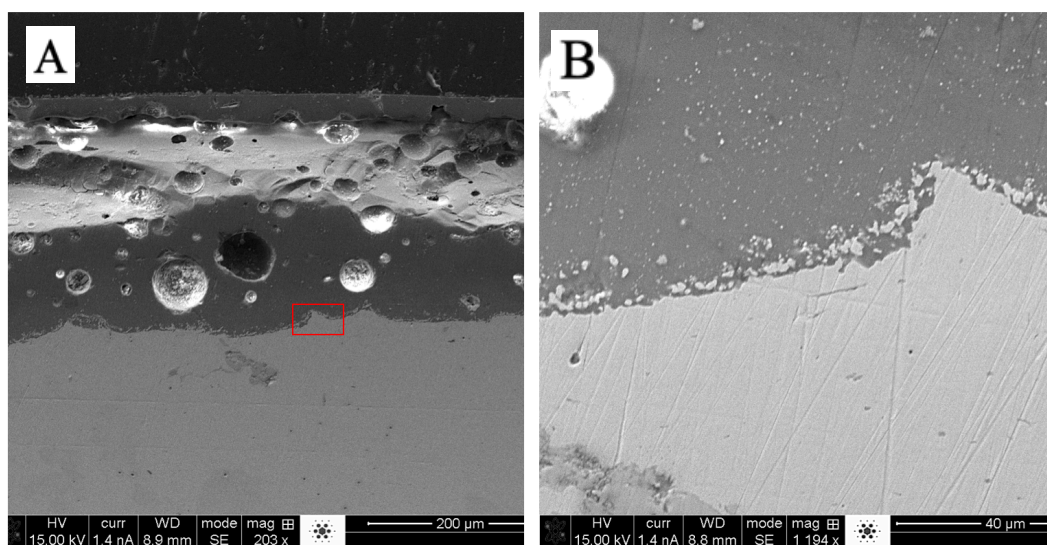


**Figure 4.36** Cross-sectional SEM images of GP2118 in  $\text{Ca}(\text{OH})_2$  with different magnification: A) 200x and B) 1200x.

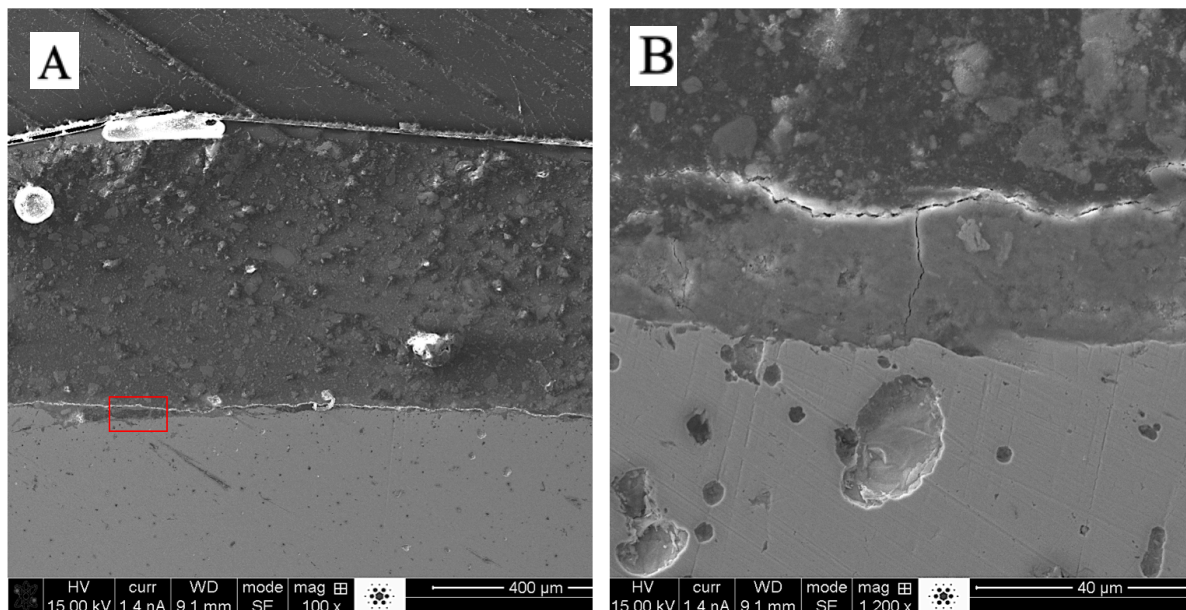


**Figure 4.37** Cross-sectional SEM images of Epoxy Coating in NaCl with different magnification: A) 100x and B) 1200x.

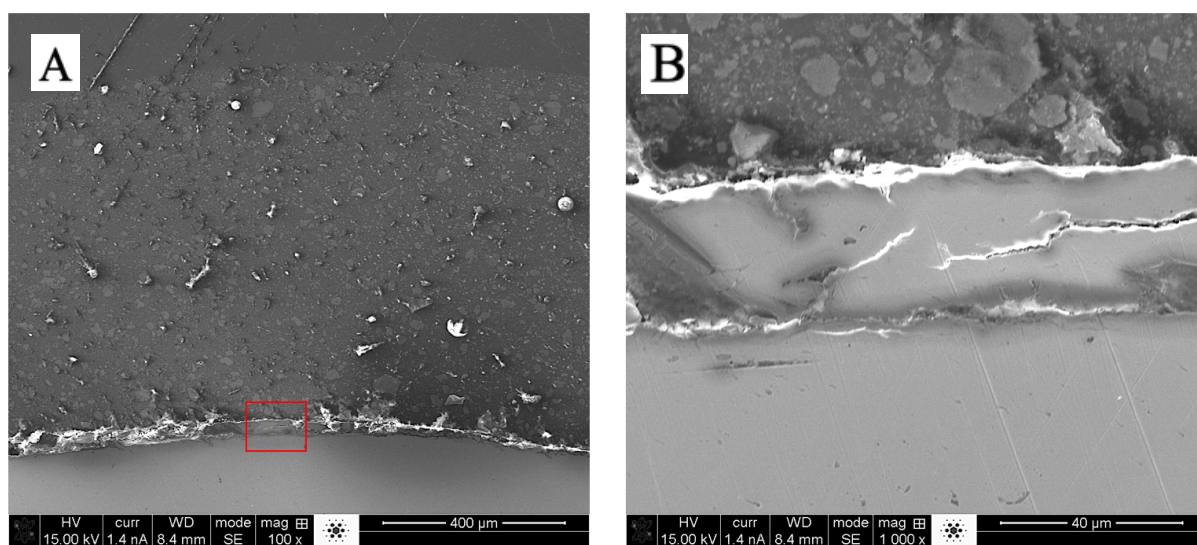


**Figure 4.38** Cross-sectional SEM images of Epoxy Coating in  $\text{Ca}(\text{OH})_2$  with different magnification: A) 100x and B) 1000x.

## 5 Discussion

### 5.1 Influence of Coating in Vibrating Pipe

The results provide an excellent prediction of the behaviour in no-coated steel pipe and in enamel coated pipe. In particular, comparing the obtained results of pipe vibrations, in Figure 4.1 and 4.6. The increasing of the diameter in the steel pipe induces a reduction of the vibration wavelength. On the contrary, the rise of pipe diameter in the enamel coating pipe brings the growth of the wavelength oscillation. Furthermore, the fluid rate modifies pipe behaviour in the presence of the coating. In the steel pipe, the increasing of the fluid rate does not change drastically the shape of vibration, in fact, the curves in Figure 4.4 present the same sinusoidal trend. On the other hand, the rise of fluid rate in enamel coated pipe, in Figure 4.8 provides an irregular pipe oscillation. Other changing in pipe vibrations are noticed when the soil nature changes. In the no-coated pipe, shown in Figures 4.2 and 4.3, for all tested  $K_s$  values, there are periodic fluctuations of the curve's trend. Nevertheless, for enamel coated pipes with ground soil constant equal to  $5 \text{ N/cm}^3$ , the graphs have a sinusoidal shape with a tiny wave's length, but with  $K_s$  value greater than  $5 \text{ N/cm}^3$ , the asymmetric trend prevails. Additionally, in Section 3.1 are studied the dependence of vibrations from fluid density and coating thickness. As described in Figure 4.5, for water, the curve has a periodic sinusoidal trend but reducing the fluid density the irregular behaviour is promoted. Finally, the coating thickness induces any changing in pipe vibrations, in fact, comparing Figure 4.6 and 4.7, the curve's trend is the same.

Overall, in all the above-mentioned cases, the deflection of steel pipe is lower than the maximum deflection  $y_{max}$ , that induces plastic deformation. Therefore, during the operating conditions, the pipes work in the elastic region. The presence of enamel coating has the benefit to reduce the pressure drops due to the less roughness surface. The losses of energy during the transmission step are lower because the enamel coating friction coefficient is lower than in the steel pipe. As a result, the presence of the coating allows a sensible reduction of pumping and energy cost. Unfortunately, the enamel coating, being a ceramic material, has not a plastic deformation region so it is subjected to fatigue damages during working conditions. As mentioned in [41], the enamel coating is chemically bonded with the pipe steel substrate then the cracks propagate in parallel to the surface inside the coating thickness. It is possible that there is the detachment of enamel fragments but never happens that the steel substrate is directly exposed to the environment. Therefore, the damaged coating is able to provide excellent protection from corrosion attacks also if the coating thickness is reduced.

### 5.2 Enamel Coating

The electrochemical test provides a complete impression of the quality and the morphology of epoxy and enamel coatings. Comparing the two Open Circuit Potential diagrams, presented in Figure 4.11 and 4.12, the graphs show in both cases a downward trend in the first 20 days of immersion until they reach the asymptotic values. The initial rapid drop is caused by the electrolyte penetration through the coating defects, in specific, the corrosion products gradually clog the damage's point, as a consequence, the corrosion rate is reduced and it reaches constant values. The corrosion products have different natures in the NaCl and  $\text{Ca}(\text{OH})_2$  solutions, in fact, in the first one the corrosion products do not protect the surface so new material is exposed to the solution and the corrosion process goes on. On the contrary, in the second one, the high

pH value of the solution thermodynamically induces the formation of a strongly adherent corrosion layer in the coating defects, that avoid the exposure of new surface and corrosion process terminates. The results of the Linear Polarization Resistance and the Current Corrosion Density show similar behavior. The epoxy coated samples present after 20 days the lower value of resistance and the higher value of current than enamel specimens. Surely, this is evidence that the epoxy coating degrades faster than the enamel one. In conclusion, in the long term, the enamel coating provides better barrier against corrosion. Furthermore, according to [42], both enamel coating shows a corrosion current density less than  $10^{-6}$  A/cm<sup>2</sup> so the steel substrate is well protected, instead, for epoxy coating this condition is not always verified. Regarding the EIS results and the SEM images, they provide significant information about the coating morphology and microstructure, in specific, the enamel coatings are severely damaged. The enamel coating's quality depends on the deposition technique, but the shape of the steel substrate also influences the final coating morphology. In this case, the rebar has an irregular surface with some grooves, therefore, a continuous layer is hard to obtain. Regarding the EEC analysis in NaCl solution, the coating which provides the better barrier against corrosion processes at long term in NaCl solution is the enamel coating because it has the highest charge transfer resistance  $R_{ct}$  and the lowest double layer capacitance  $C_{dl}$ . Specifically, the T-001 slurry enamel coating shows the greater behaviour than the GP2118 powder coating because the  $R_{ct}$  and  $C_{dl}$  values are, respectively, the highest and the lowest.

## 6 Conclusion

The main motivations of this work are the estimation of the enamel coating performance in two different situations, the understanding how the presence of the coating can modify the vibration profile in the pipelines and the protection that this coating can provide against corrosion processes on steel rebars immersed in NaCl and Ca(OH)<sub>2</sub> solutions. Regarding the vibration analysis, definitively the coating deposition influences the propagation and the shape of vibration.

- The vibration profile is extremely dependent on the pipe diameter, fluid density and soil constant. In particular, it is observed drastic changes in pipe vibration when in the simulating model it is taken into account the presence of the coating.
- The uncoated pipe vibration does not depend on the soil constant for clay grounds, instead, for the enamel coating systems, there is a strong modification of vibration profile due to the coating deposition.
- Fluid flow rate does not affect the vibration trend, so the increase of the fluid rate, for both systems, does not change the pipes vibration. Even if for the uncoated pipes, the vibration shows a sinusoidal trend, instead, for the enamel coated pipes, the vibration profile is totally irregular.
- The maximum observed deflection in all simulation models is around 1 cm, this means that in all situations, where different variables values are taken into consideration, the pipes never exceed the yield stress so these structures work in the elastic region.
- To estimate the fluid flow rate, it is studied the fluid dynamic conditions, in specific, it is derived the fluid motion's regime is totally turbulent with  $Re > 10^6$ .

In the following part are presented the main conclusion regarding the performance of the enamel coatings to prevent the degradation of reinforcement concrete.

- The enamel coatings show the highest value of polarization resistance in NaCl and Ca(OH)<sub>2</sub> solutions, compared to epoxy coated and uncoated samples. In particular, for NaCl solution the slurry and the powder coating have the resistance values close to  $10^5 \Omega \cdot cm^2$ , instead, for the Ca(OH)<sub>2</sub> solution the resistance is  $10^6 \Omega \cdot cm^2$ . This ensures that the coatings provide excellent protection against corrosion.
- The corrosion current density values for the enamel coatings are the lowest in both solutions, compared to the epoxy and uncoated samples. This parameter directly monitored the corrosion advancement so higher is the value of  $i_{corr}$ , more the electrochemical reactions are promoted.
- The EIS analysis and SEM images provide a clear picture of the morphology and the quality of the coatings. In specific, both enamel coatings are defect due to the irregular shape of the rebar's surface that makes it hard to obtain a constant and continuous layer. In addition, during the heating step at high temperature the reaction between the carbon alloy and the coatings oxides occurs and promotes the formation of carbon dioxide bubbles.
- The gradually decreasing of the impedance's modulus  $|Z|$  at low and middle frequencies in the enamel and epoxy coatings for the EIS analysis show the solution's penetration through the coatings.

- For the epoxy and the enamel coatings, the impedance's modulus at low frequencies for all the test time is higher than  $10^5 \Omega \cdot cm^2$  so both coatings provide good protection of the substrate against corrosion.
- The Equivalent Electric Circuit model show in both solutions that the enamel coatings provide the better barrier against corrosion because they have in the long term the highest value of charge transfer resistance  $R_{ct}$  and the lowest values of double layer capacitance  $C_{dl}$ .

## 7 Symbols List

<b>Symbol</b>	<b>Description</b>
$\beta_a$	Anodic Tafel Constant
$\beta_c$	Catodic Tafel Constant
$C_c$	Coating Capacitance
Ca(OH) <sub>2</sub>	Calcium Hydroxide
CP	Cathodic Protection
CPE <sub>c</sub>	Coating Constant Phase Elements
CPE <sub>dl</sub>	Double Layer Constant Phase Elements
CTE	Coefficient of Thermal Expansion
$d$	Inner Diameter
$D$	Outer Diameter
EEC	Electrical Circuit Model
$E$	Young's Modulus
$\xi$	Darcy Coefficient
$\epsilon$	Roughness
$EI$	Flexural Rigidity
EIS	Electrochemical Impedance Spectroscopy
$F_{cent}$	Centripetal Force
$F_{bend}$	Bending Reaction
FBE	Fusion Bonded Epoxy
$j$	Imaginary Unit
$I$	Inertia's Moment
$I_0$	Current Amplitude
$i$	Current
$i_{corr}$	Corrosion Current Density
$K_S$	Winkler's Constant
$l$	Beam's Length
$L$	Pipe Length
LPR	Linear Polarization Resistance
LEL	Lower Explosive Limit
$m$	Pipe Total Mass
$m_c$	Coating Mass

$m_f$	Fluid Mass
$M_C$	Bending Moment
MRI	Magnetic Resonance Imaging
$\eta$	Viscosity
NaCl	Sodium Chloride
$R$	Pipe Section Curvature Radius
$R_c$	Coating Resistance
$R_{dl}$	Double Layer Resistance
$R_p$	Polarization Resistance
$Re$	Reynolds Number
$\sigma_{max}$	Normal Stress
$\sigma_T$	Soil Pressure
$\sigma_y$	Yield Strength
OCP	Open Circuit Potential
P	Pressure
$\rho$	Density
PHMSA	Pipeline and Hazardous Materials Safety Administration
$q$	Load
s	Thickness
SCC	Stress Corrosion Cracking
SCE	Saturated Calomel Electrode
SEM	Scanning Electron Microscope
$\phi$	Phase Angle
UEL	Upper Explosive Limit
$v$	Fluid Velocity
$V$	Volume
$y_{max}$	Maximum Deflection
$\omega$	Radial Frequency
$W$	Resistance Modulus
$Z$	Impedance

## 8 References

1. Hansson, C. (2016). *An Introduction to Corrosion of Engineering Materials in Corrosion of Steel in Concrete Structures.*, Elsevier: Waltham, USA.
2. Pedefferri, P., et al., *Corrosion Science and Engineering*. Engineering materials. 1 Online-Ressource.
3. Koch, G., Brongers M., and Thompson N., (2002). *Corrosion Cost and Preventive Strategies in the United States*. NACE, National Association of Corrosion Engineers.
4. US Department of Transportation. *The State of the National Pipeline Infrastructure* Available from: <https://www.hsdl.org/?view&did=804318>.
5. PHMSA Pipeline and Hazardous Material Safety Administration. (2018). *National Pipeline Mapping System* Available from: [https://www.npms.phmsa.dot.gov/Documents/NPMS\\_Pipelines\\_Map.pdf](https://www.npms.phmsa.dot.gov/Documents/NPMS_Pipelines_Map.pdf).
6. Pipeline Safety Trust. (2015). *Pipeline Basics & Specifics About Natural Gas Pipelines.*; Available from: <http://pstrust.org/wp-content/uploads/2015/09/2015-PST-Briefing-Paper-02-NatGasBasics.pdf>.
7. Kyriakides, S. and Corona E. (2007). *Mechanics of Offshore Pipelines*. Elsevier Science. p. 34-52.
8. Mohinder, L.N. (1999). *Fabrication and Installation of Piping in Pipeline Handbook.*, McGraw-Hill Inc., New York. p. 320-327.
9. Fractracker Alliance. (2016). *Pipeline Construction: step-by-step guide available*. Available from: <https://www.fractracker.org/resources/oil-and-gas-101/pipeline-construction/>.
10. Nolan, D.P. (2014). *Physical Properties of Hydrocarbons and Petrochemicals*, in *Handbook of Fire and Explosion Protection Engineering Principles*. Elsevier: Waltham, US. p. 58-77.
11. ARIA Analysis Research and Information on Accidents. (2009). *Rupture and ignition of a gas pipeline 30 July 2004 Ghislenghien, Belgium*. Available from: [https://www.aria.developpement-durable.gouv.fr/wp-content/files\\_mf/FD\\_27681\\_Ghislenghein\\_v\\_2004ang.pdf](https://www.aria.developpement-durable.gouv.fr/wp-content/files_mf/FD_27681_Ghislenghein_v_2004ang.pdf).
12. Mahgerefteh, H. and Atti O. (2006). *An Analysis of the Gas Pipeline Explosion at Ghislenghien, Belgium*, in *AICHE Spring Meeting and Global Congress on Process Safety*. Orlando, FL, USA.
13. California Public Utilities Commission. (2012). *The San Bruno Catastrophe and Its Aftermath*.
14. Rosekind, R.M. (2012). *Invest Now or Pay Later – Lessons learned from San Bruno*, N.T.S. Board, Editor.
15. Massachusetts Department of Fire Services. (2019). *Merrimack Valley Gas Explosions*. p. 4 -6.
16. FHWA Federal Highway Administration. (2015). *Status of the Nation's Highways, Bridges, and Transit: Conditions & Performance*.
17. Petrovic, K.E., Vale B., and Zari P.M. (2017). *Building Materials in Materials for a Healthy, Ecological and Sustainable Built Environment*. Woodhead Publishing: Sawston, UK. p. 67 - 112.

18. McCormac, C.J. and Brown H.R. (2015). *Design of Reinforced Concrete*. Hoboken, NJ, USA: John Wiley & Sons.
19. Kahn System Standards. (1910). *A Hand Book of Practical Calculation and Application of Reinforced Concrete*. Engineering Department Trussed Concrete Steel Company: Detroit, MI, USA.
20. Sellevold, J.E. and Bjøntegaard Ø. (2006). *Coefficient of Thermal Expansion of Cement Paste and Concrete: Mechanisms of Moisture Interaction*. Materials and Structures. **39**: p. 809 -815.
21. Cverna, F. and A.S.M.I.M.P.D. Committee. (2002). *ASM Ready Reference: Thermal properties of metals*. ASM Ready Reference Series. ASM International.
22. Rossetti, A.V. (2003). *Il Calcestruzzo: Materiali e Tecnologia*. McGraw-Hill.
23. ASCE American Society of Civil Engineers. (2017). *Bridge C+ in Infrastructure Report Card*.
24. GAO US Government Accountability Office. (2016). *Highway Bridges - Linking Funding to Conditions May Help Demonstrate Impact of Federal Investment*.
25. Kunishima, M. (1994). *Collapse of the Korea Seoul Seongsu Bridge*.
26. Hilti. *Manuale sulla Corrosione* Available from: [https://www.hilti.it/content/dam/documents/pdf/e4/engineering/manuals/Hilti\\_Corrosion-Handbook\\_W4412\\_it.pdf](https://www.hilti.it/content/dam/documents/pdf/e4/engineering/manuals/Hilti_Corrosion-Handbook_W4412_it.pdf).
27. Rossi, S. (2008). *I Rivestimenti: La Pelle del design*. Italy.
28. PHMSA Pipeline & Hazardous Materials Safety Administration. (2018). *Internal Corrosion*, Department of Transportation, Editor.
29. CEPA Canadian Energy Pipeline Association. (2016). *How do pipeline operators prevent corrosion*.
30. Romano, M. (2005). *The Ins and Outs of Pipeline Coatings: Coatings Used To Protect Oil and Gas Pipelines*. Tyco Adhesives.
31. 3M. (2019). *3M™ Scotchkote™ Liquid Epoxy Coating 323*. Available from: <https://multimedia.3m.com/mws/media/193283O/3mtm-scotchkotetm-323-liquid-epoxy-coatings.pdf>.
32. American Petroleum Institute and Association of Oil Pipe Line. (2016). *Annual Liquids Pipeline Safety Excellence Performance Report Strategic Plan*. API-AOPL.
33. Hansson, C. (2016). *An Introduction to Corrosion of Engineering Materials*, in *Corrosion of Steel in Concrete Structures*, A. Poursae, Editor. Woodhead Publishing. p. 3-18.
34. Pedferri, P. (1985). *La Corrosione delle Armature nel Calcestruzzo*, in *Convegno sulle opere in calcestruzzo: Durabilità e ripristino*. Milano.
35. Poursae, A. (2016). *Corrosion of Steel in Concrete Structures*, in *Corrosion of Steel in Concrete Structures*., Elsevier. Waltham, USA.
36. Zanellato, V. (2013). *Studio degli effetti dell'interazione terreno-struttura nella progettazione di serbatoi circolari*, in *Civil Engineering Department*. Università degli Studi di Padova.
37. Udoetok, E. (2018). *Internal Fluid Flow Induced Vibration of Pipes*. Journal of Mechanical Design and Vibration. **6**: p. 1 – 8.

38. Mauri, R. (2005). *Elementi di Fenomeni di Trasporto. Manuale per Studenti di Ingegneria*. Pisa, Italy. Plus.
39. Farina, A. (2002). *Il moto dei Fluidi in un Condotto*. Available from: <http://pcfarina.eng.unipr.it/dispense01/porta130320/porta130320.htm>.
40. Kilareski, W. (1977). *Epoxy coatings for corrosion protection of reinforcement steel*, in *Chloride Corrosion of Steel in Concrete*. ASTM International.
41. Fan, L., et al. (2017). *Corrosion Resistances of Steel Pipes Internally Coated with Enamel*. CORROSION. **73**.
42. Clément, A., et al. (2012). *Numerical study of the linear polarisation resistance technique applied to reinforced concrete for corrosion assessment*. European Journal of Environmental and Civil Engineering. **16**(3-4): p. 491-504.
43. Husain A. and Chakkamalayath J. (2017). *Electrochemical impedance spectroscopy as a rapid technique for evaluating the failure of fusion bonded epoxy powder coating*, in *Engineering Failure Analysis*. p. 1350-6307.



## 9 Appendices

In this section are presented the MATLAB® codes used to solve the partial differential equation (PDE) which describe the pipe vibration, in particular, two different codes are been developed the first one, for un-coated pipe and the second one, for enamel coated pipe.

### 9.1 MATLAB Code for Clamped Pipe carrying Fluid

```
function Claped_pipe
% The following MATLAB function solves the partial differential equation
% that describes the pipe vibration due to the fluid flow.
% The solution appears as a 3D graph, in which the pipe deflection is
% evaluated as a function of distance and time.

E = 200*10^9;           % Steel Young's modulus [Pa]
D = .1524;             % Outer pipe diameter [m]
d = .1424;             % Inner pipe diameter [m]
I = pi*(D^4-d^4)/64;   % Pipe inertia moment [Kg/m^2]

EI=E*I;               % Flexural rigidity
L = 10;               % Pipe lenght [m]
Vf= pi*(d/2)^2*L ;    % Fluid volume [m^3]
rho_f = 680 ;         % Fluid density [Kg/m^3]
m_f = (rho_f*Vf)/L ;  % Fluid mass [Kg]
V_pipe = pi*L*(D^2-d^2)/4; % Pipe volume [m^3]
rho_pipe = 7700;      % Steel density [Kg/m^3]
m_pipe = (rho_pipe* V_pipe)/L; % Pipe mass per unit lenght [Kg/m]
m_tot = m_f + m_pipe; % Total pipe mass per unit lenght [Kg/m]
v = 25.78;           % Fluid rate [m/s]
C = v^2;
Ks = 5*10^6;         % Winkler's modulus [N/m^3]
B = Ks;
m = 0;
amp=0.01;
numElems=20;
numNodes = numElems + 1;
x = linspace(0,L,numNodes);
t=linspace(0, 10, 100);

% function setting
pde = @(x,t,u,DuDx) beampde(x,t,u,DuDx, EI, m_tot, m_f, B, C);
bc = @(xl,ul,xr,ur,t) beambc(xl,ul,xr,ur,t);
ic = @(x) beamic(x,L, amp);

sol = pdepe(m,pde,ic,bc,x,t);

u = sol(:,:,1);

%plot the results

figure;
surf(x,t,u);
title('Displacement function of Distance and Time in a Pipeline');

xlabel('Distance x [m]');
ylabel('Time t [s]');
zlabel('Displacement y [m]')

end

function [cr,fr,sr] = beampde(x,t,u,DuDx, EI, m_tot, m_f, B, C)
```

```

cr = [1 m_tot 0]';
fr = [0 -EI*DuDx(3)-m_f*C*DuDx(1) -DuDx(1)]';
sr = [u(2) -B*u(1) u(3)]';
end

function u0 = beamic(x, L, amp)
    s = sin(pi*x/L);
    u0 = [amp*s; 0; -amp*(pi/L)^2*s];
end

function [pl,ql,pr,qr] = beambc(xl,ul,xr,ur,t)
    pl = [ul(1) ul(2) 0]';
    ql = [0 0 1]';
    pr = [ur(1) ur(2) 0]';
    qr = [0 0 1]';
end

```

## 9.2 MATLAB Code for Enamel Coated Pipe carrying Fluid

```

function Claped_coating_pipe
% The following MATLAB code resolves the partial differential equation
% that describe the enamel coated pipeline vibration.
% The solution appears as a 3D graph, in which the pipe deflection is
% evaluated as a function of distance and time.

% Input data

Ep = 200*10^9; % Steel Young's modulus [Pa]
D = 0.1524; % Outer pipe diameter [m]
d = .1424; % Inner pipe diameter [m]
Ip = pi*(D^4-d^4)/64; % Pipe inertia moment [Kg/m^2]

Ec = 70*10^9; % Coating Young's modulus [Pa]
thickness = 340*10^-6; % Coating thickness [m]
dc = d - thickness; % Inner pipe coated diameter [m]
Ic = pi*(d^4 - dc^4)/64; % Coating inertia moment [Kg/m^2]
EI = Ep*Ip + Ec*Ic; % Total flexural rigidity

L = 10; % Pipe lenght [m]
Vf= pi*(dc/2)^2*L; % Fluid volume [m^3]
rho_f = 680; % Fluid density [Kg/m^3]
m_f = (rho_f*Vf)/L ; % Fluid mass [Kg]
V_pipe = pi*L*(D^2-d^2)/4; % Pipe volume [m^3]
rho_pipe = 7700; % Steel density [Kg/m^3]
m_pipe = (rho_pipe* V_pipe)/L; % Pipe mass per unit lenght [Kg/m]
Vc = pi*L*(d^2-dc^2)/4; % Coating volume [m^3]
rho_c = 2230; % Enamel density [Kg/m^3]
m_c = (rho_c*Vc)/L; % Coating mass per unit lenght [Kg/m]
m_tot = m_f + m_pipe + m_c; % Total pipe mass per unit lenght [Kg/m]

v = 25.78; % Fluid rate [m/s]
C = v^2;
Ks = 5*10^6; % Winkler's modulus [N/m^3]
B = Ks;
m = 0;
amp=0.01;
numElems=20;
numNodes = numElems + 1;
x = linspace(0,L,numNodes);
t=linspace(0, 10, 100);

% Functions setting

```

```

pde = @(x,t,u,DuDx) beampde(x,t,u,DuDx, EI, m_tot, m_f, B, C);

bc = @(xl,ul,xr,ur,t) beambc(xl,ul,xr,ur,t); % Boundary condition
ic = @(x) beamic(x,L, amp); % Initial condition

sol = pdepe(m,pde,ic,bc,x,t);

u = sol(:,:,1);

%plot the results

figure;
surf(x,t,u);
title('Displacement function of Distance and Time in a Coated Pipeline');

xlabel('Distance x [m]');
ylabel('Time t [s]');
zlabel('Displacement y [m]')

end

function [cr,fr,sr] = beampde(x,t,u,DuDx, EI, m_tot, m_f, B, C)
cr = [1 m_tot 0]';
fr = [0 -EI*DuDx(3)-m_f*C*DuDx(1) -DuDx(1)]';
sr = [u(2) -B*u(1) u(3)]';
end

function u0 = beamic(x, L, amp)
s = sin(pi*x/L);
u0 = [amp*s; 0; -amp*(pi/L)^2*s];
end

function [pl,ql,pr,qr] = beambc(xl,ul,xr,ur,t)
pl = [ul(1) ul(2) 0]';
ql = [0 0 1]';
pr = [ur(1) ur(2) 0]';
qr = [0 0 1]';
end

```



## 10 Acknowledgements

None of this would have been possible without the help and the support of my advisor, Dr. Gianpaolo Cimellaro. I am thankful for his aspiring guidance, invaluable constructive criticism and friendly advice during this thesis work.

Many Thanks.

Secondly, I would like to reserve a special thanks to Dr. Genda Chen, my mentor during the 6 months spent at the INSPIRE lab at the Missouri University of Science and Technology in the United States. I want to thank him for giving me the chance to join his research team, and for giving me the access to the laboratory and research facilities. He was always keen to know what I was doing and how I was proceeding.

I am grateful to Dr. Richard K. Brow for his sincere and valuable guidance.

My gratitude goes to Dr. Liang Fan for following and helping me in all the experimental work and for sharing his expertise with me. He was on my side all the time. I could not truly ask to meet a better person than him.

I am forever indebted to my parents, Roberto and Marilena, who have provided me support and continuous encouragement throughout my years of study.

And finally, last but by no means least, thanks to Francesca and Elisa, they are the first person I could count on.

Thanks Again to Everyone.

Erica Nesti